

# What chemical species are responsible for new particle formation and growth in the Netherlands? A hybrid positive matrix factorization (PMF) analysis using aerosol composition (ACSM) and size (SMPS)

Farhan R. Nursanto<sup>1</sup>, Roy Meinen<sup>2</sup>, Rupert Holzinger<sup>2</sup>, Maarten C. Krol<sup>1,2</sup>, Xinya Liu<sup>3</sup>, Ulrike Dusek<sup>3</sup>, Bas Henzing<sup>4</sup>, Juliane L. Fry<sup>1</sup>

<sup>1</sup>Meteorology and Air Quality (MAQ), Environmental Sciences Group, Wageningen University and Research (WUR), Wageningen, 6708PB, the Netherlands

<sup>2</sup>Institute for Marine and Atmospheric Research Utrecht, Department of Physics, Utrecht University, Princetonplein 5, 3584CC, Utrecht, the Netherlands

<sup>3</sup>Centre for Isotope Research (CIO), Energy and Sustainability Research Institute Groningen (ESRIG), University of Groningen, Groningen 9747 AG, the Netherlands

<sup>4</sup>Netherlands Organisation for Applied Scientific Research (TNO), Princetonlaan 6, 3584 Utrecht, the Netherlands

Correspondence to: Juliane L. Fry ([juliane.fry@wur.nl](mailto:juliane.fry@wur.nl))

**Abstract.** Aerosol formation acts as a sink for gas-phase atmospheric species that controls their atmospheric lifetime and environmental effects. To investigate aerosol formation and evolution in the Netherlands, a hybrid positive matrix factorization (PMF) analysis has been conducted using observations from May, June, and September 2021 collected in a rural site of Cabauw in Central Netherlands. The hybrid input matrix consists of the full organic mass spectrum acquired from a time-of-flight aerosol chemical speciation monitor (ToF-ACSM), ACSM *inorganic* species concentrations, and binned particle size distribution concentrations from a scanning mobility particle sizer (SMPS). These hybrid PMF analyses discerned ~~six~~*four* factors that describe aerosol composition variations: ~~four~~*two* size-driven factors that are related to new particle formation (NPF) and growth (~~F6, F5, F4, and F3~~), and two bulk factors driven by composition, not size (F2, ~~and~~ F1). ~~The distribution of chemical species across these factors shows different compounds responsible for nucleation and growth of new particles. The smallest-diameter size factor (F6F4) contains ammonium sulfate and organics, and typically occurs peaks during the daytime. Newly formed particles, represented by F6F4, are correlated mainly with wind from the southwesterly-westerly, northerly, and easterly sectors that transport sulfur oxides (SO<sub>x</sub>), ammonia (NH<sub>3</sub>), and organic precursors to Cabauw. As the particles grow from F6F4 to F3 and bulk factors, nitrate and organics plays an increasing role, and the particle loading diurnal cycle shifts from daytime to a nighttime maximum. The inorganic ion balance and organics composition in the bulk atmosphere affects the chemical composition variation across factors and seasons. Changing ammonium-sulfate-nitrate equilibrium shifts inorganic species among factors, and greater~~ Greater organics availability makes secondary organic aerosol (SOA) more influential in summertime aerosol growth, principally due to volatility differences produced by seasonal variation in photooxidation and temperature.

Style Definition: Normal (Web)

Formatted: Width: 21 cm, Height: 24 cm

Formatted: Font color: Auto

Formatted: Font color: Auto

Keywords: new particle formation (NPF), positive matrix factorization (PMF), particle size distribution, sulfate aerosol, nitrate aerosol, organic aerosol

1. Introduction

Atmospheric aerosols are solid or liquid particles suspended in the air that are formed from natural or anthropogenic sources (Haywood, 2016). To describe the aerosol particle size distribution, four modes are generally distinguished according to the particle geometric diameter ( $D_p$ ): nucleation mode ( $D_p < 20\text{ nm}$ ), Aitken mode ( $20\text{ nm} < D_p < 100\text{ nm}$ ), accumulation mode ( $100\text{ nm} < D_p < 1000\text{ nm}$ ), and coarse mode ( $D_p > 1\text{ }\mu\text{m}$ ) (Hussein et al., 2004; Wu et al., 2008). New particle formation (NPF) is identified by a rapid buildup of high atmospheric concentrations of aerosol particles in the nucleation mode. These particles subsequently grow into Aitken mode particles and further (Maso et al., 2005; Spracklen et al., 2010; Salimi et al., 2015; Kerminen et al., 2018; Lee et al., 2019).

Aerosols impact the Earth by absorbing and scattering solar and terrestrial radiation (Andreae and Crutzen, 1997; Grantz et al., 2003; Wong et al., 2017; Marrero-Ortiz et al., 2019), and indirectly by producing or modifying clouds (Lohmann and Feichter, 2005; Mahowald et al., 2011; Fan et al., 2018). NPF plays a prominent role in cloud formation by contributing to over 50% of cloud condensation nuclei formation, which affects the lifetime and radiative properties of clouds (Bianchi et al., 2016; Gordon et al., 2016; Haywood, 2016; Dall'Osto et al., 2018; Lee et al., 2019). These phenomena affect the ecosystem physically by modifying radiation diffusion, temperature, and precipitation (Grantz et al., 2003; Haywood, 2016; Lee et al., 2019). Aerosols also influence the ecosystem chemically through influencing the spatial patterns of nitrogen deposition (van der Swaluw et al., 2011; Wamelink et al., 2013) and oxidative processes (Xing et al., 2017), leading to ecological harm such as soil pollution, water acidification, eutrophication, and loss of biodiversity (Erisman et al., 2011; Wamelink et al., 2013). In terms of public health, aerosols exhibit adverse effects on human health due to their size and chemical composition. NPF events are typically followed by air quality degradation, which is consistently associated with elevated pulmonary and cardiovascular morbidity and mortality worldwide (Ayala et al., 2012; Pope et al., 2020).

Sulfuric acid ( $\text{H}_2\text{SO}_4$ ) is typically understood to be the most prevalent nucleation-inducing agent in NPF events, together with other airborne chemical species, including nitrate, nitric acid ( $\text{HNO}_3$ ), bases (e.g., amines), and organic acids (Zhang et al., 2012; Kulmala et al., 2013; Zhang et al., 2015; Wagner et al., 2017; Lehtipalo et al., 2018; Kürten, 2019; Lee et al., 2019; Brean et al., 2021; Olin et al., 2022). Numerous studies also report low-volatility organic species, such as terpene oxidation products and organic nitrates, participating in the formation of new particles (Berkemeier et al., 2016; Bianchi et al., 2016; Tröstl et al., 2016; Barsanti et al., 2017; Dall'Osto et al., 2018; Kerminen et al., 2018; Lee et al., 2019; Heinritzi et al., 2020).

Formatted: Font: +Headings (Times New Roman)

Formatted: Font: +Headings (Times New Roman)

Formatted: Font: +Headings (Times New Roman)

Formatted: Font: +Headings (Times New Roman), English (United Kingdom)

Formatted: English (United Kingdom)

Formatted: Font: +Headings (Times New Roman)

Formatted: Font: +Headings (Times New Roman)

Formatted: Font: +Headings (Times New Roman), English (United Kingdom)

Formatted: English (United Kingdom)

Formatted: Font: +Headings (Times New Roman)

Formatted: Font: +Headings (Times New Roman), English (United Kingdom)

Formatted: English (United Kingdom)

Formatted: Font: +Headings (Times New Roman)

Formatted: Font: +Headings (Times New Roman)

Formatted: Font: +Headings (Times New Roman)

Formatted: Font: +Headings (Times New Roman), English (United Kingdom)

Formatted: English (United Kingdom)

Formatted: Font: +Headings (Times New Roman), English (United Kingdom)

Formatted: English (United Kingdom)

65 In this work, we show that co-located measurements of aerosols' atmospheric composition and particle size distribution can be  
used to characterize the chemical composition of new particle and aerosol components that facilitate their growth. A time-of-  
flight aerosol chemical speciation monitor (ToF-ACSM, Aerodyne Inc.) allows the continuous and real-time quantification of  
non-refractory chemical species in ambient air (Ng et al., 2011; Fröhlich et al., 2013). For particle size distributions, the  
scanning mobility particle sizer (SMPS) provides real-time measurement of submicron particle number concentrations of  
different sizes (Amaral et al., 2015; Wiedensohler et al., 20182012).

70 Aerosol mass spectrometry measurements have been used extensively with positive matrix factorization (PMF) as a strategy  
for aerosol source apportionment, especially regarding the organic components (Lanz et al., 2007; Jimenez et al., 2009; Ulbrich  
et al., 2009; Ng et al., 2010; Zhang et al., 2011). This paper combines the full organic mass spectrum and chemical species  
concentrations from ToF-ACSM with particle size distribution from SMPS into a hybrid PMF input matrix, to study the  
75 association between chemical composition and particle size distribution. A similar approach for hybrid ACSM-SMPS PMF  
analysis was used for a European aerosol dataset comparison (Dall'Osto et al., 2018). Previous studies on aerosol source  
apportionment in the Netherlands have focused on organic aerosol composition (Mooibroek et al., 2011; Mensah et al., 2012;  
Schlag et al., 2016). Here, we analyze ACSM-SMPS datasets from Cabauw, the Netherlands, collected as part of the Ruisdael  
Observatory Land-Atmosphere Interactions Intensive Trace-gas and Aerosol (RITA) campaign in May to September 2021  
80 (<https://ruisdael-observatory.nl>), using PMF to characterize the chemical species responsible for new particle formation and  
growth across several seasons. Several studies have shown NPF events dependent on air mass origin transporting different  
pollutants (Hamed et al., 2007; Modini et al., 2009; Castro et al., 2010; Asmi et al., 2011; Németh and Salma, 2014; Nieminen  
et al., 2014; Qi et al., 2015; Mordas et al., 2016; Kolesar et al., 2017; Peng et al., 2017; Kerminen et al., 2018; Pushpawela et  
al., 2019), and therefore we also explore relationships between wind direction, wind speed, and factor timeseries time series to  
85 interpret source apportionment.

## 2. Methods and Instrumentation

### 2.1. Cabauw site and meteorological conditions

90 Measurements were performed at the CESAR tower (51.970° N, 4.926° E), managed and operated by the Royal Netherlands  
Meteorological Institute (KNMI, the Netherlands) (see Fig. 1a). The tower is located near Cabauw, in the province of Utrecht,  
the Netherlands, approximately 18 km southwest of Utrecht city center, 31 km east of the city and (largest in Europe) port of  
Rotterdam, 45 km south of Amsterdam, and about 45 km southeast of the Dutch North Sea coast. To the east and south of the  
site are the provinces of Gelderland and Noord-Brabant, which consist mainly of forests, agricultural lands with clay and sand  
soil types for crops, and animal farms, specifically chicken and pig farms in the south and cattle in the east (CBS, 2022). The  
Cabauw site itself is rural and surrounded by agricultural lands. The dataset used in this analysis contains overlapping ACSM

Formatted: Font: +Headings (Times New Roman)

Formatted: Font: +Headings (Times New Roman)

Formatted: Font: +Headings (Times New Roman)

Formatted: Font: +Headings (Times New Roman), English (United Kingdom)

Formatted: English (United Kingdom)

Formatted: Font: +Headings (Times New Roman)

Formatted: Font: +Headings (Times New Roman)

Formatted: Font color: Auto

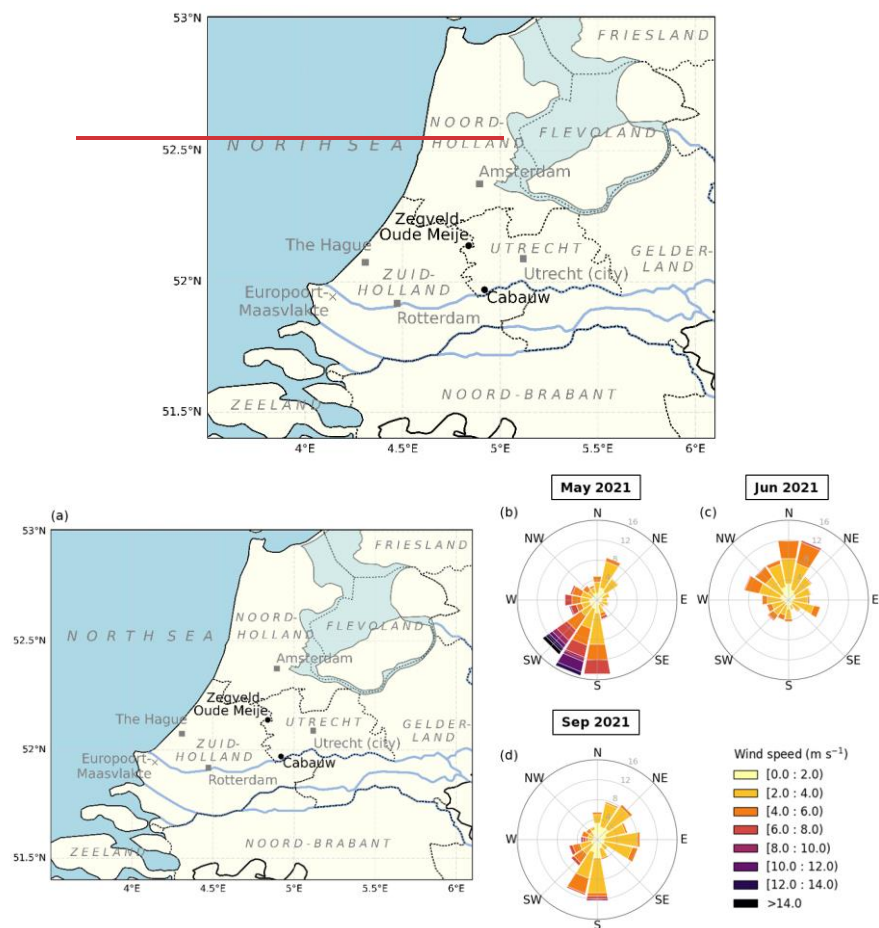
Formatted: Font color: Auto

Formatted: Underline

Formatted: Font: +Headings (Times New Roman)

Formatted: Font: +Headings (Times New Roman)

95 and SMPS data split into periods from 11–31 May 2021, 1–22 June 2021, and 1–30 September 2021, providing some seasonal variation. To simplify, we will refer to these periods as May, June, and September, respectively, in this paper.



100 **Figure 1.** (a) Map of a part of the Netherlands showing the locations of the measurement stations Cabauw (main site) and Zegveld-Oude Meije (auxiliary NH<sub>3</sub> measurements). The province, sea, and neighbouringneighboring country names are indicated in italic and light grey. The big cities of Amsterdam, The Hague, Rotterdam, and Utrecht in the area collectively known as “Randstad” are situated in Noord-Holland, Zuid-Holland, and Utrecht provinces. The urban and harbor area of Rotterdam extends as Europoort-Maasvlakte to the mouth of

105 the Maas River. (b-d) Wind rose plots for May, June, and September 2021. Winds from S up to SW sector were dominant in May. In June, the prevailing winds were from WNW up to the NNE sector. In September, two major wind directions were from the E and S sectors.

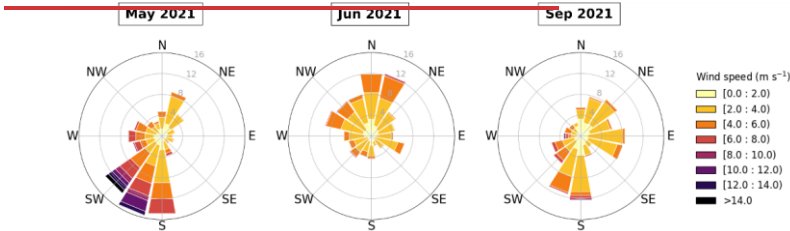
Formatted: Font: Not Bold

110 Weather data were retrieved from the Royal Netherlands Meteorological Institute (KNMI, <https://www.knmi.nl>). In general, May 2021 was characterized by moderate spring temperatures (11.8 °C on average) with scattered precipitation transitioning into the warmer summer period. June 2021 had the highest temperatures (18.7 °C on average) and was the sunniest of the three periods, reflecting summer weather. September 2021 showed warm temperatures, (16.2 °C on average), with less radiation and precipitation compared to May 2021. Winds from south to southwest ~~sector~~ (180° to 225°) dominated in spring (May), bringing plumes from the agriculture-heavy province of Noord-Brabant. In summer (June), the prevailing air masses were coming from west-northwest to north-northeast (292.5° to 22.5°), bringing air from the North Sea and some major cities along the coast and/or in the Randstad, such as Rotterdam, The Hague, Amsterdam, and Utrecht. More diverse wind plumes were observed in  
115 September, ranging from easterly (22.5° to 112.5°), coming from the forested nature and agricultural areas in the province of Gelderland, and southerly (180° to 202.5°), coming from the province of Noord-Brabant. The meteorological variables for each period are summarized in Table 1 and the wind variables are visualized as wind roses in Fig. 2**1b-d**.

Formatted: Font: 9 pt, Bold

**Table 1.** Meteorological conditions on three periods analyzed (May, June, and September 2021). The periods represent spring, summer, and autumn weather, respectively.

Period	Temperature (°C)	Downward shortwave radiation (W m <sup>-2</sup> )	Precipitation (mm)
11–31 May 2021	11.8 (mean) 3.5 (low), 23.0 (high)	211.7 (mean) 1032.2 (max)	96.6 (total)
1–22 Jun 2021	18.7 (mean) 8.1 (low), 29.6 (high)	264.9 (mean) 957.2 (max)	31.2 (total)
1–30 Sep 2021	16.2 (mean) 5.7 (low), 26.7 (high)	142.0 (mean) 818.9 (max)	24.4 (total)



2.2. Measurement setup

2.2.1. Chemical species measurements

**Figure 2.** Wind rose plots for May, June, and September 2021. Winds from S up to SW sector were dominant in May. In June, the prevailing winds were from WNW up to the NNE sector. In September, two major wind directions were from the E and S sectors.

2.3. Measurements

The ToF-ACSM was the main instrument employed for this analysis. The instrument has been detailed in other work (Fröhlich et al., 2013). The ACSM was installed with an inlet at 5-meter height, a cyclone with size cut of 2.5 µm (PM<sub>2.5</sub>), and an aerodynamic lens in the inlet system allowing the analysis of non-refractory organics, ammonium, nitrate, sulfate, and chloride, and potassium in the aerosol phase. The instrument has been detailed in other work (Fröhlich et al., 2013). The Ambient air was drawn into the instrument is through a stainless-steel tubing inlet system equipped with a PM<sub>2.5</sub> size-cut cyclone (URG-2000-30ED) and a Nafion dryer, sampling at 4.5-meter height with flow rate of 2 L min<sup>-1</sup>. An intermediate pressure lens (IPL) is used as aerodynamic lens allowing transmission of particles in the PM<sub>2.5</sub> fraction (Xu et al., 2017). The instrument uses a capture vaporizer (CV) instead of the standard vaporizer (SV), which is designed to increase the particle collection efficiency (Middlebrook et al., 2012; CE) compared to standard vaporizer (SV) (Jayne and Worsnop, 2016). By having a narrow entrance, the CV increases the particle collision events and thus increases the contact with the hot vaporizer surface, minimizing particles that bounce without evaporation (Hu et al., 2017) and resulting in higher CE. Consequently, however, the fragmentation patterns are shifted towards smaller ion masses due to the additional thermal decomposition (Hu et al., 2017; Xu et al., 2017;

Zheng et al., 2020). The average flow rate in the sample line of the instrument is  $1.22 \text{ cm}^3 \text{ s}^{-1}$  ( $0.07 \text{ L min}^{-1}$ ). Combining the  $\text{PM}_{2.5}$  cut cyclone,  $\text{PM}_{2.5}$  aerodynamic lens, and CV allows the ToF-ACSM to be a  $\text{PM}_{2.5}$  measurement (Xu et al., 2017).

Formatted: Font: +Headings (Times New Roman)

The ToF-ACSM provides unit mass resolution (UMR) mass spectra with 10-minute time resolution which are analyzed using Tofware v3.2 in Igor Pro 8. The fractions of measured UMR signals were assigned to individual aerosol species using the fragmentation table: (Allan et al., 2004). On-site calibrations are performed to determine the ionization efficiencies of the chemical species. ~~The calibration with~~ The calibrations of ionization efficiency (IE) and relative IE (RIE) were performed following the procedures described in previous studies by using 300–350 nm pure ammonium nitrate ( $\text{NH}_4\text{NO}_3$ ) and ammonium sulfate ( $(\text{NH}_4)_2\text{SO}_4$ ) dissolved in aqueous solution. The calibration with gives ionization efficiency (IE) IE value of 250.0 ions  $\text{pg}^{-1}$  for nitrate ( $\text{NO}_3$ ), and ~~relative ionization efficiency (RIE) RIE~~ values of 1.40, 1.67, 1.30, and 3.35, ~~and 1.00~~ for organics, (Org), sulfate ( $\text{SO}_4$ ), chloride (Cl), and ammonium ( $\text{NH}_4$ ), and ~~potassium (K)~~, respectively. The detection limit values for the ToF-ACSM are expected to be similar to other studies using the same instrument setup (Fröhlich et al., 2013; Zheng et al., 2020), where the values are 198–351.8  $\text{ng m}^{-3}$  for Org, 182–470.3  $\text{ng m}^{-3}$  for  $\text{NH}_4$ , 21–41.8 for  $\text{NO}_3$ , 18–33.6  $\text{ng m}^{-3}$  for  $\text{SO}_4$ , and 11–31.4  $\text{ng m}^{-3}$  for Cl.

In addition to the aerosol measurements by the ToF-ACSM, ambient sulfur dioxide ( $\text{SO}_2$ ) concentrations were obtained from the open-source data of Landelijk Meetnet Luchtkwaliteit (LML, <https://www.luchtmeetnet.nl>), measured at the same location. Ammonia ( $\text{NH}_3$ ) concentrations were obtained from measurements in Zegveld-Oude Meije station, 20 km to the north of Cabauw station (see Fig. 4), ~~also acquired from LML. The particle size distribution concentration measurements were conducted using a TROPOS-SMPS with 8 nm to 800 nm size range and 5-minute time resolution from a 5-meter height inlet. The co-located weather data were retrieved from the Royal Netherlands Meteorological Institute (KNMI, <https://www.knmi.nl>), also acquired from LML.~~

Formatted: Font color: Auto

Formatted: Font color: Auto

### 2.2.2. Particle size distribution measurements

The particle size distribution measurements were conducted using a TROPOS-SMPS. The instrument has been detailed in other work (Wiedensohler et al., 2012). Ambient air was sampled using a stainless-steel inlet equipped with  $\text{PM}_{10}$  size-cut cyclone and Nafion dryer at 4.5-meter height sampling with a flow rate of  $16.7 \text{ L min}^{-1}$ . The SMPS inlet was placed approximately 3 m lateral distance from the ACSM instrument inlet. The instrument consists of a Vienna-type differential mobility analyzer (DMA) and a butanol-based TSI condensation particle counter (CPC) 3750. The flow rate in the instrument is  $1.0 \text{ L min}^{-1}$ . The TSI CPC 3750 has the collection efficiency of 100% at the first selected and reported size of 10 nm.

The raw dataset was processed using a linear multiple charge inversion algorithm to derive the particle number size distribution (PNSD or  $\text{dN}/\text{dlog}(D_p)$ ) (Wiedensohler et al., 2012; Pfeifer et al., 2014). The MPSS inversion algorithm version 2.13 was utilized to obtain final PNSD from the raw dataset. The final PNSD has 5-minute time resolution and covers 71 geometric

mean diameters ( $D_p$ ) from 8 nm to 853 nm. The particle number concentrations (dN) for individual  $D_p$  were then calculated by multiplying PNSD with  $\text{dlog}(D_p)$  values.

#### 2.4.2.3. Positive matrix factorization (PMF)

The 10-minute average matrices of UMR organic fragment mass spectra with mass-to-charge ratio (m/z) 12 to 120 were combined with the inorganic species average mass concentrations (i.e., organics (Org), ammonium ( $\text{NH}_4$ ), nitrate ( $\text{NO}_3$ ), sulfate ( $\text{SO}_4$ ), and chloride ( $\text{Cl}$ ), and potassium (K)), and the 10-minute average particle number concentrations (dN) in 18 particle diameter ( $D_p$ ) size bins from 71 geometric mean diameters ( $D_p$ ) to generate hybrid input data matrices for PMF analysis. Each organic fragment mass-to-ratio (m/z), species concentration, and size-binned particle concentration is treated as an individual variable in the PMF.

The values and errors of organic fragment mass spectra and inorganic mass concentration variable values and errors variables, and the minimum error (minErr) of all species were generated by Tofware v3.2 in Igor Pro 8. The 10-minute resolution particle size dataset was obtained from the SMPS instrument as 5-minute resolution particle number concentration described in the Sect. 2.2.2. The particle number concentrations are categorized into 18 size bin variables (8–10 nm; 10–13 nm; 13–16 nm; 16–20 nm; 20–25 nm; 25–32 nm; 32–40 nm; 40–51 nm; 51–65 nm; 65–83 nm; 83–107 nm; 107–140 nm; 140–185 nm; 185–249 nm; 249–342 nm; 342–481 nm; 481–691 nm; and 691–853 nm). Each size bin contains the sum of four concentration points, (except for the last bin containing only three concentration points), then averaged to 10 minutes. We use larger bin sizes for the larger diameters because larger particles occur less frequently. The errors for each size bin are taken to be the population standard deviation of the raw data. The variable values of species mass concentrations and particle number concentrations were weighted prior to analysis to ensure that individual peaks have similar magnitude as the organic mass spectrum. This weighting was done to give all variables the same importance in the PMF analysis. standard deviation of the raw data.

We performed the analysis using the PMF Evaluation Tool (PET) v3.08 (Ulbrich et al., 2009) in Igor Pro 8. The details of applying positive matrix factorization (PMF) to aerosol mass spectrometry datasets have been discussed elsewhere in detail (Paatero and Tapper, 1994; Paatero, 1999; Ulbrich et al., 2009). The first step of the factor analysis was identifying the optimum number of factors by running unconstrained experiments using 2 to 10 factors. The optimum number of factors is selected by considering the lowest residuals of the PMF solutions, and whether all the factors are environmentally reasonable and unique based on their chemical composition. For all three-month datasets, this analysis converges to an optimum of 6 factors. The ordering of the factors is not identical across months and for ease of presentation, we reorder them so that factors of similar identity have the same factor number across months. The percent of signal explained by each factor is presented alongside plots of the factor profiles, to enable the reader to deduce the original factor ordering. The resulting hybrid PMF solution matrix is split back up into organic mass spectrum, species mass concentrations, and particle number concentration bin matrices, and the value of each variable is readjusted (undoing the previously described re-weighting) so that the ACSM species mass

Formatted: Font: +Headings (Times New Roman)



concentrations can still be interpreted quantitatively. Prior to analysis before the PMF input matrix preparation, the variable values and errors of species mass concentrations and particle number concentrations were downweighted in reference to the highest average peak of the original organic mass spectrum,  $m/z$  44 ( $f_{44}$ ). During PMF input matrix preparation in PETv3.08, the  $m/z$  44, 28, 18, 17, and 16 signals in the organic mass spectrum are also downweighted as provided by the procedure to account for duplicated information of  $m/z$  44 in the organic mass spectrum (Ulbrich et al., 2009). The details of PMF variable downweighting can be found in Sect. S3.

The first step of the factor analysis was identifying the optimum number of factors ( $p$ ) by running unconstrained experiments using 2 to 8 factors and varying the seed value (min = 0; max = 20; delta = 1) to pick different initial values for the PMF algorithm. The optimum  $p$  is selected by considering the lowest residuals and local minima ( $Q/Q_{\text{exp}}$ ) of the PMF solutions. Alongside the local minima, we considered whether all the factors are environmentally reasonable and unique mainly based on their particle size distribution and chemical composition. After the optimum  $p$  and seed value are chosen, the rotationality of the best PMF solution is explored by varying the rotation ( $f_{\text{peak}}$ ) value (min = -1, max = +1, delta = 0.2). Bootstrapping runs with 100 iterations on the chosen PMF solution were performed to estimate the uncertainty in the factor profile variables and time series, ensuring the robustness of the solution.

To determine the organic and inorganic composition in each PMF factor, the particle size distributions are removed from the factor profile. The total organic mass fraction is considered as the sum of organic fragments fraction from  $m/z$  12 to 120, while the inorganic mass fractions are upweighted back and taken as  $\text{NH}_4$ ,  $\text{NO}_3$ ,  $\text{SO}_4$ , and Cl mass fractions. The final fraction of each species is determined by dividing the species mass fraction with the total organic and readjusted inorganic mass fraction.

#### 2.5.2.4. Wind analysis

To analyze the factors using wind variables, we investigate the prevailing wind for several pollution episodes observed in the dataset. Bivariate polar plots are generated for selected-factor reconstructed mass concentration derived from PMF analyses and mass concentration for each ACSM species in each period using the “Openair” package in the “R” environment (Carslaw and Ropkins, 2012). The wind parameters are obtained from co-located measurement of 10-meter wind direction data acquired from KNMI.

### **3. Results and Discussion**

#### 3.1. Mean bulk atmospheric chemical composition across periods

We hypothesize that the mean bulk atmospheric chemical composition influences how the chemical species are distributed across the PMF factors. Therefore, we discuss this topic before the PMF solutions. To compare the mean bulk composition among periods, we choose the springtime period (May) as reference. The mean concentrations of atmospheric species and the

Formatted: Font: +Headings (Times New Roman)

species percentages in the bulk atmosphere are summarized in Table S1. In summer (June), we observe roughly a doubling in aerosol concentration for all IA and an increase with a factor 2.6 in OA compared to spring (May). In autumn (September), the particle concentrations decrease again, with a relatively larger decrease for sulfate.

**Table 2.** Mean bulk atmospheric chemical composition in the three periods, summarized as the values of total aerosol mass loading in  $\mu\text{g m}^{-3}$ , ion balance ratio ( $NH_4\text{ }_{bal}$ ) from linear regression, and mean organic-to-inorganic ratio ( $m_{Org}/m_{IA}$ ). A more detailed information about each chemical species can be seen in Table S1.

Mean value	May 2021 (spring)	Jun 2021 (summer)	Sep 2021 (autumn)
Bulk aerosol composition <sup>(a)</sup> <div><div>Org</div><div>NH<sub>4</sub></div><div>NO<sub>3</sub></div><div>SO<sub>4</sub></div><div>Cl</div></div>			
Aerosol mass loading <sup>(c)</sup>	6.60 $\mu\text{g m}^{-3}$	14.12 $\mu\text{g m}^{-3}$	5.15 $\mu\text{g m}^{-3}$
$NH_4\text{ }_{bal}$ <sup>(b)</sup>	0.997 $\pm$ 0.001	0.986 $\pm$ 0.001	1.066 $\pm$ 0.001
$m_{Org}/m_{IA}$ <sup>(a)</sup>	0.61	0.82	0.74

<sup>(a)</sup> mass concentration, <sup>(b)</sup> molar concentration, <sup>(c)</sup> total mass of aerosol detected by ToF-ACSM ( $m_{Org}+m_{NO_3}+m_{NH_4}+m_{SO_4}+m_{Cl}$ )

The ion balance ratio, or also called ammonium balance ( $NH_4\text{ }_{bal} = n_{NH_4}/(n_{NO_3}+2\times n_{SO_4}+n_{Cl})$ ), is the ratio between the measured ammonium ( $n_{NH_4}$ ) and the total ammonium required to neutralize the major anions ( $n_{NO_3}+2\times n_{SO_4}+n_{Cl}$ ). The ratio illustrates the excess of atmospheric ammonium (cation), or nitrate (anion), and other possibilities based on aerosol chemistry (see Sect. S2 for details). Ambient aerosol is normally charge-balanced, meaning that the major cation ( $NH_4^+$ ) and major anion species ( $NO_3^-$ ,  $SO_4^{2-}$ , and  $Cl^-$ ) should have roughly one-to-one molar ratio ( $NH_4\text{ }_{bal} \approx 1$ ). Among three periods analyzed, the ion balance ratio was found to be close to unity for all periods. This infers that the bulk aerosol charge is fully neutralized.

We introduce mean organic-to-inorganic mass ratio ( $m_{Org}/m_{IA}$ ) to quantitatively compare bulk OA and IA composition across seasons. Based on this ratio, in summertime (June), we have composition richer in organics compared to spring and autumn. This difference is likely due to increasing biogenic emissions of VOC in summertime, and higher temperature-induced increases in anthropogenic VOC concentrations.

Formatted: Normal, No bullets or numbering

3.2. Identification of PMF factors

3.1.1.1. Identification of PMF factors

3.1.1.1.1. Factor particle size distributions and composition

From the unconstrained experiments using the combined ACSM-SMPS matrix, the best PMF solution was found with six factors for the combined ACSM-SMPS matrix in each of the datasets to have 4 factors for May 2021 (Fig. S2), June 2021 (Fig. S1), and September 2021 (Fig. S2), with similarities observed across months (S2). The determination of PMF solution is detailed in Sect. S3. The resulting hybrid PMF solution matrix is split into organic mass spectrum, species mass concentrations, and particle number concentration bin matrices for the ease of presentation. The fragments of m/z below 20 are included in the PMF analysis but are not shown in the figures as they do not convey information for the spectrum interpretation. The signal factor axes for inorganic composition and particle size distribution are rescaled and fixed to allow comparison across factors. As each period encompasses around one month of time series data, the factors discerned by the hybrid PMF analyses show typical average aerosol composition during each period, rather than individual pollution episode profiles that may vary over time. Similarities and differences of factors across months will be discussed further below.

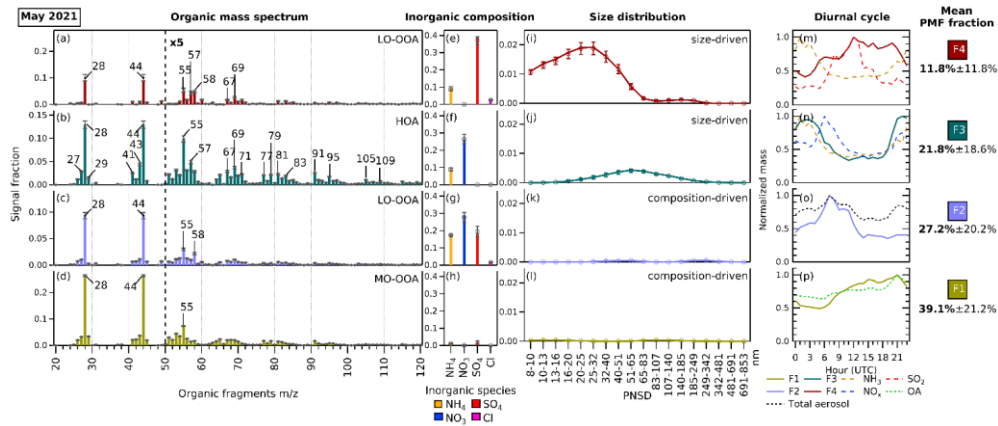


**Figure 2.** The profiles of 4-factor PMF solution from the combined ACSM-SMPS dataset in May 2021. Each factor is split into three matrices with their own rescaled signal fraction axes. The error bars in each variable represents standard deviation generated by performing bootstrapped run of the solution. The panel a-d shows the organic fragment mass spectrum from m/z 20 to 120 from ACSM (m/z < 20 not included). The panel e-h shows the ACSM standard inorganic aerosol species concentrations (ammonium (NH<sub>4</sub>), nitrate (NO<sub>3</sub>), sulfate (SO<sub>4</sub>), and chloride (Cl)). The panel i-l shows the particle size distribution profiles from the SMPS. On the panel m-p, the diurnal cycles of the factors and related species are depicted. The mean PMF fractions and their standard deviations are shown indicating the mean contribution of each hybrid PMF factor to the “total variable reconstruction” by PMF throughout the period. Note that the standard deviations shown here indicate real variability in contribution of each factor, and not uncertainty. The factors in May 2021 are assigned as: (F1) MO-OOA, (F2)

Formatted: Font: +Headings (Times New Roman)

NH<sub>4</sub>+NO<sub>3</sub>+SO<sub>4</sub>+LO-OOA, (F3) size-driven NH<sub>4</sub>+NO<sub>3</sub>+HOA, and (F4) size-driven NH<sub>4</sub>+SO<sub>4</sub>+LO-OOA. Similar figures for June and September 2021 can be found in Fig. S1 and Fig. S2.

### 3.2.1. Factor particle size distributions and composition

~~Four~~Two factors have particle size profiles ~~distributed in~~associated with specific diameter subranges, which we interpret as related to ~~new particle formation~~NPF and growth. We therefore call these factors “size-driven”. The size-driven factors resolved from the analysis possess ~~some~~similarities in composition across months, ~~from ammonium sulfate-rich aerosol (F6) to varying mixture of organic aerosol (OA) and inorganic aerosol (IA) (F5, F4, and F3) (see Fig. 4). We interpret the where the factor associated with the smallest-diameter size driven factor as a nucleation mode factor (F6), which then grows with different composition, on average progressing from F6 to F3. The two particle sizes has bulk composition-driven factors are distributed across particle sizes of ammonium sulfate aerosol (F4) while the larger sizes is linked to the bulk composition of ammonium nitrate aerosol (F3). The other two factors are unrelated to specific particle size and therefore called “composition-driven” factors, consisting of: (F2), an OA and IA mixed factor with a variable composition, and (F1), an organic aerosol factor with occasional traces of ammonium sulfate aerosol~~OA-dominant factor.

### 3.1.2.3.2.2. Factor organic profiles

The organic mass spectrum ~~of each factor profile~~ can be used to obtain information regarding the ~~degree of oxidation level of the factor. Oxidized, which can be related to atmospheric aging of each factor profile. In general, OA can be categorized into two types: primary organic aerosols (POA), and secondary organic aerosols (SOA). Oxygenated organic aerosols (OOA) are often considered to be SOA, while other OA profiles are generally considered POA (Chen et al., 2022), compounds~~

OOA are characterized by ~~a~~relatively high m/z 28 (f<sub>28</sub>) and m/z 44 (f<sub>44</sub>) ~~signal~~fragment signals, originating primarily from CO<sup>+</sup> and CO<sub>2</sub><sup>+</sup> fragments of ~~carboxylic~~carboxylate groups in organic compounds, produced by thermal decomposition inside the ACSM vaporizer (Alfarra et al., 2004). ~~This~~The f<sub>44</sub> fragment is often related to a high degree of oxidation and photochemical ageing (Alfarra et al., 2004; Ng et al., 2010). It is also important to note that the ACSM used in this paper has a CV instead of an SV inlet (see Sect. 2.2.1), which is known to produce higher f<sub>44</sub> values due to enhanced thermal decomposition (Hu et al., 2017; Zheng et al., 2020). The m/z 43 (f<sub>43</sub>) fragment is characteristic for both ~~oxidized~~oxygenated organic compounds (CH<sub>3</sub>CO<sup>+</sup>) and saturated hydrocarbon compounds (C<sub>3</sub>H<sub>7</sub><sup>+</sup>). Thus, factors with higher f<sub>44</sub> and lower f<sub>43</sub> values are understood to be more oxidized ~~and are often classified as an oxygenated organic aerosol (OOA). Meanwhile, while lower f<sub>44</sub> and higher f<sub>43</sub> values implies that the factor is less oxidized. OOA may appear in more than one factor in a PMF solution and thus it is common to distinguish less oxidized-OOA (LO-OOA) and is often labelled hydrocarbon-like organic aerosol (HOA). In this paper, we use these values only to compare more oxidized-OOA (MO-OOA). To assess the variation in OOA oxidation level between aerosol, the triangle plot (Ng et al., 2010) is normally used to compare f<sub>44</sub>/f<sub>43</sub> values among resolved OOA factors. It is also important to note that the ACSM used in this paper has a CV instead of a SV inlet in the PMF~~

**Formatted:** Comment Reference, Font: Times New Roman Bold, Font color: Text 1

**Formatted:** Font: Bold, Font color: Text 1

**Formatted:** Font: Bold

**Formatted:** Font color: Text 1

**Formatted:** Font color: Text 1

**Formatted:** Font color: Text 1

**Formatted:** Font color: Text 1

**Formatted:** Font: +Headings (Times New Roman)

**Formatted:** Font: +Headings (Times New Roman)

**Formatted:** Font: +Headings (Times New Roman)

solution (see Sect. 2.2), which Fig. S6). OOA generally increase throughout the afternoon as its formation is known to produce higher  $f_{44}$  values due to enhanced thermal decomposition photochemically driven (Hu et al., 2017), and therefore cannot be directly compared to PMF organic profiles in other works (2016; Sun et al., 2016) and accumulate in the evening due to the shallow nocturnal boundary layer. In the morning, the concentration decreases as clean airmasses introduced into the rising boundary layer diluting existing aerosol concentrations (Stull, 1988).

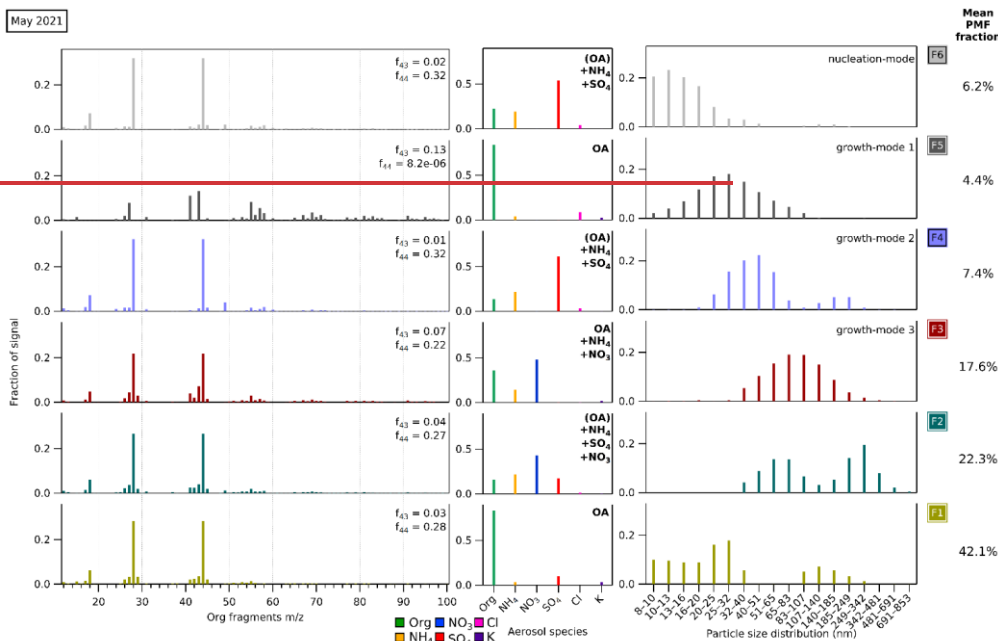


**Figure 3.** The profiles of 6-factor solution from the combined ACSM-SMPS dataset in May 2021. Each factor is split into three matrices with their own signal fraction axes. The left-hand panel shows the organic fragment mass spectrum profiles from ACSM. The values of  $f_{43}$  ( $\text{CO}_3^-$ -fragment) representing higher oxidation level and  $f_{44}$  ( $\text{CH}_3\text{CO}^-$  and  $\text{C}_2\text{H}_7^-$ ) representing lower oxidation level are given. The middle panel shows the ACSM standard aerosol species concentrations (organics (Org), ammonium ( $\text{NH}_4$ ), nitrate ( $\text{NO}_3$ ), sulfate ( $\text{SO}_4$ ), chloride (Cl), and potassium (K)). The right-hand panel shows the particle size distribution profiles from the SMPS. The mean PMF fractions are shown to the right, indicating the mean contribution of each hybrid PMF factor to the “total variable reconstruction” by PMF throughout the period (note we have reordered factors to be consistent across the 3 months). The factors in May 2021 are assigned as: (F1) OA, (F2) (OA)+ $\text{NH}_4$ + $\text{SO}_4$ + $\text{NO}_3$ , (F3) growth-mode 3 OA+ $\text{NH}_4$ + $\text{NO}_3$ , (F4) growth-mode 2 (OA)+ $\text{NH}_4$ + $\text{SO}_4$ , (F5) growth-mode 1 OA, and (F6) nucleation-mode (OA)+ $\text{NH}_4$ + $\text{SO}_4$ . Factors with OA listed inside parentheses indicates OA below 25% of the total mass. Similar figures for June and September 2021 can be found in Fig. S1 and Fig. S2.

3.2. Bulk atmospheric chemical composition across periods

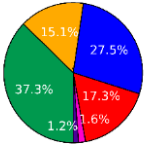
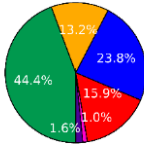
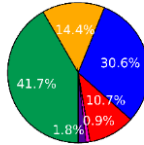
We hypothesize that the bulk atmospheric chemical composition influences how the chemical species are distributed across the PMF factors. The three periods have different average chemical composition as detected by the ToF-ACSM measurements. The mean concentrations of atmospheric species and the species percentages in the bulk atmosphere are summarized in Table S1. For this assessment, we are using three mean concentration ratios summarized in Table 2 to characterize average composition. Ion balance ratio ( $n_{\text{NH}_4^+}/(n_{\text{NO}_3^-} + 2 \times n_{\text{SO}_4^{2-}} + n_{\text{Cl}^-})$ ) is the ratio between the measured ammonium ( $n_{\text{NH}_4^+}$ ) and the total ammonium required to neutralize the major anions ( $n_{\text{NO}_3^-} + 2 \times n_{\text{SO}_4^{2-}} + n_{\text{Cl}^-}$ ). It illustrates the excess of atmospheric ammonium (cation), or nitrate (anion), and other possibilities based on aerosol chemistry (see Sect. S2 for details). This ion balance ratio was found to be unity in May (suggesting charge-balanced condition), less than unity in June (suggesting nitrate excess), and more than unity in September (suggesting ammonium excess). We also examine the mean sulfate to nitrate molar concentration ratio ( $n_{\text{SO}_4^{2-}}/n_{\text{NO}_3^-}$ ), determining a sulfate-rich or sulfate-poor condition relatively. The mean organic-to-ammonium mass ratio ( $m_{\text{Org}}/m_{\text{NH}_4^+}$ ) is used to show whether a period is organic-rich relative to other periods.

We have three different composition regimes measured during the three periods based on these ratios. In springtime (May), we can see a sulfate-rich and nitrate-excess regime. In summertime (June), we have an organic-rich, sulfate-rich with nitrate-excess regime. Lastly, a sulfate-poor and ammonium-excess regime is observed in autumn (September). Below, we will discuss how these regimes influence the chemical composition of factors that were obtained from PMF analyses. POA consists of various sources which can be identified from the appearance of certain fragmentation patterns in the organic mass spectrum, diurnal cycle, as well as correlation with other measurements. Some of the most common POA from PMF analysis are hydrocarbon-like organic aerosols (HOA), biomass burning organic aerosol (BBOA), cooking organic aerosols (COA), and coal combustion organic aerosol (CCOA) (Chen et al., 2022). POA have similar characteristics of alkyl and alkenyl fragments ( $\text{C}_n\text{H}_{2n+1}^+$ : m/z 29, 43, 57, 71, ... and  $\text{C}_n\text{H}_{2n-1}^+$ : m/z 27, 41, 55, 69, ...). HOA as a type of POA is often correlated with anthropogenic combustion pollutants, such as  $\text{NO}_x$  and black carbon from vehicular emission (Alfarra et al., 2004; Mohr et al., 2009; Zheng et al., 2020). Other POA profiles are distinguished by looking at certain fragments (e.g. m/z 60 and 73 for BBOA (Schneider et al., 2006; Weimer et al., 2008; He et al., 2010), m/z 55 for COA (He et al., 2010; Mohr et al., 2012), m/z of larger fragments related to polycyclic aromatic hydrocarbons (PAHs) for CCOA (Hu et al., 2013)). While CV increases the  $f_{44}$  values and smaller organic fragments due to enhanced thermal decomposition, larger fragments become underestimated (Hu et al., 2017; Zheng et al., 2020) and therefore the differences between POA factors becomes more subtle.

The PMF analyses in this study resolved one POA factor (as HOA factor) and three SOA factors (one LO-OOA factor and two MO-OOA factors) across periods, where each organic profile has its corresponding IA composition and size distribution. Among size-driven factors, the factor related to the smallest particle sizes (F4) has OA assigned as LO-OOA, while the OA associated with the second size-driven factor (F3) is assigned as HOA. In the composition-driven factors, the OA+IA mixture factor (F2) resolves an LO-OOA profile while the OA factor (F1) resolves an MO-OOA profile.

365

**Table 2.** Mean bulk atmospheric chemical composition in the three periods, summarized as the values of ion balance ratio ( $n_{NH_4}/(n_{NO_3}+2\times n_{SO_4}+n_{Cl})$ ) from linear regression, mean sulfate to nitrate ratio ( $n_{SO_4}/n_{NO_3}$ ), and mean organic to ammonium ratio ( $m_{Org}/m_{NH_4}$ ). The concentrations were detected by the ToF-ACSM in Cabauw. A more detailed information can be seen in Table S1.

Mean-ratio	May 2021 (spring)	Jun 2021 (summer)	Sep 2021 (autumn)
Bulk-aerosol-composition <sup>‡</sup>			
$n_{NH_4}/(n_{NO_3}+2\times n_{SO_4}+n_{Cl})^{**}$	0.99	0.98	1.08
$n_{SO_4}/n_{NO_3}^{**}$	0.41	0.43	0.23
$m_{Org}/m_{NH_4}^{*}$	2.47	3.36	2.90
Composition-regime	sulfate-rich	nitrate-excess; organic-and-sulfate-rich	ammonium-excess; sulfate-poor

<sup>‡</sup>mass-concentration, <sup>\*\*</sup>molar-concentration

**3.40.3.3. Size-driven factors (F7, F6, F5, and F4 and F3)**

Using the hybrid ACSM-SMPS datasets, fourtwo size-driven factors emerge from the PMF analyses as F6, F5, F4, and F3 (see Fig. 3, Fig. S1, and Fig. S2). These factors are considered “size-driven” due to the approximately normally distributed particle concentrations in a specific sub-range of diameter. The fourtwo factors display different particle size clusters increasing in diameter from F6F4 to F3. The size-driven factors have diverse composition characterized by a variety of OA and IA mixtures, as can be seen in Fig. 4, discussed in more detail below.

375

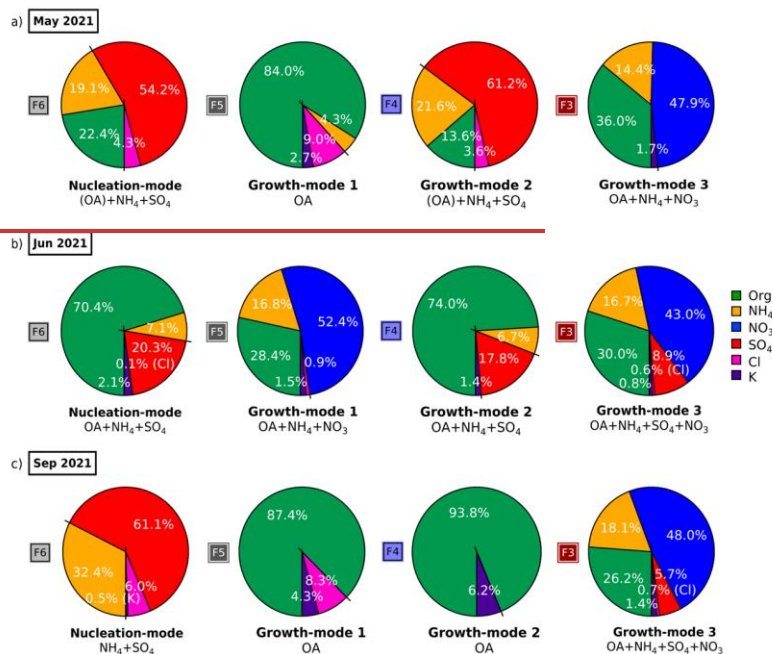


Figure 4. Pie charts showing mass percentage of each aerosol species contributing to each size-driven factor profile in (a) May 2021, (b) June 2021, and (c) September 2021. Green represents organics (Org), orange represents ammonium (NH<sub>4</sub>), dark blue represents nitrate (NO<sub>3</sub>), dark red represents sulfate (SO<sub>4</sub>), pink represents chloride (Cl), and purple represents potassium (K). Factors with OA listed inside parentheses indicates OA below 25% of the total mass.

New particle formation (NPF) events are characterized by the rapidly increasing particle number concentration below 20 nm followed by particle growth, creating nearly vertical aligned peaks in particle number concentration plotted against time (Heintzenberg et al., 2007; Kerminen et al., 2018). In Fig. 5B by comparing the time series of particle size distribution (dN/dlogD<sub>p</sub>), total mass loading, and PMF mass fraction (see Fig. 4 (May) and Fig. S3 (June and September)), we can observe that the episodes during which the smallest-size-driven factor (F6) fraction increases occur when the total aerosol mass concentration is relatively low. This is to be expected, as during these periods, the condensational sink, which would compete by scavenging low-volatility gases or small particles, is reduced. If we zoom into the time series, the NPF growth shapes appear during episodes that are dominated by the smallest size factor, F6 and/or F3 (see Fig. S4). The trace inorganic ions (chloride and potassium) in the factors are found to be correlated with the existence of sulfate

Formatted: Normal

Formatted: Font: +Headings (Times New Roman), English (Indonesia)

Formatted: Font: +Headings (Times New Roman)

Formatted: Font: +Headings (Times New Roman), English (United Kingdom)

Formatted: English (United Kingdom)

Formatted: English (United Kingdom)

Formatted: Font: +Headings (Times New Roman), English (United Kingdom)



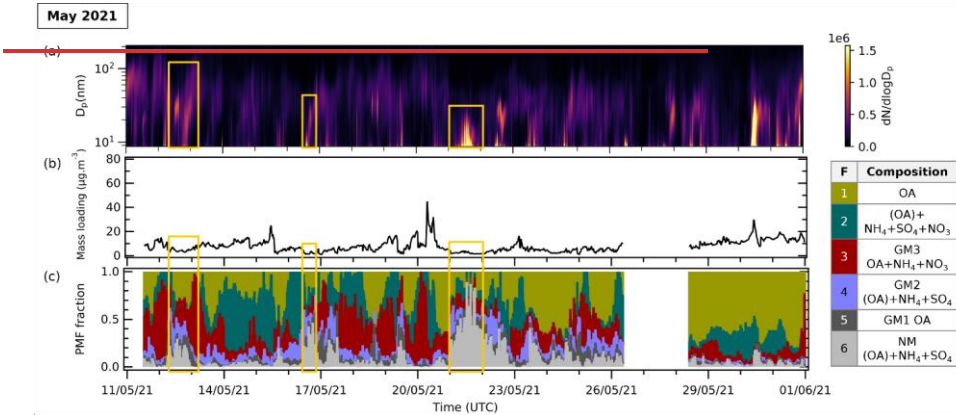
395

400

405

and organic species, respectively, hinting at possible correlations with sea spray and biomass burning aerosol, respectively (see details in Sect. S4).

The reconstructed PMF masses show the influence of sunlight and temperature on NPF events. The average PMF mass fraction of the size-driven F4 is higher in summertime (June) compared to other periods (see Fig. 3) due to higher mean radiation and temperatures (see Table 1). In summer (June), F4 accounts in average 14.9% of total reconstructed PMF mass while in spring (May) and autumn (September), it only represents 11.8% and 7.8%, respectively. The more frequent appearance of NPF growth events during summer can be seen in Fig. S3a-c. Other studies have likewise found the occurrence of NPF events is generally favored in high radiation (Modini et al., 2009; Peltola et al., 2022) and warmer temperatures (Jokinen et al., 2022; Peltola et al., 2022). This is because solar radiation provides the UV radiation that promotes photochemical reactions and turbulent motions needed to form new particles (Wehner et al., 2015; Dada et al., 2017; Kerminen et al., 2018; Sellegri et al., 2019).



Formatted: Font color: Text 1

Formatted: Font: +Headings (Times New Roman)

Formatted: Font: +Headings (Times New Roman)

Formatted: Font: +Headings (Times New Roman)

Formatted: Font: +Headings (Times New Roman), English (United Kingdom)

Formatted: English (United Kingdom)

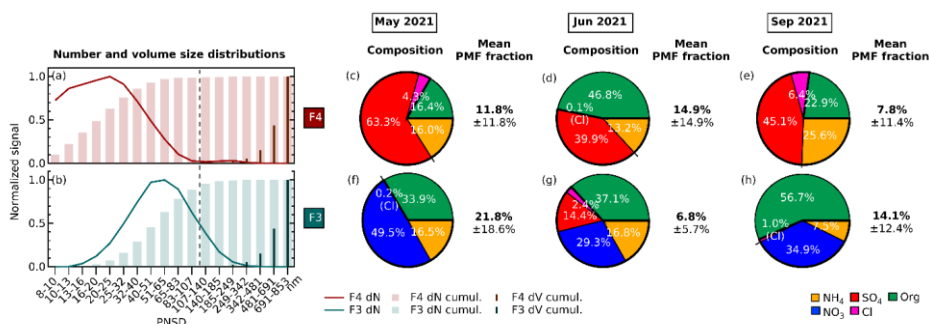


**Figure 3.** (a-b) Normalized average particle size distribution of two size-driven factors of F4 (maroon) and F3 (turquoise) across periods. The line plot shows particle number concentration (dN) fraction on each size bin. The thick histogram represents cumulative particle number concentration (dN) fraction as the particle size increases, while the thin histogram represents cumulative particle volume (dV =  $dN \times (4/3) \times \pi \times (D_p/2)^3$ ) fraction. The vertical dashed dark grey line divides the particle diameters where particles are transmitted with <50% efficiency on the left (diameter less than ~100 nm) and with at least 50% efficiency by PM<sub>2.5</sub> lens of ToF-ACSM on the right (diameter more than ~100 nm). (c-h) Pie charts showing mass percentage of each aerosol species contributing to each size-driven factor in May 2021, June 2021, and September 2021. Green represents organics (Org), orange represents ammonium (NH<sub>4</sub>), dark blue represents nitrate (NO<sub>3</sub>), dark red represents sulfate (SO<sub>4</sub>), and pink represents chloride (Cl). F4 are dominated by ammonium sulfate while F3 are dominated by ammonium nitrate. The mean PMF fractions and their standard deviations are shown indicating the mean contribution of the factor to the total reconstructed PMF mass.

Formatted: Font color: Text 1

Formatted: Font: Not Bold, Font color: Text 1, Subscript

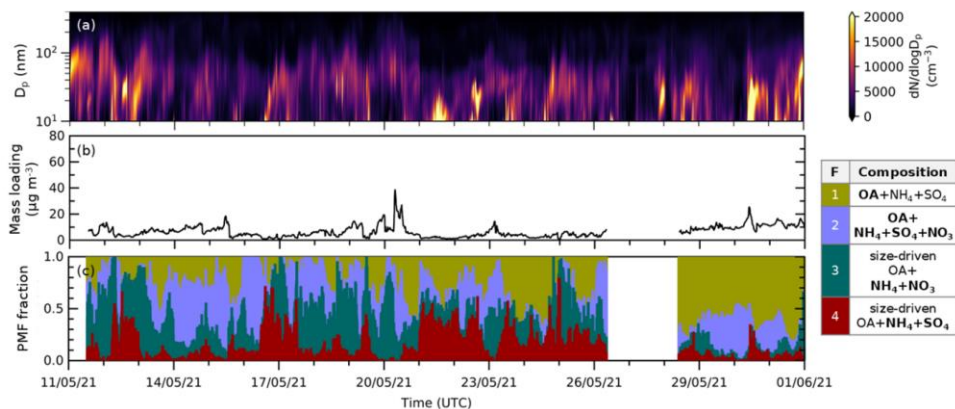


**Figure 4.** Time series of (a) particle size distribution (dN/dlogD<sub>p</sub>) in cm<sup>-3</sup> with logarithmic scale in particle size obtained from SMPS measurements, (b) total mass loading calculated from ACSM species concentration (using Tofware) in µg m<sup>-3</sup>, and (c) reconstructed PMF fraction (stacked) from analysis in May 2021. Orange-outlined sections indicate periods during which high episodes of size-driven factors are observed. These episodes of F4 and F3 coincide with relatively low total aerosol mass conditions and high fine particle concentrations. Similar figures for June and September 2021 can be found in Fig. S3.

Formatted: Font: +Headings (Times New Roman)

3.40.2.F6: nucleation-mode factor

3.3.1. F6 corresponds Particle size distributions

F4 corresponds to the bulk composition when the particles in the nucleation mode is growing into Aitken mode size range ( $\leftarrow D_p \leftarrow$ , with modal size of 20-25 nm (see Fig. 3(a)). F3 is characterized by clustered particle sizes in the Aitken and accumulation mode region, with modal size of 51-65 nm (see Fig. 3(b)). The F4 and F3 mass loading shows a good correlation with particle number concentration in the size bin of 20-25 nm and 51-65 nm, respectively, across periods (see Fig. S5). The size range differs slightly across months but is F4 always appears as the smallest particle size range among factors, which we therefore designate as nucleation-mode, “nucleation-mode” factor, while F3 with larger particle size range is designated as “growth-mode” factor.

Some concerns may arise because the ACSM and SMPS measure different particle size ranges, especially the smaller sizes which are the major interest of this study. According to a study conducted using a ToF-ACSM in the same configuration as this study, the PM<sub>2.5</sub> lens in the ToF-ACSM transmits particles with vacuum aerodynamic diameter ( $D_{va}$ ) between 100 nm and 3  $\mu$ m with efficiency above 50%, decreasing to around 20% for  $D_{va} \sim 55$ –60 nm (Xu et al., 2017). Meanwhile, the SMPS instrument samples particles with diameters ranging from 10 to 800 nm. As we are mainly interested in elucidating the composition of NPF and growth in sizes finer than 100 nm, we address here the influence of this mismatch on interpretation of our PMF results.

In Fig. 3a, we observe that F4 mainly related to aerosol with sizes that have transmission efficiency <50% in PM<sub>2.5</sub> ToF-ACSM, while in Fig. 3b, only the size bins of 107–140 nm in F3 have transmission efficiency  $\geq$ 50%. The small-sized particles will make a negligible contribution to the PM<sub>2.5</sub> mass and the larger particles will always dominate the particle volume size distribution, regardless of whether the finer particles are efficiently sampled or not by ACSM. Nevertheless, although the ACSM does not directly measure the finest particle composition, the factor still illustrates the bulk chemical composition that occurs during and favors the formation and growth of new particles. Moreover, the PMF tool does not recognize that the diameter bins are sequential, so the factors whose particle diameters cluster in certain range confirm that F4 and F3 composition indeed happen during NPF and growth when the fine particle loading is the greatest.

3.3.2. Chemical composition

In all periods, F6 the nucleation-mode F4 has ammonium sulfate as the major component. (see Fig. 3c-e). The factor further consists of ammonium (7.113% to 32.426%), sulfate (20.340% to 61.663%), organic compounds (0.016% to 70.447%), and traces of chloride (0.1% to 6.0%) and potassium (0.0% to 2.1%).

**Commented [NF1]:** 5.1) How does the composition shift from sulfate to organics or sulfate/organics to nitrate between F6 F5? What happened to the sulfate? Looking at the solutions, it appears that F6 --> F4 and may be F5 --> F3; however, as it is presented and discussed, it appears the NPF event goes from F6 - F5 --> F4 --> F3.

**Commented [NF2R1]:** 5.2) Similarly, what happened to f(C Highly oxygenated material may be necessary for the initiation of NPF; however, it should not completely disappear as compounds with higher volatility, lower f(CO2) condenses onto the aerosol.

**Formatted:** Font color: Text 1

**Formatted:** Font color: Text 1

**Formatted:** Font color: Text 1

**Formatted:** Font color: Text 1

**Formatted:** Font color: Text 1

**Formatted:** Font color: Text 1

**Formatted:** Font color: Text 1

455 The4%). Organics are known to participate in particle formation and growth (Riipinen et al., 2012; Hodshire et al., 2016),  
while in this study, the mass percentage share between ammonium, sulfate, and organics of F6 dependF4 depends on the mean  
bulk organic composition regime in each period (see Fig. 43c-c). The sulfate-rich regime with low mean bulk organiesorganic  
composition in springtime and autumn (May and September) leads to F6F4 being largely ammonium (16% and 26%) and  
sulfate (19.163% and 54.2%, respectively),45%), followed by OA (22.416% and 23%) and chloride (4.83% and 6.4%). The  
460 organic-rich and sulfate-rich regime in summer (June, see Table 2) results in F6 being dominated by the increase of OA (70.4%)  
rather than in F4 (47%) and less ammonium and, sulfate (7.1, and chloride (13%, 40% and 20.30.1%, respectively), with traces  
of chloride (0.1%) and potassium (2.1%). In autumn (September), the ammonium-excess and sulfate-poor regime with low  
bulk organics results in the F6 composition being exclusively ammonium and sulfate (32.4% and 61.1%, respectively), with  
traces of chloride (6.0%) and potassium (0.5%). We). F4 represents from 9.5% up to 14.3% of total reconstructed PMF mass  
465 in the solution with the highest being during summer when there is more contribution from organic masses. On the other hand,  
the growth-mode F3 is composed of mainly ammonium nitrate aerosol (see Fig. 3f-h). The factor further composed of  
ammonium (8% to 17%), nitrate (29% to 50%), organic compounds (34% to 57%), and traces of chloride (0.2% to 2.4%). In  
contrast to other months, the PMF analysis also resolves variations in F3 containing sulfate (14%) during summertime (June).

470 Overall, we interpret these results to meanindicate that sulfate is a key component of condensation-nucleinucleating particles  
during NPF events, regardless of the bulk atmospheric composition. When the mean bulk organic concentration is high, and  
more oxidized (e.g., summertime), it participates more abundantly in particle nucleation. With excess ambientWhile sulfate is  
key to nucleation, nitrate plays a more important role in particle growth (see Sect. S2).

3.3.3. Organic profiles

475 The organic mass spectrum profile from each size-driven factors and their diurnal cycles in each period are shown in Fig. 5.  
Across seasons, LO-OOA is part of the nucleation-mode particles composition. The factors are assigned as LO-OOA due to  
their  $f_{44}/f_{43}$  values compared to other OOA factors (see the triangle plot in Fig. S6). The LO-OOA F4 profile resolved in this  
study is comparable to LO-OOA resolved in other aerosol mass spectrometry studies using CV (Zheng et al., 2020; Joo et al.,  
2021), although fragments with  $m/z > 50$  are observed less. From this trend, we infer that only lower volatility, oxygenated  
480 organic compounds can condense on freshly nucleated particles. In terms of diurnal cycle, the F4 mass loading does not follow  
the typical LO-OOA pattern, but rather together with the formation of ammonium, however, particle condensation can occur  
without organic compounds.

Oxidation levels further explain the OA contribution difference in nucleation-mode particles. We can observe this variation  
485 by looking at the organic fragment spectrum of F6. High  $f_{44}$  value is observed in F6 where OA participates in new particle  
condensation during spring (May,  $f_{44}=0.32$ ) and summer (June,  $f_{44}=0.33$ ). In these months, higher mean radiation promotes  
photooxidation of organic vapors and sulfate is responsible for the increase in new particle loading during the day, as seen in

- Formatted: Font color: Text 1
- Formatted: Font color: Text 1
- Formatted: Font color: Text 1
- Formatted: Font: Not Bold, Font color: Text 1
- Formatted: Font color: Text 1
- Formatted: Font color: Text 1
- Formatted: Font color: Text 1
- Formatted: Font color: Text 1
- Formatted: Font color: Text 1
- Formatted: Font color: Text 1
- Formatted: Font color: Text 1
- Formatted: Font color: Text 1
- Formatted: Font color: Text 1
- Formatted: Font color: Text 1
- Formatted: Font color: Text 1

- Formatted: Font color: Text 1

the diurnal cycles (Fig. 5g,i,k). The organic-rich regime in summer (see Table 2) combined with higher mean temperature also favors the abundant production of semi-volatile oxidized organic compounds OA which can condense rapidly onto newly formed particles, resulting in higher OA contribution to nucleation-mode particles. In September, when mean radiation is lower, OA does not appear in F6. The organic mass spectra are consistent with this lower degree of oxidation, with lower  $f_{44}$  and high  $f_{43}$  value leading to the increase of OA to 47%, compared to 16% in spring and 23% in autumn (September,  $f_{44} = 5.8 \times 10^{-6}$  and  $f_{43} = 0.16$ ).

We infer that only lower volatility, oxidized organic compounds can condense on freshly nucleated particles. The organic-rich regime combined with higher mean temperature favors the abundant condensation of available semi-volatile OA onto newly formed particles; see Fig. 3). Consistent with these results, several aerosol chamber experiments have reported that highly oxygenated organic molecules (HOM) from biogenic and anthropogenic organic precursors play a dominant role in new particle formation and growth (Schobesberger et al., 2013; Ehn et al., 2014; Riccobono et al., 2014; Tröstl et al., 2016; Mohr et al., 2019; Pospisilova et al., 2020; Zhao et al., 2021).

**F5 to F3: growth-mode factors**

F5, F4, and F3 are characterized by clustered particle sizes in the Aitken and accumulation mode region ( $20 < D_p < 691$  nm). The size range differs across period but has particle size progressively growing from F5 to F3, which we thus designate the “growth-mode” factors. The growth-mode factors contain different composition across seasons, depending on the available semivolatile species for condensation.

In springtime (May), less-volatile and less-oxidized organic compounds ( $f_{44} = 8.2 \times 10^{-6}$  and  $f_{43} = 0.13$ ) condense onto newly formed particles, increasing the organic contribution in F5. The increase of OA in F5 is also observed for autumn (September), although in the case more highly-oxidized organic compounds ( $f_{44} = 0.21$  and  $f_{43} = 0.07$ ) condense onto new particles. We suggest that although oxidized organic compounds are not involved in early particle condensation when the mean radiation is lower, they are incorporated in later growth. For spring and autumn, F5 consists of largely OA composition (84.0% to 87.4%), ammonium (4.3% only in May), chloride (8.3% to 9.0%), and potassium (2.7% to 4.3%).

In summertime (June), there is a substantial amount of nitrate (52.4%) in F5 alongside less-oxygenated OA (28.4%,  $f_{44} = 2.8 \times 10^{-6}$  and  $f_{43} = 0.17$ ), ammonium (16.8%), chloride (0.9%), and potassium (1.5%). The ion balance ratio in June was less than unity, which can be due to excess nitrate aerosol (see Sect. S2). We propose that it indicates the promotion of semi-volatile organic nitrate formation in the summertime, condensing onto the newly formed particles as the temperature lowers. Organic nitrate comes from reaction between  $\text{NO}_x$  with less-oxygenated organic compounds and condensing into aerosol phase more easily in this period. Further, we infer the possibility of biogenic source of the organic compounds involved in this organic

Formatted: Font color: Text 1

Formatted: Font color: Text 1

Formatted: Font color: Text 1

Formatted: Font: +Headings (Times New Roman), English (United Kingdom)

Formatted: Font: +Headings (Times New Roman), English (United Kingdom)

Formatted: English (United Kingdom)

nitrate-source, due to the fact that we observe this composition only in the hottest and sunniest month of June and less oxygenated.

As particles grow into the larger size ranges F4 and F3, they incorporate more OA and ammonium salts. F4 resembles the composition of either the two smallest size-driven factors (F6 or F5), which may be due to continuation of smaller particle growth with the same composition. F3, the largest particle size range among size-driven factors, contains nitrate as the main component (43.0% to 48.0%) followed by OA (26.2% to 36.0%), and ammonium (14.4% to 18.1%). The dominant contribution of nitrate is observed across periods regardless of the nitrate composition regime. Overall, the composition of these size-driven factors suggests that, while sulfate is key to nucleation, nitrate plays a more important role in particle growth, which is related to the ammonium-sulfate-nitrate aerosol chemistry (see Sect. S2).

Relationships with mean radiation and temperatures

The reconstructed PMF masses show the influence of mean downward shortwave radiation and temperature on NPF events. The average PMF mass fraction of nucleation-mode particles (F6) is higher in summertime (June) compared to other periods (see Fig. S1) due to higher mean radiation and temperatures (see Table 1). In summer (June), F6 accounts in average 22.3% of total reconstructed PMF mass while in spring (May) and summer (September), they only represent 6.2% and 4.1%, respectively. The more frequent appearance of NPF growth events during summer can be seen in Fig. S3a. The occurrence of NPF events is generally favored in high radiation (Modini et al., 2009; Peltola et al., 2022) and warmer temperatures (Jokinen et al., 2022; Peltola et al., 2022). Solar radiation provides the UV radiation that promotes photochemical reactions and turbulent motions needed to form new particles (Wehner et al., 2015; Dada et al., 2017; Kerminen et al., 2018; Sellegri et al., 2019).

Formatted: Font: +Headings (Times New Roman)

Formatted: Font: +Headings (Times New Roman)

Formatted: Font: +Headings (Times New Roman)

Formatted: Font: +Headings (Times New Roman), English (United Kingdom)

Formatted: English (United Kingdom)

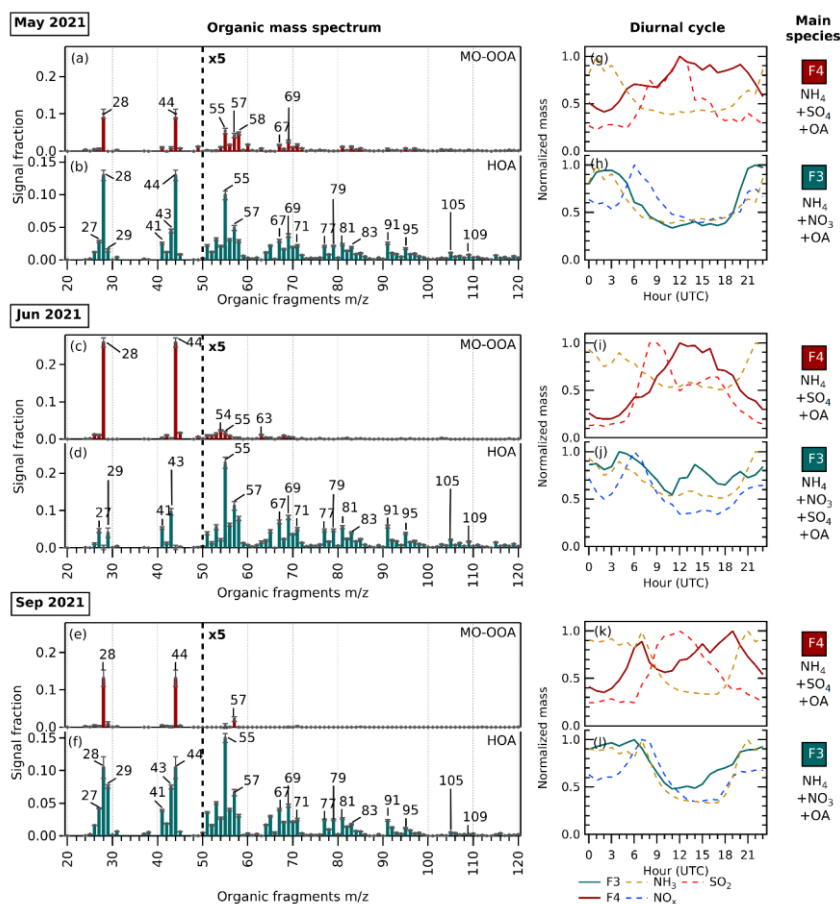


**Figure 5.** (a-f) Organic mass spectrum from  $m/z$  20 to 120 ( $m/z < 20$  not included) of F4 (maroon) showing MO-OOA factor profiles and F3 (turquoise) showing HOA factor profiles in May 2021, June 2021, and September 2021. The error bars in each  $m/z$  were generated from bootstrap run. (g-i) Diurnal cycles of corresponding factors and potential precursor gases. The diurnal cycles of F4, mainly composed of ammonium sulfate, are shown together with its precursors,  $\text{NH}_3$  and  $\text{SO}_2$ . The diurnal cycles of F3, mainly composed of ammonium nitrate, are shown together with its precursor,  $\text{NH}_3$  and  $\text{NO}_x$ .

F3, seen as the growth-mode factor related mainly to ammonium nitrate, is associated with an HOA-like organic profile. The factor is assigned as HOA due to the alkyl and alkenyl fragments that are abundant ( $m/z$  27, 29, 41, 43, 55, 57, 69, and 71).

The diurnal cycle of F3 in this study shows similarity with general non-urban HOA diurnal patterns, with increase of loading at nighttime (see Fig. 5h,j,l), contrary to typical diurnal pattern of HOA in urban site with peaks during morning and evening rush hour (Chen et al., 2022). It suggests that the growth-mode F3 may be related to transported vehicular emissions from urban areas and/or local primary organic emissions. Organic nitrates can also be formed from reaction between  $\text{NO}_x$  with less oxygenated volatile organic compounds (VOCs) through  $\text{NO}_3$  or alkyl peroxy radicals (Berkemeier et al., 2016). The diurnal pattern of F3 is consistent with this organic nitrate formation, followed by condensation onto the newly formed particles as the temperature lowers at night. During the summer, a small increase in F3 mass loading during the daytime also can be observed, hinting at enhancement of daytime organic nitrate formation in the hottest and sunniest period.

During the summer, the values of  $f_{28}$  and  $f_{44}/f_{43}$  as oxygenated organic markers in F4 are higher compared to other seasons, while they are almost absent in F3. In the chemical composition discussed in Sect. 3.3.2, sulfate also makes appearance in F3 unlike other seasons. We hypothesize that the PMF solution did not resolve the two size-driven factors in summer (Jun) similarly to other seasons, and therefore the aerosol composition is more mixed between NPF and growth particles. Mathematically, this is reflected in the local minima of the chosen PMF solution. Despite being the lowest minima in the PMF solution space,  $Q/Q_{\text{exp}}$  in June scores the lowest compared to May and September (see Table S3).

#### 3.3.4. New particle formation (NPF) and growth pathway

The NPF events shown by the time series of particle number size distribution and size-driven factor loading reveal that particle formation and growth takes around 6 to 12 hours (see Fig. S4). The high occurrence of ammonium sulfate and oxidized organic molecules in the aerosol phase observed during nucleation-mode F4 episodes marks the beginning of NPF. This is related to ammonium sulfate formation from the reaction between ammonia and sulfuric acid, and uptake of oxygenated organic compounds. We can consider F3 as a “sequential” pathway of F4 growing in size; this sequential nature is observed in some NPF events shown in Fig. S4, when F3 peaks after F4. F4 grows into F3 when nitric acid and/or organic nitrates and hydrocarbon-like semi-volatile organic compounds are dominant in the aerosol composition.

One might argue that F3 cannot be considered as the successor of F4 as it does not contain any sulfate (for May and September), which should remain from initial nucleation. Another possible explanation is that F3 emerges directly from ammonium nitrate as a “parallel” nucleation pathway. Other studies have observed this nucleation mode to occur very rarely and only in the free troposphere, at lower temperature and very clean air conditions, through reaction between nitric acid and  $\text{NH}_3$  (Höpfner et al., 2019; Wang et al., 2020). In a “combined” hypothesis, F3 emerges from F4, but the particles rapidly favor the pathway of growing mainly by ammonium nitrate condensation to the particle phase. The simultaneous pathway of F4 and F3 growth can be observed in some NPF events in Fig. S4.

The diurnal cycles of the size-driven factors shown in Fig. 6 (May) and Fig. S5 (June and September) also shows the influence of shortwave radiation and temperature on particle formation. Going from F6 to F3, we observe that the factors’ diurnal pattern

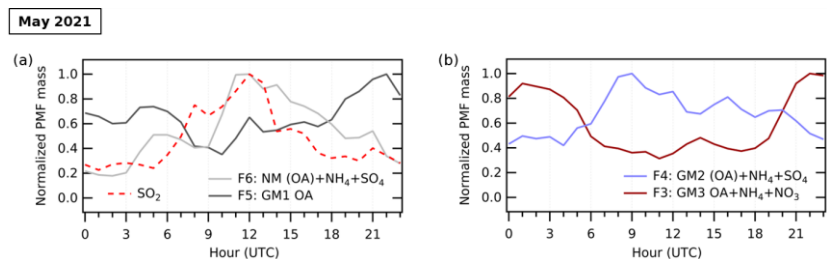
Formatted: Font color: Text 1



tends to shift from a daytime peak (F6 peaks in the middle of the day) to higher nighttime concentration as the particle size grows. Regional-scale NPF normally takes place during the daytime between sunrise and sunset, where it can carry on for several hours (Hamed et al., 2007; Hussein et al., 2009; Németh and Salma, 2014; Qi et al., 2015; Dai et al., 2017; Kerminen et al., 2018; Kalkavouras et al., 2020), although there are also instances of NPF happening during the night in various locations (Hirsikko et al., 2012; Vehkamäki and Riipinen, 2012; Rose et al., 2018; Kammer et al., 2018) or quiet NPF during non-event days (Kulmala et al., 2012; Dada et al., 2018; Kulmala et al., 2022). Daytime peaks in F6 can be seen in spring (see Fig. 6) and summer (see Fig. S5) when the mean radiation is higher. This peak is less visible during autumn when mean radiation is lower (see Fig. S5). The sulfate-rich new particle factor F6 also appears around the same time as the precursor gas  $\text{SO}_2$ , with the most obvious match between  $\text{SO}_2$  and the F6 diurnal cycle observed in spring (May, see Fig. 6).

Unlike the nucleation-mode F6, the growth-mode F5 and F4 have different diurnal patterns across periods, corresponding to their diverse compositions. F5 and F4 also exhibit consistently less diurnal variation, except for F5 during summer (see Fig. S5), when it tracks with the highest mean radiation across periods. In summertime (June), when there was more daylight and radiation available to promote NPF and growth, F5 has a pronounced peak in the afternoon, later than the F6 peak.

F3 shows more elevated nighttime concentrations across seasons (see Fig. 6 and Fig. S5). Lower nocturnal temperatures foster the condensation of semivolatile chemical species into the aerosol phase, increasing the nighttime particle concentration. The increase in the particle concentration during the night can also be facilitated by a shallower nocturnal boundary layer.



This process leads to the negligible amount of sulfate and abundance of ammonium nitrate during particle growth, hence sulfate mass being unresolved in the F3 composition (for May and September). Chamber experiments and theoretical studies support this interpretation of NPF occurring with only minor involvement of sulfate (Liu et al., 2018; Wang et al., 2020, 2022). The chemistry of ammonium sulfate and nitrate aerosol formation is discussed in more detail in Sect. S2.

**Figure 6.** Normalized diurnal cycles in May 2021 of (a) the size-driven factors of F6 and F5, and  $\text{SO}_2$  as the sulfate precursor, and (b) the size-driven factors of F4 and F3. Notice that from F4 to F3, the factors' diurnal pattern shifted from high daytime to high nighttime concentration. Similar figures for June and September 2021 can be found in Fig. S5.

**Commented [NF3]:** 7) Fig 6 and associated figures in SI, it is surprising how the normalized mass spans what appears to be a long time frame than the NPF event. E.g., Fig. S4 shows that the event are ~ 4 - 6 hours; however, looking at Fig. 6 (and associated figures) it seems that it takes a full 12 hrs to go from F6 --> F3. Clarification in how this figure/results are related to NPF needs to be further detailed.

3.40.6.3.3.5. Relationship of new particle formation with wind variables

To study the relationship between wind variables and new particle formation in the rural site of Cabauw, we compare timeseries of wind variables analyses were done using bivariate polar plots of size-driven F4 and the reconstructed PMF fraction of the nucleation-mode (F6)F3 by wind speed and first growth-mode (F5) in Fig. 7 (May) and Fig. S6 (June and September)-wind direction (see Fig. 6). We observe that new particle formation episodes nucleation-mode F4 are correlated mainly with air masses transported from southwesterly-westerly sector or northerly, and sometimes from the easterly sector. These wind sectors are the suppliers of organics, supply sulfate, ammonium, and organics (Fig. S8), and their precursor gasgases that determine the main composition of F6F4 (see Fig. S7 and Fig. S8S9). Westerlies represent a source of sulfate, which mainly comes from sulfur oxides (SO<sub>x</sub>) emission along the waterway of Rotterdam's harbor, the busiest port in Europe. The sulfate in air transported to Cabauw from the northern to eastern sector may arise from SO<sub>x</sub> precursor from other urban, shipping, industry centers (e.g., Amsterdam city and port, Utrecht city), and power plants to the site (see Fig. 1) (Henschel et al., 2013; Fioletov et al., 2016; Ledoux et al., 2018). The supply of ammonium for new particle condensation through NH<sub>3</sub> emission comes from the agricultural practices that take place around the Cabauw site, with tendency of higher NH<sub>3</sub> and ammonium from the southern sector. The easterlies extending to north are also sources of VOCs coming from the forested nature areas in the provinces Utrecht and Gelderland, which are subsequently transformed into SOA.

Formatted: Font: +Headings (Times New Roman)

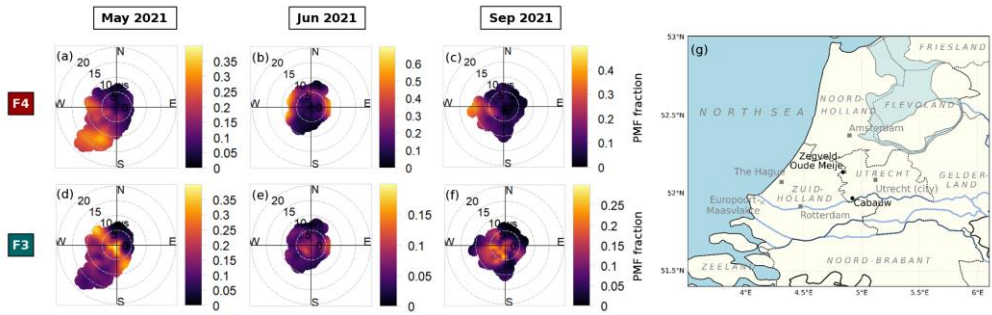


**Figure 6.** (a-f) Bivariate polar plots of size-driven factor mass fraction (F4 and F3) by wind speed and wind direction measured in Cabauw in May, June, and September 2021. We can observe that nucleation-mode particles (F4, a-c) fraction is largely correlated with air masses from the southwesterly-westerly sector where the urban and harbor areas of Rotterdam located. The growth-mode particles (F3, d-f) fraction is distributed around the site and from southwesterly sector. Similar figures for composition-driven factors can be found in Fig. S7.

The different prevailing wind also affects the F6F4 composition and frequency. In spring (May) and autumn (September), new particle formation mainly correlates with winds from southerly and westerly directions (see Fig. 26a,c), and thus has less organic composition. In summer (June), winds coming from the north or east contribute to NPF events (see Fig. 26b), supplying more organics to the site. As previously discussed in Sect. 3.3.3, the abundant organics combined with due to higher

radiation and temperatures allow semi-volatile ~~oxidized-organics~~SOA to directly condense onto newly formed particles, increasing NPF events and ~~F6F4~~ mass fraction during summer (see Fig. S63d).

Formatted: Font: +Headings (Times New Roman)

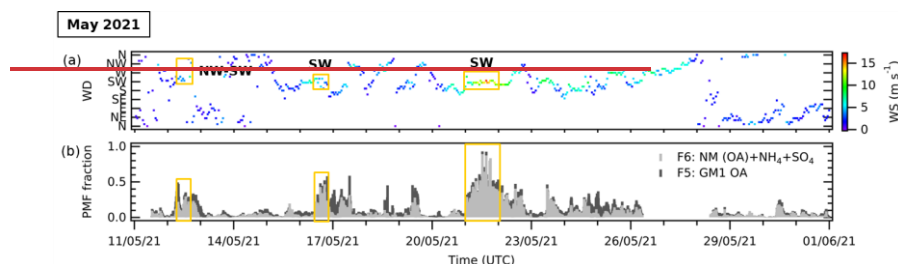


**Figure 7.** Timeseries of (a) wind direction (WD) color-coded with wind speed (WS), and (b) reconstructed PMF fractions F6 and F5 (stacked) corresponding to nucleation-mode and first growth-mode particles in May 2021. Orange-outlined sections indicate high F6 and F5 episodes. We observe that new particle formation episodes are correlated with air masses from the southwesterly-westerly sector. Similar figures for June and September 2021 can be found in Fig. S6, showing more contributions from northerly-easterly wind directions.

#### 3.4.4.3.4. Bulk composition-Composition-driven factors (F2 and F1)

The two ~~bulk composition-driven~~ factors yielded by the PMF analyses are F2 and F1 (see Fig. 3-2 (May), Fig. S1 (June), and Fig. S1, and Fig. S2): (September)). We call these factors ~~bulk composition-driven~~ because they are ~~composition-driven~~ and found across the size distribution, rather than in a specific size range. They collectively account for a large fraction of total aerosol mass loading (31.1% to 64.4%);reconstructed PMF mass (66% to 78%) and can be considered as the result of size-driven factors further growth into the bulk aerosol. F2 and F1 are both representative of mean atmospheric bulk aerosol composition that are split into two different factors by PMF.

F2 is characterized by the presence of a mixture of OA and IA. ~~In (see Fig. S9, we can see that S10m-r). Based on the organic spectrum, the aerosol mixture can be characterized as LO-OOA, comparable to the LO-OOA profile found in other aerosol mass spectrometry studies using CV (Hu et al., 2018; Zheng et al., 2020; Joo et al., 2021). It has similar  $f_{44}/f_{43}$  to LO-OOA profile in F4 in average (see triangle plot in Fig. S6). In terms of diurnal cycle of, the F2 is mass loading does not follow the typical LO-OOA pattern. Normally, LO-OOA would have a higher nighttime concentration and slight decrease during the day (Chen et al., 2022), but we found the diurnal cycle of F2 to be similar to the diurnal pattern of total aerosol mass loading in spring (May). It is less similar in summer (June) and autumn (September) due to scarcity of OA mass, which is mainly found in the size-driven factors; this study (see Fig. S10g,i,k). This pattern finding suggests that F2 is the result of condensation of available semi-volatile chemical constituents over the course of the day, as the continuation of NPF and growth, governed by the availability of both bulk IA and OA composition.~~

Formatted: Font: +Headings (Times New Roman)

While F2 contains both OA and IA, F1 is dominated by OA (see Fig. S10m-r). It represents the continuation of NPF and growth enriched by organic compounds. F1 is composed mainly of OA with organics (82% to 94%) and a trace amount of IA, containing the majority of OA in every month, ammonium (2% to 6%) and sulfate (2% to 12%). A trace of nitrate aerosol (2%) can also be found in F1 in the summer (June). The abundance of m/z 44 fragments and high  $f_{44}/f_{43}$  values (see Fig. S6) indicates that factor F1 represents aged organic aerosol SOA, resembling OAOOA profiles observed at the same site in previous studies (Mensah et al., 2012; Paglione et al., 2014; Schlag et al., 2016) and MO-OOA profiles observed in aerosol mass spectrometry with CV (Hu et al., 2018; Zheng et al., 2020; Joo et al., 2021). F1 exhibits a diurnal pattern consistent with MO-OOA, with concentration rising slightly across the day. It has a relatively stable concentration throughout the day because the factor is driven largely by long-range transport of aerosol (Kodros et al., 2020; Chen et al., 2022), but with slightly increasing concentration from morning to afternoon due to photochemical oxidation. Wind analysis suggests that the bulk SOA in F1 is related to airmasses arriving from the easterly sector that spans from north ( $\sim 0^\circ$ ) to south ( $\sim 180^\circ$ ) (see Fig. S7). To the east, the province of Gelderland is mostly covered by agricultural grass land and forested nature areas that emit VOCs, therefore increasing the amount of OA produced. Easterly wind directions may also contain the accumulated pollutants or VOCs from continental Europe, and therefore may contain a variety of OA from either biogenic or anthropogenic sources. 2016). The factor is related to airmasses arriving from the easterly to southerly sector (see Fig. S10 in Sect. S3 for details). Considering the organic profile, the high mass loading percentage, and the source regions across periods, we attribute F1 to background regional and continental OA.

#### 4. Conclusions

In this work, we have shown that hybrid ACSM-SMPS PMF analysis can be used to determine the bulk chemical constituents composition associated with new particle formation and growth. The analyses of three selected periods enable us to use the seasonality of the factor profiles, representing conditions of spring (sunny and warm) for May, summer (very sunny and hot) for June, and autumn (less sunny and warm) for September, as well as different prevailing winds, to attribute factor sources. Different chemical composition regimes were observed across these seasons, which manifested as differences in the species controlling aerosol growth.

New particle formation episodes appeared when the total aerosol concentration was low, with key contributions from ammonium sulfate, regardless of bulk aerosol composition regime, and oxygenated organic compounds across seasons, despite the high nitrogen emission in the Netherlands. This new particle formation and growth exhibits a diurnal pattern dominated by daytime formation that shifts to nighttime growth as the particle size increases. While sulfate promotes new particle formation, nitrate and semi-volatile organics are more influential in condensational growth. Organics participate in either new particle formation or growth.

Formatted: Font: +Headings (Times New Roman)

Formatted: Font color: Text 1

Formatted: Font color: Text 1

Formatted: Font color: Text 1

695 The abundance of organics, sulfate, and substantial contribution of nitrate and less oxidized organic aerosols to F3, and its  
shift to a nighttime peak in concentration, indicate that ammonium aerosol, as well as the mean radiation and temperature,  
govern the chemical species distribution across the factors. As a result, different modes of new particle formation and growth  
exist. The sulfate-rich regime in spring results in the nucleation mode containing a mixture ammonium sulfate and organics,  
and organic nitrate condensing during the particle growth when the temperature is lower. The organic-rich regime, higher mean  
radiation, and higher mean temperature in summer results in larger contribution of oxidized oxygenated organic vapors in new  
700 particle formation. The ammonium excess condition in autumn promotes nucleation without the presence of organic  
compounds.

A particle growth mode that arises from condensation of semi-volatile organics from the bulk atmospheric composition is  
observed in F5. In particular, the substantial contribution of nitrate in F5 during summer could be seen as the possible  
705 promotion of organic nitrate formation in nitrate excess condition in higher radiation, condensing during the particle growth  
when the temperature is lower. F4 is seen as the continuation of previous growth modes with similar composition but larger  
particle size range. The factor with the largest particle diameter sub-range, F3, has a nitrate-rich composition across the seasons,  
illustrating the ubiquitous importance of nitrate.

710 New particle formation is most pronounced with winds from the southwest-west, or north and east sometimes northeast. These  
directions supply precursors gases, with the westerlies bringing SO<sub>x</sub> from the port of Rotterdam, southwesterlies bringing NH<sub>3</sub>  
from agricultural emissions, and northerlies and easterlies bring organic vapors from the forest and nature areas. There is also  
an indication of SO<sub>x</sub> sources from other urban centers to the north and east. The influence of the wind direction can be clearly  
seen during the summer, where instead of southern and western winds, the prevailing winds were from the north and east and  
715 brought abundant organics, resulting in the rapid growth of large amounts of OA.

In sum, this novel combination of composition and size information into the statistical PMF tool, combined with method of  
PMF, augmented by meteorological and gas-phase auxiliary data, provides a powerful tool to assess the factors that control  
aerosol production in a complex region, heavily influenced by agricultural and industrial activities, alongside biogenic  
720 emissions of VOCs.

**Code availability**

The analysis and graphics are mainly generated using Igor Pro 8. The code utilized in the PMF analysis is part of the PMF  
Evaluation Tool (PET) v3.08 written as Igor procedures, available at [https://cires1.colorado.edu/jimenez-](https://cires1.colorado.edu/jimenez-group/wiki/index.php/PMF-AMS_Analysis_Guide#PMF_Evaluation_Tool_Software)  
group/wiki/index.php/PMF-AMS Analysis Guide#PMF Evaluation Tool Software (Ulbrich et al., 2009). The map,  
725 pollution roses, and particle size distribution time series are generated using Python 3.9 packages. The map is generated using

Formatted: Font color: Auto

Formatted: Font color: Auto

Formatted: Font: +Headings (Times New Roman)



- [mass spectra from Aerodyne aerosol mass spectrometer data, Journal of Aerosol Science, 35, 909–922, https://doi.org/10.1016/j.jaerosci.2004.02.007, 2004.](https://doi.org/10.1016/j.jaerosci.2004.02.007)
- 755 Amaral, S., de Carvalho, J., Costa, M., and Pinheiro, C.: An Overview of Particulate Matter Measurement Instruments, *Atmosphere*, 6, 1327–1345, <https://doi.org/10.3390/atmos6091327>, 2015.
- Andreae, M. O. and Crutzen, P. J.: Atmospheric Aerosols: Biogeochemical Sources and Role in Atmospheric Chemistry, *Science*, 276, 1052–1058, <https://doi.org/10.1126/science.276.5315.1052>, 1997.
- ~~Ansari, A. S. and Pandis, S. N.: Response of Inorganic PM to Precursor Concentrations, Environ. Sci. Technol., 32, 2706–2714, https://doi.org/10.1021/es971130j, 1998.~~
- 760 Asmi, E., Kivekäs, N., Kerminen, V.-M., Komppula, M., Hyvärinen, A.-P., Hatakka, J., Viisanen, Y., and Lihavainen, H.: Secondary new particle formation in Northern Finland Pallas site between the years 2000 and 2010, *Atmos. Chem. Phys.*, 11, 12959–12972, <https://doi.org/10.5194/acp-11-12959-2011>, 2011.
- Ayala, A., Brauer, M., Mauderly, J. L., and Samet, J. M.: Air pollutants and sources associated with health effects, *Air Qual. Atmos. Health*, 5, 151–167, <https://doi.org/10.1007/s11869-011-0155-2>, 2012.
- 765 Barsanti, K. C., Kroll, J. H., and Thornton, J. A.: Formation of Low-Volatility Organic Compounds in the Atmosphere: Recent Advancements and Insights, *J. Phys. Chem. Lett.*, 8, 1503–1511, <https://doi.org/10.1021/acs.jpclett.6b02969>, 2017.
- Berkemeier, T., Ammann, M., Mentel, T. F., Pöschl, U., and Shiraiwa, M.: Organic Nitrate Contribution to New Particle Formation and Growth in Secondary Organic Aerosols from  $\alpha$ -Pinene Ozonolysis, *Environ. Sci. Technol.*, 50, 6334–6342, <https://doi.org/10.1021/acs.est.6b00961>, 2016.
- 770 Bianchi, F., Tröstl, J., Junninen, H., Frege, C., Henne, S., Hoyle, C. R., Molteni, U., Herrmann, E., Adamov, A., Bukowiecki, N., Chen, X., Duplissy, J., Gysel, M., Hutterli, M., Kangasluoma, J., Kontkanen, J., Kürten, A., Manninen, H. E., Münch, S., Peräkylä, O., Petäjä, T., Rondo, L., Williamson, C., Weingartner, E., Curtius, J., Worsnop, D. R., Kulmala, M., Dommen, J., and Baltensperger, U.: New particle formation in the free troposphere: A question of chemistry and timing, *Science*, 352, 1109–1112, <https://doi.org/10.1126/science.aad5456>, 2016.
- 775 Brean, J., Dall'Osto, M., Simó, R., Shi, Z., Beddows, D. C. S., and Harrison, R. M.: Open ocean and coastal new particle formation from sulfuric acid and amines around the Antarctic Peninsula, *Nat. Geosci.*, 14, 383–388, <https://doi.org/10.1038/s41561-021-00751-y>, 2021.
- Carslaw, D. C. and Ropkins, K.: openair — An R package for air quality data analysis, *Environmental Modelling & Software*, 27–28, 52–61, <https://doi.org/10.1016/j.envsoft.2011.09.008>, 2012.
- 780 Castro, A., Alonso-Blanco, E., González-Colino, M., Calvo, A. I., Fernández-Raga, M., and Fraile, R.: Aerosol size distribution in precipitation events in León, Spain, *Atmospheric Research*, 96, 421–435, <https://doi.org/10.1016/j.atmosres.2010.01.014>, 2010.
- CBS: Agriculture; crops, livestock and land use by general farm type, region, CBS, 2022.
- 785 Celles, S., Filipe, Quick, J., Samuël Weber/GwendalD, Kittner, J., Strawberry Beach Sandals, Ogasawara, I., Bachant, P., Maussion, F., Kvalsvik, J., R, M., Raj, S. P., McCann, J., and Sspagnol: python-windrose/windrose: v1.8.1, <https://doi.org/10.5281/ZENODO.7465610>, 2022.

Formatted: Font: +Headings (Times New Roman)

Formatted: Font: +Headings (Times New Roman)

Formatted: Font: +Headings (Times New Roman)

Formatted: Font: +Headings (Times New Roman)

Formatted: Font: +Headings (Times New Roman)

Formatted: Font: +Headings (Times New Roman)

Chen, G., Canonaco, F., Tobler, A., Aas, W., Alastuey, A., Allan, J., Atabakhsh, S., Aurela, M., Baltensperger, U., Bougiatioti, A., De Brito, J. F., Ceburnis, D., Chazeau, B., Chebaicheb, H., Daellenbach, K. R., Ehn, M., El Haddad, I., Eleftheriadis, K., Favez, O., Flentje, H., Font, A., Fossom, K., Freney, E., Gini, M., Green, D. C., Heikkinen, L., Herrmann, H., Kalogridis, A.-C., Keernik, H., Lhotka, R., Lin, C., Lunder, C., Maasikmets, M., Manousakas, M. I., Marchand, N., Marin, C., Marmureanu, L., Mihalopoulos, N., Močnik, G., Nęcki, J., O'Dowd, C., Ovadnevaite, J., Peter, T., Petit, J.-E., Pikridas, M., Matthew Platt, S., Pokorná, P., Poulain, L., Priestman, M., Riffault, V., Rinaldi, M., Róžański, K., Schwarz, J., Sciare, J., Simon, L., Skiba, A., Slowik, J. G., Sosedova, Y., Stavroulas, I., Styszko, K., Teinemaa, E., Timonen, H., Tremper, A., Vasilescu, J., Via, M., Vodička, P., Wiedensohler, A., Zografou, O., Cruz Minguiñón, M., and Prévôt, A. S. H.: European aerosol phenomenology – 8: Harmonised source apportionment of organic aerosol using 22 Year-long ACSM/AMS datasets, *Environment International*, 166, 107325, <https://doi.org/10.1016/j.envint.2022.107325>, 2022.

Dada, L., Paasonen, P., Nieminen, T., Buenrostro Mazon, S., Kontkanen, J., Peräkylä, O., Lehtipalo, K., Hussein, T., Petäjä, T., Kerminen, V.-M., Bäck, J., and Kulmala, M.: Long-term analysis of clear-sky new particle formation events and nonevents in Hyytiälä, *Atmos. Chem. Phys.*, 17, 6227–6241, <https://doi.org/10.5194/acp-17-6227-2017>, 2017.

Dada, L., Chellapermal, R., Buenrostro Mazon, S., Paasonen, P., Lampilahti, J., Manninen, H. E., Junninen, H., Petäjä, T., Kerminen, V.-M., and Kulmala, M.: Refined classification and characterization of atmospheric new particle formation events using air ions, *Atmos. Chem. Phys.*, 18, 17883–17893, <https://doi.org/10.5194/acp-18-17883-2018>, 2018.

Dai, L., Wang, H., Zhou, L., An, J., Tang, L., Lu, C., Yan, W., Liu, R., Kong, S., Chen, M., Lee, S., and Yu, H.: Regional and local new particle formation events observed in the Yangtze River Delta region, China, *J. Geophys. Res.-Atmos.*, 122, 2389–2402, <https://doi.org/10.1002/2016JD026030>, 2017.

Dall’Osto, M., Beddows, D. C. S., Asmi, A., Poulain, L., Hao, L., Freney, E., Allan, J. D., Canagaratna, M., Crippa, M., Bianchi, F., de Leeuw, G., Eriksson, A., Swietlicki, E., Hansson, H. C., Henzing, J. S., Granier, C., Zemankova, K., Laj, P., Onasch, T., Prevot, A., Putaud, J. P., Sellegri, K., Vidal, M., Virtanen, A., Simo, R., Worsnop, D., O’Dowd, C., Kulmala, M., and Harrison, R. M.: Novel insights on new particle formation derived from a pan-european observing system, *Sci Rep*, 8, 1482, <https://doi.org/10.1038/s41598-017-17343-9>, 2018.

Decherety, K. S., Aiken, A. C., Huffman, J. A., Ulbrich, I. M., DeCarlo, P. F., Sueper, D., Worsnop, D. R., Snyder, D. C., Peltier, R. E., Weber, R. J., Grover, B. D., Eatough, D. J., Williams, B. J., Goldstein, A. H., Ziemann, P. J., and Jimenez, J. L.: The 2005 Study of Organic Aerosols at Riverside (SOAR-1): instrumental intercomparisons and fine particle composition, *Atmos. Chem. Phys.*, 11, 12387–12420, <https://doi.org/10.5194/acp-11-12387-2011>, 2011.

Ehn, M., Thornton, J. A., Kleist, E., Sipilä, M., Junninen, H., Pullinen, I., Springer, M., Rubach, F., Tillmann, R., Lee, B., Lopez-Hilfiker, F., Andres, S., Acir, I.-H., Rissanen, M., Jokinen, T., Schobesberger, S., Kangasluoma, J., Kontkanen, J., Nieminen, T., Kurtén, T., Nielsen, L. B., Jørgensen, S., Kjaergaard, H. G., Canagaratna, M., Maso, M. D., Berndt, T., Petäjä, T., Wahner, A., Kerminen, V.-M., Kulmala, M., Worsnop, D. R., Wildt, J., and Mentel, T. F.: A large source of low-volatility secondary organic aerosol, *Nature*, 506, 476–479, <https://doi.org/10.1038/nature13032>, 2014.

Elson, P., De Andrade, E. S., Lucas, G., May, R., Hattersley, R., Campbell, E., Dawson, A., Stephane Raynaud, Scmc72, Little, B., Snow, A. D., Donkers, K., Blay, B., Killick, P., Wilson, N., Peglar, P., Lbdreyer, Andrew, Szymaniak, J., Berchet, A., Bosley, C., Davis, L., Filipe, Krasting, J., Bradbury, M., Kirkham, D., Stephenworsley, Clément, Caria, G., and Herzmann, D.: SciTools/cartopy: v0.21.1, <https://doi.org/10.5281/ZENODO.7430317>, 2022.

Erisman, J. W., Galloway, J., Seitzinger, S., Bleeker, A., and Butterbach-Bahl, K.: Reactive nitrogen in the environment and its effect on climate change, *Current Opinion in Environmental Sustainability*, 3, 281–290, <https://doi.org/10.1016/j.cosust.2011.08.012>, 2011.

Formatted: Font: +Headings (Times New Roman)

Formatted: Font: +Headings (Times New Roman)

Formatted: Font: +Headings (Times New Roman)

Formatted: Font: +Headings (Times New Roman)

Formatted: Font: +Headings (Times New Roman)

Formatted: Font: +Headings (Times New Roman)

Formatted: Font: +Headings (Times New Roman)

Formatted: Font: +Headings (Times New Roman)

Formatted: Font: +Headings (Times New Roman)

Formatted: Font: +Headings (Times New Roman)

Formatted: Font: +Headings (Times New Roman)

Formatted: Font: +Headings (Times New Roman)

Formatted: Font: +Headings (Times New Roman)

Formatted: Font: +Headings (Times New Roman)

Formatted: Font: +Headings (Times New Roman)



830 Fan, J., Rosenfeld, D., Zhang, Y., Giangrande, S. E., Li, Z., Machado, L. A. T., Martin, S. T., Yang, Y., Wang, J., Artaxo, P., Barbosa, H. M. J., Braga, R. C., Comstock, J. M., Feng, Z., Gao, W., Gomes, H. B., Mei, F., Pöhlker, C., Pöhlker, M. L., Pöschl, U., and de Souza, R. A. F.: Substantial convection and precipitation enhancements by ~~ultrafine aerosol~~ ultrafine aerosol particles, *Science*, 359, 411–418, <https://doi.org/10.1126/science.aan8461>, 2018.

~~Farmer, D. K., Matsunaga, A., Docherty, K. S., Surratt, J. D., Seinfeld, J. H., Ziemann, P. J., and Jimenez, J. L.: Response of an aerosol mass spectrometer to organonitrates and organosulfates and implications for atmospheric chemistry, *Proc. Natl. Acad. Sci. U.S.A.*, 107, 6670–6675, <https://doi.org/10.1073/pnas.0912340107>, 2010.~~

835 Fioletov, V. E., McLinden, C. A., Krotkov, N., Li, C., Joiner, J., Theys, N., Carn, S., and Moran, M. D.: A global catalogue of large SO<sub>2</sub> sources and emissions derived from the Ozone Monitoring Instrument, *Atmos. Chem. Phys.*, 16, 11497–11519, <https://doi.org/10.5194/acp-16-11497-2016>, 2016.

Fröhlich, R., Cubison, M. J., Slowik, J. G., Bukowiecki, N., Prévôt, A. S. H., Baltensperger, U., Schneider, J., Kimmel, J. R., Gonin, M., Rohner, U., Worsnop, D. R., and Jayne, J. T.: The ToF-ACSM: a portable aerosol chemical speciation monitor with TOFMS detection, *Atmos. Meas. Tech.*, 6, 3225–3241, <https://doi.org/10.5194/amt-6-3225-2013>, 2013.

840 Gordon, H., Sengupta, K., Rap, A., Duplissy, J., Frege, C., Williamson, C., Heinritzi, M., Simon, M., Yan, C., Almeida, J., Tröstl, J., Nieminen, T., Ortega, I. K., Wagner, R., Dunne, E. M., Adamov, A., Amorim, A., Bernhammer, A.-K., Bianchi, F., Breitenlechner, M., Brilke, S., Chen, X., Craven, J. S., Dias, A., Ehrhart, S., Fischer, L., Flagan, R. C., Franchin, A., Fuchs, C., Guida, R., Hakala, J., Hoyle, C. R., Jokinen, T., Junninen, H., Kangasluoma, J., Kim, J., Kirkby, J., Krapf, M., Kürten, A., Laaksonen, A., Lehtipalo, K., Makhmutov, V., Mathot, S., Molteni, U., Monks, S. A., Onnela, A., Peräkylä, O., Piel, F., Petäjä, T., Praplan, A. P., Pringle, K. J., Richards, N. A. D., Rissanen, M. P., Rondo, L., Sarnela, N., Schobesberger, S., Scott, C. E., Seinfeld, J. H., Sharma, S., Sipilä, M., Steiner, G., Stozhkov, Y., Stratmann, F., Tomé, A., Virtanen, A., Vogel, A. L., Wagner, A. C., Wagner, P. E., Weingartner, E., Wimmer, D., Winkler, P. M., Ye, P., Zhang, X., Hansel, A., Dommen, J., Donahue, N. M., Worsnop, D. R., Baltensperger, U., Kulmala, M., Curtius, J., and Carslaw, K. S.: Reduced anthropogenic aerosol radiative forcing caused by biogenic new particle formation, *Proc. Natl. Acad. Sci. U.S.A.*, 113, 12053–12058, <https://doi.org/10.1073/pnas.1602360113>, 2016.

850 Grantz, D. A., Garner, J. H. B., and Johnson, D. W.: Ecological effects of particulate matter, *Environment International*, 29, 213–239, [https://doi.org/10.1016/S0160-4120\(02\)00181-2](https://doi.org/10.1016/S0160-4120(02)00181-2), 2003.

Hamed, A., Joutsensaari, J., Mikkonen, S., Sogacheva, L., Dal Maso, M., Kulmala, M., Cavalli, F., Fuzzi, S., Facchini, M. C., Decesari, S., Mircea, M., Lehtinen, K. E. J., and Laaksonen, A.: Nucleation and growth of new particles in Po Valley, Italy, *Atmos. Chem. Phys.*, 7, 355–376, <https://doi.org/10.5194/acp-7-355-2007>, 2007.

855 Haywood, J.: Atmospheric Aerosols and Their Role in Climate Change, in: *Climate Change*, Elsevier, 449–463, <https://doi.org/10.1016/B978-0-444-63524-2.00027-0>, 2016.

~~He, L.-Y., Lin, Y., Huang, X., Guo, S., Xue, L., Su, Q., Hu, M., Luan, S., J., and Zhang, Y.-H.: Characterization of high-resolution aerosol mass spectra of primary organic aerosol emissions from Chinese cooking and biomass burning, *Atmos. Chem. Phys.*, 10, 11535–11543, <https://doi.org/10.5194/acp-10-11535-2010>, 2010.~~

860 Heinritzi, M., Dada, L., Simon, M., Stolzenburg, D., Wagner, A. C., Fischer, L., Ahonen, L. R., Amanatidis, S., Baalbaki, R., Baccarini, A., Bauer, P. S., Baumgartner, B., Bianchi, F., Brilke, S., Chen, D., Chiu, R., Dias, A., Dommen, J., Duplissy, J., Finkenzeller, H., Frege, C., Fuchs, C., Garmash, O., Gordon, H., Granzin, M., El Haddad, I., He, X., Helm, J., Hofbauer, V., Hoyle, C. R., Kangasluoma, J., Keber, T., Kim, C., Kürten, A., Lamkaddam, H., Laurila, T. M., Lampilahti, J., Lee, C. P., Lehtipalo, K., Leiminger, M., Mai, H., Makhmutov, V., Manninen, H. E., Marten, R., Mathot, S., Mauldin, R. L., Mentler, B., Molteni, U., Müller, T., Nie, W., Nieminen, T., Onnela, A., Partoll, E., Passananti, M., Petäjä, T., Pfeifer, J., Pospisilova, V., Quéléver, L. L. J., Rissanen, M. P., Rose, C., Schobesberger, S., Scholz, W., Scholze, K., Sipilä, M., Steiner, G., Stozhkov,

Formatted: Font: +Headings (Times New Roman)

Formatted: Font: +Headings (Times New Roman)

Formatted: Font: +Headings (Times New Roman)

Formatted: Font: +Headings (Times New Roman)

Formatted: Font: +Headings (Times New Roman)

Formatted: Font: +Headings (Times New Roman)

Formatted: Font: +Headings (Times New Roman)

Formatted: Font: +Headings (Times New Roman)



Jayne, J. T. and Worsnop, D. R.: Particle Capture Device, 2016.

Jimenez, J. L., Canagaratna, M. R., Donahue, N. M., Prevot, A. S. H., Zhang, Q., Kroll, J. H., DeCarlo, P. F., Allan, J. D., Coe, H., Ng, N. L., Aiken, A. C., Docherty, K. S., Ulbrich, I. M., Grieshop, A. P., Robinson, A. L., Duplissy, J., Smith, J. D., Wilson, K. R., Lanz, V. A., Hueglin, C., Sun, Y. L., Tian, J., Laaksonen, A., Raatikainen, T., Rautiainen, J., Vaattovaara, P., Ehn, M., Kulmala, M., Tomlinson, J. M., Collins, D. R., Cubison, M. J., E., Dunlea, J., Huffman, J. A., Onasch, T. B., Alfarra, M. R., Williams, P. I., Bower, K., Kondo, Y., Schneider, J., Drewnick, F., Borrmann, S., Weimer, S., Demerjian, K., Salcedo, D., Cottrell, L., Griffin, R., Takami, A., Miyoshi, T., Hatakeyama, S., Shimono, A., Sun, J. Y., Zhang, Y. M., Dzepina, K., Kimmel, J. R., Sueper, D., Jayne, J. T., Herndon, S. C., Trimborn, A. M., Williams, L. R., Wood, E. C., Middlebrook, A. M., Kolb, C. E., Baltensperger, U., and Worsnop, D. R.: Evolution of Organic Aerosols in the Atmosphere, *Science*, 326, 1525–1529, <https://doi.org/10.1126/science.1180353>, 2009.

Jokinen, T., Lehtipalo, K., Thakur, R. C., Ylivinkka, I., Neitola, K., Sarnela, N., Laitinen, T., Kulmala, M., Petäjä, T., and Sipilä, M.: Measurement report: Long-term measurements of aerosol precursor concentrations in the Finnish subarctic boreal forest, *Atmos. Chem. Phys.*, 22, 2237–2254, <https://doi.org/10.5194/acp-22-2237-2022>, 2022.

Kalkavouras, Joo, T., Chen, Y., Xu, W., Croteau, P., Canagaratna, M. R., Gao, D., Guo, H., Saavedra, G., Kim, S. S., Sun, Y., Weber, R., Jayne, J., and Ng, N. L.: Evaluation of a New Aerosol Chemical Speciation Monitor (ACSM) System at an Urban Site in Atlanta, GA: The Use of Capture Vaporizer and PM<sub>2.5</sub> Inlet, *ACS Earth Space Chem.*, 5, 2565–2576, <https://doi.org/10.1021/acsearthspacechem.1c00173>, 2021.

P. Bougiatioti, A., Hussein, T., Kalivitis, N., Stavroulas, I., Michalopoulos, P., and Mihalopoulos, N.: Regional New Particle Formation over the Eastern Mediterranean and Middle East, *Atmosphere*, 12, 13, <https://doi.org/10.3390/atmos12010013>, 2020.

Kammer, J., Perraudin, E., Flaud, P. M., Lamaud, E., Bonnefond, J. M., and Villenave, E.: Observation of nighttime new particle formation over the French Landes forest, *Science of The Total Environment*, 621, 1084–1092, <https://doi.org/10.1016/j.scitotenv.2017.10.118>, 2018.

Kerminen, V.-M., Chen, X., Vakkari, V., Petäjä, T., Kulmala, M., and Bianchi, F.: Atmospheric new particle formation and growth: review of field observations, *Environ. Res. Lett.*, 13, 103003, <https://doi.org/10.1088/1748-9326/aadf3c>, 2018.

Kodros, J. K., Papanastasiou, D. K., Paglione, M., Masiol, M., Squizzato, S., Florou, K., Skyllakou, K., Kaltsonoudis, C., Nenes, A., and Pandis, S. N.: Rapid dark aging of biomass burning as an overlooked source of oxidized organic aerosol, *Proc. Natl. Acad. Sci. U.S.A.*, 117, 33028–33033, <https://doi.org/10.1073/pnas.2010365117>, 2020.

Kolesar, K. R., Cellini, J., Peterson, P. K., Jefferson, A., Tuch, T., Birmili, W., Wiedensohler, A., and Pratt, K. A.: Effect of Prudhoe Bay emissions on atmospheric aerosol growth events observed in Utqiagvik (Barrow), Alaska, *Atmospheric Environment*, 152, 146–155, <https://doi.org/10.1016/j.atmosenv.2016.12.019>, 2017.

Kulmala, M., Petäjä, T., Nieminen, T., Sipilä, M., Manninen, H. E., Lehtipalo, K., Dal-Maso, M., Aalto, P. P., Junninen, H., Paasonen, P., Riiipinen, I., Lehtinen, K. E. J., Laaksonen, A., and Kerminen, V. M.: Measurement of the nucleation of atmospheric aerosol particles, *Nat Protoc.*, 7, 1651–1667, <https://doi.org/10.1038/nprot.2012.091>, 2012.

Kulmala, M., Kontkanen, J., Junninen, H., Lehtipalo, K., Manninen, H. E., Nieminen, T., Petäjä, T., Sipilä, M., Schobesberger, S., Rantala, P., Franchin, A., Jokinen, T., Järvinen, E., Äijälä, M., Kangasluoma, J., Hakala, J., Aalto, P. P., Paasonen, P., Mikkilä, J., Vanhanen, J., Aalto, J., Hakola, H., Makkonen, U., Ruuskanen, T., Mauldin, R. L., Duplissy, J., Vehkamäki, H., Bäck, J., Kortelainen, A., Riiipinen, I., Kurtén, T., Johnston, M. V., Smith, J. N., Ehn, M., Mentel, T. F., Lehtinen, K. E. J., Laaksonen, A., Kerminen, V.-M., and Worsnop, D. R.: Direct Observations of Atmospheric Aerosol Nucleation, *Science*, 339, 943–946, <https://doi.org/10.1126/science.1227385>, 2013.

Formatted: Font: +Headings (Times New Roman)

Formatted: Font: +Headings (Times New Roman)

Formatted: Font: +Headings (Times New Roman)

Formatted: Font: +Headings (Times New Roman)

Formatted: Font: +Headings (Times New Roman)

Formatted: Font: +Headings (Times New Roman)

Formatted: Font: +Headings (Times New Roman)

- 950 Kulmala, M., Junninen, H., Dada, L., Salma, I., Weidinger, T., Thén, W., Vörösmarty, M., Komsaare, K., Stolzenburg, D., Cai, R., Yan, C., Li, X., Deng, C., Jiang, J., Petäjä, T., Nieminen, T., and Kerminen, V.-M.: Quiet New Particle Formation in the Atmosphere, *Front. Environ. Sci.*, 10, 912385, <https://doi.org/10.3389/fenvs.2022.912385>, 2022.
- Kürten, A.: New particle formation from sulfuric acid and ammonia: nucleation and growth model based on thermodynamics derived from CLOUD measurements for a wide range of conditions, *Atmos. Chem. Phys.*, 19, 5033–5050, <https://doi.org/10.5194/acp-19-5033-2019>, 2019.
- 955 Lanz, V. A., Alfarra, M. R., Baltensperger, U., Buchmann, B., Hueglin, C., and Prévôt, A. S. H.: Source apportionment of submicron organic aerosols at an urban site by factor analytical modelling of aerosol mass spectra, *Atmos. Chem. Phys.*, 7, 1503–1522, <https://doi.org/10.5194/acp-7-1503-2007>, 2007.
- Ledoux, F., Roche, C., Cazier, F., Beaugard, C., and Courcot, D.: Influence of ship emissions on NO<sub>x</sub>, SO<sub>2</sub>, O<sub>3</sub> and PM concentrations in a North-Sea harbor in France, *Journal of Environmental Sciences*, 71, 56–66, <https://doi.org/10.1016/j.jes.2018.03.030>, 2018.
- 960 Lee, S., Gordon, H., Yu, H., Lehtipalo, K., Haley, R., Li, Y., and Zhang, R.: New Particle Formation in the Atmosphere: From Molecular Clusters to Global Climate, *J. Geophys. Res. Atmos.*, 124, 7098–7146, <https://doi.org/10.1029/2018JD029356>, 2019.
- 965 Lehtipalo, K., Yan, C., Dada, L., Bianchi, F., Xiao, M., Wagner, R., Stolzenburg, D., Ahonen, L. R., Amorim, A., Baccarini, A., Bauer, P. S., Baumgartner, B., Bergen, A., Bernhammer, A.-K., Breitenlechner, M., Brilke, S., Buchholz, A., Mazon, S. B., Chen, D., Chen, X., Dias, A., Dommen, J., Draper, D. C., Duplissy, J., Ehn, M., Finkenzeller, H., Fischer, L., Frege, C., Fuchs, C., Garmash, O., Gordon, H., Hakala, J., He, X., Heikkinen, L., Heinritzi, M., Helm, J. C., Hofbauer, V., Hoyle, C. R., Jokinen, T., Kangasluoma, J., Kerminen, V.-M., Kim, C., Kirkby, J., Kontkanen, J., Kürten, A., Lawler, M. J., Mai, H., Mathot, S., Mauldin, R. L., Molteni, U., Nichman, L., Nie, W., Nieminen, T., Ojdanic, A., Onnela, A., Passananti, M., Petäjä, T., Piel, F., Pospisilova, V., Quéléver, L. L. J., Rissanen, M. P., Rose, C., Sarnela, N., Schallhart, S., Schuchmann, S., Sengupta, K., Simon, M., Sipilä, M., Tauber, C., Tomé, A., Tröstl, J., Väisänen, O., Vogel, A. L., Volkamer, R., Wagner, A. C., Wang, M., Weitz, L., Wimmer, D., Ye, P., Ylisirniö, A., Zha, Q., Carslaw, K. S., Curtius, J., Donahue, N. M., Flagan, R. C., Hansel, A., Riipinen, I., Virtanen, A., Winkler, P. M., Baltensperger, U., Kulmala, M., and Worsnop, D. R.: Multicomponent new particle formation from sulfuric acid, ammonia, and biogenic vapors, *Sci. Adv.*, 4, eaau5363, <https://doi.org/10.1126/sciadv.aau5363>, 2018.
- 975 Liu, L., Li, H., Zhang, H., Zhong, J., Bai, Y., Ge, M., Li, Z., Chen, Y., and Zhang, X.: The role of nitric acid in atmospheric new particle formation, *Phys. Chem. Chem. Phys.*, 20, 17406–17414, <https://doi.org/10.1039/C8CP02719F>, 2018.
- Lohmann, U. and Feichter, J.: Global indirect aerosol effects: a review, *Atmos. Chem. Phys.*, 5, 715–737, <https://doi.org/10.5194/acp-5-715-2005>, 2005.
- 980 Mahowald, N., Ward, D. S., Kloster, S., Flanner, M. G., Heald, C. L., Heavens, N. G., Hess, P. G., Lamarque, J.-F., and Chuang, P. Y.: Aerosol Impacts on Climate and Biogeochemistry, *Annu. Rev. Environ. Resour.*, 36, 45–74, <https://doi.org/10.1146/annurev-environ-042009-094507>, 2011.
- Marrero-Ortiz, W., Hu, M., Du, Z., Ji, Y., Wang, Y., Guo, S., Lin, Y., Gomez-Hernandez, M., Peng, J., Li, Y., Secret, J., Zamora, M. L., Wang, Y., An, T., and Zhang, R.: Formation and Optical Properties of Brown Carbon from Small  $\alpha$ -Dicarbonyls and Amines, *Environ. Sci. Technol.*, 53, 117–126, <https://doi.org/10.1021/acs.est.8b03995>, 2019.
- 985 Maso, M. D., Kulmala, M., Riipinen, I., Wagner, R., Hussein, T., Aalto, P. P., and Lehtinen, K. E. J.: Formation and growth of fresh atmospheric aerosols: eight years of aerosol size distribution data from SMEAR II, Hyytiälä, Finland, *Boreal Environment Research*, 10, 323–336, 2005.

**Formatted:** Font: +Headings (Times New Roman)

**Formatted:** Font: +Headings (Times New Roman)

**Formatted:** Font: +Headings (Times New Roman)

**Formatted:** Font: +Headings (Times New Roman)

**Formatted:** Font: +Headings (Times New Roman)

990 Mensah, A. A., Holzinger, R., Otjes, R., Trimborn, A., Mentel, Th. F., ten Brink, H., Henzing, B., and Kiendler-Scharr, A.: Aerosol chemical composition at Cabauw, The Netherlands as observed in two intensive periods in May 2008 and March 2009, *Atmos. Chem. Phys.*, 12, 4723–4742, <https://doi.org/10.5194/acp-12-4723-2012>, 2012.

~~Middlebrook, A. M., Bahreini, R., Jimenez, J. L., and Canagaratna, M. R.: Evaluation of Composition-Dependent Collection Efficiencies for the Aerodyne Aerosol Mass Spectrometer using Field Data, *Aerosol Science and Technology*, 46, 258–271, <https://doi.org/10.1080/02786826.2011.620041>, 2012.~~

995 Modini, R. L., Ristovski, Z. D., Johnson, G. R., He, C., Surawski, N., Morawska, L., Suni, T., and Kulmala, M.: New particle formation and growth at a remote, sub-tropical coastal location, *Atmos. Chem. Phys.*, 9, 7607–7621, <https://doi.org/10.5194/acp-9-7607-2009>, 2009.

~~Mohr, C., Huffman, J. A., Cubison, M. J., Aiken, A. C., Docherty, K. S., Kimmel, J. R., Ulbrich, I. M., Hannigan, M., and Jimenez, J. L.: Characterization of Primary Organic Aerosol Emissions from Meat Cooking, Trash Burning, and Motor Vehicles with High-Resolution Aerosol Mass Spectrometry and Comparison with Ambient and Chamber Observations, *Environ. Sci. Technol.*, 43, 2443–2449, <https://doi.org/10.1021/es8011518>, 2009.~~

~~Mohr, C., DeCarlo, P. F., Hering, M. F., Chirico, R., Slowik, J. G., Richter, R., Reche, C., Alastuey, A., Querol, X., Seco, R., Peñuelas, J., Jiménez, J. L., Crippa, M., Zimmermann, R., Baltensperger, U., and Prévôt, A. S. H.: Identification and quantification of organic aerosol from cooking and other sources in Barcelona using aerosol mass spectrometer data, *Atmos. Chem. Phys.*, 12, 1649–1665, <https://doi.org/10.5194/acp-12-1649-2012>, 2012.~~

1000 ~~Mohr, C., Thornton, J. A., Heitto, A., Lopez-Hilfiker, F. D., Lutz, A., Riipinen, J., Hong, J., Donahue, N. M., Hallquist, M., Petäjä, T., Kulmala, M., and Yli-Juuti, T.: Molecular identification of organic vapors driving atmospheric nanoparticle growth, *Nat Commun*, 10, 4442, <https://doi.org/10.1038/s41467-019-12473-2>, 2019.~~

1005 ~~Mooibroek, D., Schaap, M., Weijers, E. P., and Hoogerbrugge, R.: Source apportionment and spatial variability of PM<sub>2.5</sub> using measurements at five sites in the Netherlands, *Atmospheric Environment*, 45, 4180–4191, <https://doi.org/10.1016/j.atmosenv.2011.05.017>, 2011.~~

1010 Mordas, G., Plauškaitė, K., Prokopčič, N., Dudoitis, V., Bozzetti, C., and Ulevicius, V.: Observation of new particle formation on Curonian Spit located between continental Europe and Scandinavia, *Journal of Aerosol Science*, 97, 38–55, <https://doi.org/10.1016/j.jaerosci.2016.03.002>, 2016.

1015 Németh, Z. and Salma, I.: Spatial extension of nucleating air masses in the Carpathian Basin, *Atmos. Chem. Phys.*, 14, 8841–8848, <https://doi.org/10.5194/acp-14-8841-2014>, 2014.

Ng, N. L., Canagaratna, M. R., Zhang, Q., Jimenez, J. L., Tian, J., Ulbrich, I. M., Kroll, J. H., Docherty, K. S., Chhabra, P. S., Bahreini, R., Murphy, S. M., Seinfeld, J. H., Hildebrandt, L., Donahue, N. M., DeCarlo, P. F., Lanz, V. A., Prévôt, A. S. H., Dinar, E., Rudich, Y., and Worsnop, D. R.: Organic aerosol components observed in Northern Hemispheric datasets from Aerosol Mass Spectrometry, *Atmos. Chem. Phys.*, 10, 4625–4641, <https://doi.org/10.5194/acp-10-4625-2010>, 2010.

1020 Ng, N. L., Herndon, S. C., Trimborn, A., Canagaratna, M. R., Croteau, P. L., Onasch, T. B., Sueper, D., Worsnop, D. R., Zhang, Q., Sun, Y. L., and Jayne, J. T.: An Aerosol Chemical Speciation Monitor (ACSM) for Routine Monitoring of the Composition and Mass Concentrations of Ambient Aerosol, *Aerosol Science and Technology*, 45, 780–794, <https://doi.org/10.1080/02786826.2011.560211>, 2011.

1025 Nieminen, T., Asmi, A., Maso, M. D., Aalto, P. P., Keronen, P., Petäjä, T., Kulmala, M., and Kerminen, V.-M.: Trends in atmospheric new-particle formation: 16 years of observations in a boreal-forest environment, *Boreal Environment Research*, 19 (suppl. B), 191–214, 2014.

Formatted: Font: +Headings (Times New Roman)

Formatted: Font: +Headings (Times New Roman)

Formatted: Font: +Headings (Times New Roman)

Formatted: Font: +Headings (Times New Roman)

Formatted: Font: +Headings (Times New Roman)

Formatted: Font: +Headings (Times New Roman)

Formatted: Font: +Headings (Times New Roman)

Formatted: Font: +Headings (Times New Roman)

Formatted: Font: +Headings (Times New Roman)

Formatted: Font: +Headings (Times New Roman)

Formatted: Font: +Headings (Times New Roman)

Formatted: Font: +Headings (Times New Roman), Subsc

Formatted: Font: +Headings (Times New Roman)

1030

Olin, M., Okuljar, M., Rissanen, M. P., Kalliokoski, J., Shen, J., Dada, L., Lampimäki, M., Wu, Y., Lohila, A., Duplissy, J., Sipilä, M., Petäjä, T., Kulmala, M., and Dal Maso, M.: Measurement report: Atmospheric new particle formation in a coastal agricultural site explained with binPMF analysis of nitrate CI-API-TOF spectra, <https://doi.org/10.5194/acp-2022-261>, 22 April 2022.

1035

Paatero, P.: The Multilinear Engine—A Table-Driven, Least Squares Program for Solving Multilinear Problems, Including the *n*-Way Parallel Factor Analysis Model, *Journal of Computational and Graphical Statistics*, 8, 854–888, <https://doi.org/10.1080/10618600.1999.10474853>, 1999.

Paatero, P. and Tapper, U.: Positive matrix factorization: A non-negative factor model with optimal utilization of error estimates of data values, *Environmetrics*, 5, 111–126, <https://doi.org/10.1002/env.3170050203>, 1994.

~~Pachon, J. E., Weber, R. J., Zhang, X., Mulholland, J. A., and Russell, A. G.: Revising the use of potassium (K) in the source apportionment of PM<sub>2.5</sub>, *Atmospheric Pollution Research*, 4, 14–21, <https://doi.org/10.5094/APR.2013.002>, 2013.~~

1040

Paglion, M., Kiendler-Scharr, A., Mensah, A. A., Finessi, E., Giulianelli, L., Sandrini, S., Facchini, M. C., Fuzzi, S., Schlag, P., Piazzalunga, A., Tagliavini, E., Henzing, J. S., and Decesari, S.: Identification of humic-like substances (HULIS) in oxygenated organic aerosols using NMR and AMS factor analyses and liquid chromatographic techniques, *Atmos. Chem. Phys.*, 14, 25–45, <https://doi.org/10.5194/acp-14-25-2014>, 2014.

Peltola, M., Rose, C., Trueblood, J. V., Gray, S., Harvey, M., and Sellegri, K.: New particle formation in coastal New Zealand with a focus on open-ocean air masses, *Atmos. Chem. Phys.*, 22, 6231–6254, <https://doi.org/10.5194/acp-22-6231-2022>, 2022.

1045

Peng, Y., Liu, X., Dai, J., Wang, Z., Dong, Z., Dong, Y., Chen, C., Li, X., Zhao, N., and Fan, C.: Aerosol size distribution and new particle formation events in the suburb of Xi'an, northwest China, *Atmospheric Environment*, 153, 194–205, <https://doi.org/10.1016/j.atmosenv.2017.01.022>, 2017.

1050

~~Pio, C-Pfeifer, S., Birmili, W., Schladitz, A., Legrand, M., Alves, C. A., OliveiraMüller, T., Afonso, J., Caseiro, A., Puxbaum, H., Sanchez-OchoaNowak, A., and Gelencsér, A.: Chemical compositionWiedensohler, A.: A fast and easy-to-implement inversion algorithm for mobility particle size spectrometers considering particle number size distribution information outside of atmospheric aerosols during the 2003 summer intense forest fire period, *Atmospheric Environment*, 42, 7530–7543detection range, *Atmos. Meas. Tech.*, 7, 95–105, <https://doi.org/10.4016/j.atmosenv.2008.05.032>, 20085194/amt-7-95-2014, 2014.~~

1055

Pope, C. A., Coleman, N., Pond, Z. A., and Burnett, R. T.: Fine particulate air pollution and human mortality: 25+ years of cohort studies, *Environmental Research*, 183, 108924, <https://doi.org/10.1016/j.envres.2019.108924>, 2020.

Pospisilova, V., Lopez-Hilfiker, F. D., Bell, D. M., El Haddad, I., Mohr, C., Huang, W., Heikkinen, L., Xiao, M., Dommen, J., Prevot, A. S. H., Baltensperger, U., and Slowik, J. G.: On the fate of oxygenated organic molecules in atmospheric aerosol particles, *Sci. Adv.*, 6, eaax8922, <https://doi.org/10.1126/sciadv.aax8922>, 2020.

Pushpawela, B., Jayaratne, R., and Morawska, L.: The influence of wind speed on new particle formation events in an urban environment, *Atmospheric Research*, 215, 37–41, <https://doi.org/10.1016/j.atmosres.2018.08.023>, 2019.

1060

Qi, X. M., Ding, A. J., Nie, W., Petäjä, T., Kerminen, V.-M., Herrmann, E., Xie, Y. N., Zheng, L. F., Manninen, H., Aalto, P., Sun, J. N., Xu, Z. N., Chi, X. G., Huang, X., Boy, M., Virkkula, A., Yang, X.-Q., Fu, C. B., and Kulmala, M.: Aerosol size distribution and new particle formation in the western Yangtze River Delta of China: 2 years of measurements at the SORPES station, *Atmos. Chem. Phys.*, 15, 12445–12464, <https://doi.org/10.5194/acp-15-12445-2015>, 2015.

Riccobono, F., Schobesberger, S., Scott, C. E., Dommen, J., Ortega, I. K., Rondo, L., Almeida, J., Amorim, A., Bianchi, F., Breitenlechner, M., David, A., Downard, A., Dunne, E. M., Duplissy, J., Ehrhart, S., Flagan, R. C., Franchin, A., Hansel, A.,

Formatted: Font: +Headings (Times New Roman)

Formatted: Font: +Headings (Times New Roman)

Formatted: Font: +Headings (Times New Roman)

Formatted: Font: +Headings (Times New Roman)

Formatted: Font: +Headings (Times New Roman)

Formatted: Font: +Headings (Times New Roman)

Formatted: Font: +Headings (Times New Roman)

Formatted: Font: +Headings (Times New Roman)



1065 Junninen, H., Kajos, M., Keskinen, H., Kupc, A., Kürten, A., Kvashin, A. N., Laaksonen, A., Lehtipalo, K., Makhmutov, V.,  
Mathot, S., Nieminen, T., Onnela, A., Petäjä, T., Praplan, A. P., Santos, F. D., Schallhart, S., Seinfeld, J. H., Sipilä, M.,  
Spracklen, D. V., Stozhkov, Y., Stratmann, F., Tomé, A., Tsagkogeorgas, G., Vaattovaara, P., Viisanen, Y., Vrtala, A.,  
Wagner, P. E., Weingartner, E., Wex, H., Wimmer, D., Carslaw, K. S., Curtius, J., Donahue, N. M., Kirkby, J., Kulmala, M.,  
1070 Worsnop, D. R., and Baltensperger, U.: Oxidation Products of Biogenic Emissions Contribute to Nucleation of Atmospheric  
Particles, *Science*, 344, 717–721, <https://doi.org/10.1126/science.1243527>, 2014.

Riipinen, J., Rose, C., Zha, Q., Dada, Y., Juuti, L., Yan, C., Lehtipalo, K., Junninen, H., Mazon, S. B., Jokinen, T., Sarnela, N.,  
Sipilä, M., Pierce, J. R., Petäjä, T., Kerminen, V., Worsnop, D. R., M., Bianchi, F., and Kulmala, M.: Observations, and  
Donahue, N. M.: The contribution of biogenic ion-induced cluster formation in the atmosphere, *Sci. Adv.*, 4, eaar5218, <https://doi.org/10.1126/sciadv.aar5218>, 2018.

1075 2012.

Salimi, F., Crilley, L. R., Stevanovic, S., Ristovski, Z., Mazaheri, M., He, C., Johnson, G., Ayoko, G., and Morawska, L.:  
Insights into the growth of newly formed particles in a subtropical urban environment, *Atmos. Chem. Phys.*, 15, 13475–13485,  
<https://doi.org/10.5194/acp-15-13475-2015>, 2015.

Schlag, P., Kiendler-Scharr, A., Blom, M. J., Canonaco, F., Henzing, J. S., Moerman, M., Prévôt, A. S. H., and Holzinger, R.:  
1080 Aerosol source apportionment from 1-year measurements at the CESAR tower in Cabauw, the Netherlands, *Atmos. Chem.*  
*Phys.*, 16, 8831–8847, <https://doi.org/10.5194/acp-16-8831-2016>, 2016.

Schneider, J., Weimer, S., Drewnick, F., Bormann, S., Helas, G., Gwaze, P., Schmid, O., Andreae, M. O., and Kirchner, U.:  
Mass spectrometric analysis and aerodynamic properties of various types of combustion-related aerosol particles, *International*  
*Journal of Mass Spectrometry*, 258, 37–49, <https://doi.org/10.1016/j.ijms.2006.07.008>, 2006.

1085 Schobesberger, S., Junninen, H., Bianchi, F., Lönn, G., Ehn, M., Lehtipalo, K., Dommen, J., Ehrhart, S., Ortega, I. K., Franchin,  
A., Nieminen, T., Riccobono, F., Hutterli, M., Duplissy, J., Almeida, J., Amorim, A., Breitenlechner, M., Downard, A. J.,  
Dunne, E. M., Flagan, R. C., Kajos, M., Keskinen, H., Kirkby, J., Kupc, A., Kürten, A., Kurtén, T., Laaksonen, A., Mathot,  
S., Onnela, A., Praplan, A. P., Rondo, L., Santos, F. D., Schallhart, S., Schnitzhofer, R., Sipilä, M., Tomé, A., Tsagkogeorgas,  
G., Vehkamäki, H., Wimmer, D., Baltensperger, U., Carslaw, K. S., Curtius, J., Hansel, A., Petäjä, T., Kulmala, M., Donahue,  
1090 N. M., and Worsnop, D. R.: Molecular understanding of atmospheric particle formation from sulfuric acid and large oxidized  
organic molecules, *Proc. Natl. Acad. Sci. U.S.A.*, 110, 17223–17228, <https://doi.org/10.1073/pnas.1306973110>, 2013.

Seinfeld, J. H. and Pandis, S. N.: Atmospheric chemistry and physics: from air pollution to climate change, 3rd edition., John  
Wiley & Sons, Hoboken, New Jersey, 1152 pp., 2016.

Sellegri, K., Rose, C., Marinoni, A., Lupi, A., Wiedensohler, A., Andrade, M., Bonasoni, P., and Laj, P.: New Particle  
Formation: A Review of Ground-Based Observations at Mountain Research Stations, *Atmosphere*, 10, 493,  
1095 <https://doi.org/10.3390/atmos10090493>, 2019.

Spracklen, D. V., Carslaw, K. S., Merikanto, J., Mann, G. W., Reddington, C. L., Pickering, S., Ogren, J. A., Andrews, E.,  
Baltensperger, U., Weingartner, E., Boy, M., Kulmala, M., Laakso, L., Lihavainen, H., Kivekäs, N., Komppula, M.,  
Mihalopoulos, N., Kouvarakis, G., Jennings, S. G., O'Dowd, C., Birmili, W., Wiedensohler, A., Weller, R., Gras, J., Laj, P.,  
1100 Sellegri, K., Bonn, B., Krejci, R., Laaksonen, A., Hamed, A., Minikin, A., Harrison, R. M., Talbot, R., and Sun, J.: Explaining  
global surface aerosol number concentrations in terms of primary emissions and particle formation, *Atmos. Chem. Phys.*, 10,  
4775–4793, <https://doi.org/10.5194/acp-10-4775-2010>, 2010.

Stull, R. B. (Ed.): An Introduction to Boundary Layer Meteorology, Springer Netherlands, Dordrecht,  
<https://doi.org/10.1007/978-94-009-3027-8>, 1988.

Formatted: Font: +Headings (Times New Roman)

Formatted: Font: +Headings (Times New Roman)

Formatted: Font: +Headings (Times New Roman)

Formatted: Font: +Headings (Times New Roman)

Formatted: Font: +Headings (Times New Roman)

Formatted: Font: +Headings (Times New Roman)

Formatted: Font: +Headings (Times New Roman)

Formatted: Font: +Headings (Times New Roman)

Formatted: Font: +Headings (Times New Roman)

Formatted: Font: +Headings (Times New Roman)

Formatted: Font: +Headings (Times New Roman)

Formatted: Font: +Headings (Times New Roman)

1105 [Sun, Y., Du, W., Fu, P., Wang, Q., Li, J., Ge, X., Zhang, Q., Zhu, C., Ren, L., Xu, W., Zhao, J., Han, T., Worsnop, D. R., and Wang, Z.: Primary and secondary aerosols in Beijing in winter: sources, variations and processes, \*Atmos. Chem. Phys.\*, 2016.](#)

[van der Swaluw, E., Asman, W. A. H., van Jaarsveld, H., and Hoogerbrugge, R.: Wet deposition of ammonium, nitrate and sulfate in the Netherlands over the period 1992–2008, \*Atmospheric Environment\*, 45, 3819–3826, <https://doi.org/10.1016/j.atmosenv.2011.04.017>, 2011.](#)

1110 [Tröstl, J., Chuang, W. K., Gordon, H., Heinritzi, M., Yan, C., Molteni, U., Ahlm, L., Frege, C., Bianchi, F., Wagner, R., Simon, M., Lehtipalo, K., Williamson, C., Craven, J. S., Duplissy, J., Adamov, A., Almeida, J., Bernhammer, A.-K., Breitenlechner, M., Brilke, S., Dias, A., Ehrhart, S., Flagan, R. C., Franchin, A., Fuchs, C., Guida, R., Gysel, M., Hansel, A., Hoyle, C. R., Jokinen, T., Junninen, H., Kangasluoma, J., Keskinen, H., Kim, J., Krapf, M., Kürten, A., Laaksonen, A., Lawler, M., Leiminger, M., Mathot, S., Möhler, O., Nieminen, T., Onnela, A., Petäjä, T., Piel, F. M., Miettinen, P., Rissanen, M. P., Rondo, L., Sarnela, N., Schobesberger, S., Sengupta, K., Sipilä, M., Smith, J. N., Steiner, G., Tomé, A., Virtanen, A., Wagner, A. C., Weingartner, E., Wimmer, D., Winkler, P. M., Ye, P., Carslaw, K. S., Curtius, J., Dommen, J., Kirkby, J., Kulmala, M., Riipinen, I., Worsnop, D. R., Donahue, N. M., and Baltensperger, U.: The role of low-volatility organic compounds in initial particle growth in the atmosphere, \*Nature\*, 533, 527–531, <https://doi.org/10.1038/nature18271>, 2016.](#)

1120 [Tsai, J. H., Tsai, S. M., Wang, W. C., and Chiang, H. L.: Water-soluble ionic species of coarse and fine particulate matter and gas-precursor characteristics at urban and rural sites of central Taiwan, \*Environ Sci Pollut Res\*, 23, 16722–16737, <https://doi.org/10.1007/s11356-016-6834-7>, 2016.](#)

[Ulbrich, I. M., Canagaratna, M. R., Zhang, Q., Worsnop, D. R., and Jimenez, J. L.: Interpretation of organic components from Positive Matrix Factorization of aerosol mass spectrometric data, \*Atmos. Chem. Phys.\*, 9, 2891–2918, <https://doi.org/10.5194/acp-9-2891-2009>, 2009.](#)

1125 [Urban, R. C., Lima-Souza, M., Caetano-Silva, L., Queiroz, M. E. C., Nogueira, R. F. P., Allen, A. G., Cardoso, A. A., Held, G., and Campos, M. L. A. M.: Use of levoglucosan, potassium, and water-soluble organic carbon to characterize the origins of biomass-burning aerosols, \*Atmospheric Environment\*, 61, 562–569, <https://doi.org/10.1016/j.atmosenv.2012.07.082>, 2012.](#)

[Vehkamäki, H. and Riipinen, I.: Thermodynamics and kinetics of atmospheric aerosol particle formation and growth, \*Chem. Soc. Rev.\*, 41, 5160, <https://doi.org/10.1039/c2cs00002d>, 2012.](#)

1130 [Wagner, R., Yan, C., Lehtipalo, K., Duplissy, J., Nieminen, T., Kangasluoma, J., Ahonen, L. R., Dada, L., Kontkanen, J., Manninen, H. E., Dias, A., Amorim, A., Bauer, P. S., Bergen, A., Bernhammer, A.-K., Bianchi, F., Brilke, S., Mazon, S. B., Chen, X., Draper, D. C., Fischer, L., Frege, C., Fuchs, C., Garmash, O., Gordon, H., Hakala, J., Heikkinen, L., Heinritzi, M., Hofbauer, V., Hoyle, C. R., Kirkby, J., Kürten, A., Kvashnin, A. N., Laurila, T., Lawler, M. J., Mai, H., Makhmutov, V., Mauldin III, R. L., Molteni, U., Nichman, L., Nie, W., Ojdanic, A., Onnela, A., Piel, F., Quéléver, L. L. J., Rissanen, M. P., Sarnela, N., Schallhart, S., Sengupta, K., Simon, M., Stolzenburg, D., Stozhkov, Y., Tröstl, J., Viisanen, Y., Vogel, A. L., Wagner, A. C., Xiao, M., Ye, P., Baltensperger, U., Curtius, J., Donahue, N. M., Flagan, R. C., Gallagher, M., Hansel, A., Smith, J. N., Tomé, A., Winkler, P. M., Worsnop, D., Ehn, M., Sipilä, M., Kerminen, V.-M., Petäjä, T., and Kulmala, M.: The role of ions in new particle formation in the CLOUD chamber, \*Atmos. Chem. Phys.\*, 17, 15181–15197, <https://doi.org/10.5194/acp-17-15181-2017>, 2017.](#)

1140 [Wamelink, G. W. W., de Knegt, B., Pouwels, R., Schuiling, C., Wegman, R. M. A., Schmidt, A. M., van Dobben, H. F., and Sanders, M. E.: Considerable environmental bottlenecks for species listed in the Habitats and Birds Directives in the Netherlands, \*Biological Conservation\*, 165, 43–53, <https://doi.org/10.1016/j.biocon.2013.05.012>, 2013.](#)

1145 [Wang, M., Kong, W., Marten, R., He, X.-C., Chen, D., Pfeifer, J., Heitto, A., Kontkanen, J., Dada, L., Kürten, A., Yli-Juuti, T., Manninen, H. E., Amanatidis, S., Amorim, A., Baalbaki, R., Baccarini, A., Bell, D. M., Bertozzi, B., Bräkling, S., Brilke, S., Murillo, L. C., Chiu, R., Chu, B., De Menezes, L.-P., Duplissy, J., Finkenzeller, H., Carracedo, L. G., Granzin, M., Guida,](#)

Formatted: Font: +Headings (Times New Roman)

Formatted: Font: +Headings (Times New Roman)

Formatted: Font: +Headings (Times New Roman)

Formatted: Font: +Headings (Times New Roman)

Formatted: Font: +Headings (Times New Roman)



R., Hansel, A., Hofbauer, V., Krechmer, J., Lehtipalo, K., Lamkaddam, H., Lampimäki, M., Lee, C., P., Makhmutov, V., Marie, G., Mathot, S., Mauldin, R. L., Mentler, B., Müller, T., Onnela, A., Partoll, E., Petäjä, T., Philippov, M., Pospisilova, V., Ranjithkumar, A., Rissanen, M., Rörup, B., Scholz, W., Shen, J., Simon, M., Sipilä, M., Steiner, G., Stolzenburg, D., Tham, Y. J., Tomé, A., Wagner, A. C., Wang, D. S., Wang, Y., Weber, S., K., Winkler, P. M., Wlasits, P. J., Wu, Y., Xiao, M., Ye, Q., Zauner-Wieczorek, M., Zhou, X., Volkamer, R., Riipinen, I., Dommen, J., Curtius, J., Baltensperger, U., Kulmala, M., Worsnop, D. R., Kirkby, J., Seinfeld, J. H., El-Haddad, I., Flagan, R. C., and Donahue, N. M.: Rapid growth of new atmospheric particles by nitric acid and ammonia condensation, *Nature*, 581, 184–189, <https://doi.org/10.1038/s41586-020-2270-4>, 2020.

Wang, M., Xiao, M., Bertozzi, B., Marie, G., Rörup, B., Schulze, B., Bardakov, R., He, X.-C., Shen, J., Scholz, W., Marten, R., Dada, L., Baalbaki, R., Lopez, B., Lamkaddam, H., Manninen, H. E., Amorim, A., Ataei, F., Bogert, P., Brasseur, Z., Caudillo, L., De Menezes, L.-P., Duplissy, J., Ekman, A. M. L., Finkenzeller, H., Carracedo, L. G., Granzin, M., Guida, R., Heinritzi, M., Hofbauer, V., Höhler, K., Korhonen, K., Krechmer, J., E., Kürten, A., Lehtipalo, K., Mahfouz, N. G. A., Makhmutov, V., Massabò, D., Mathot, S., Mauldin, R. L., Mentler, B., Müller, T., Onnela, A., Petäjä, T., Philippov, M., Piedadierro, A. A., Pozzer, A., Ranjithkumar, A., Schervish, M., Schobesberger, S., Simon, M., Stozhkov, Y., Tomé, A., Umo, N. S., Vogel, F., Wagner, R., Wang, D. S., Weber, S., K., Welti, A., Wu, Y., Zauner-Wieczorek, M., Sipilä, M., Winkler, P. M., Hansel, A., Baltensperger, U., Kulmala, M., Flagan, R. C., Curtius, J., Riipinen, I., Gordon, H., Lelieveld, J., El-Haddad, I., Volkamer, R., Worsnop, D. R., Christoudias, T., Kirkby, J., Möhler, O., and Donahue, N. M.: Synergistic  $\text{HNO}_3$ – $\text{H}_2\text{SO}_4$ – $\text{NH}_3$  upper tropospheric particle formation, *Nature*, 605, 483–489, <https://doi.org/10.1038/s41586-022-04605-4>, 2022.

Wehner, B., Werner, F., Ditas, F., Shaw, R. A., Kulmala, M., and Siebert, H.: Observations of new particle formation in enhanced UV irradiance zones near cumulus clouds, *Atmos. Chem. Phys.*, 15, 11701–11711, <https://doi.org/10.5194/acp-15-11701-2015>, 2015.

Wiedensohler, A., Wiesner, A., Weinhold, K., Birmili, W., Hermann, M., Merkel, M., Müller, T., Pfeifer, S., Schmidt, A., Tuch, T., Velarde, F., Quincey, P., Seeger, S., and Nowak, A.: Mobility particle size spectrometers: Calibration procedures and measurement uncertainties, *Aerosol Science and Technology*, 52, 146–164, <https://doi.org/10.1080/02786826.2017.1387229>, 2018.

Weimer, S., Alfarra, M. R., Schreiber, D., Mohr, M., Prévôt, A. S. H., and Baltensperger, U.: Organic aerosol mass spectral signatures from wood-burning emissions: Influence of burning conditions and wood type, *J. Geophys. Res.*, 113, D10304, <https://doi.org/10.1029/2007JD009309>, 2008.

Wiedensohler, A., Birmili, W., Nowak, A., Sonntag, A., Weinhold, K., Merkel, M., Wehner, B., Tuch, T., Pfeifer, S., Fiebig, M., Fjårraa, A. M., Asmi, E., Sellegri, K., Depuy, R., Venzac, H., Villani, P., Laj, P., Aalto, P., Ogren, J. A., Swietlicki, E., Williams, P., Roldin, P., Quincey, P., Hüglin, C., Fierz-Schmidhauser, R., Gysel, M., Weingartner, E., Riccobono, F., Santos, S., Gröning, C., Faloon, K., Beddows, D., Harrison, R., Monahan, C., Jennings, S. G., O’Dowd, C. D., Marinoni, A., Horn, H.-G., Keck, L., Jiang, J., Scheckman, J., McMurry, P. H., Deng, Z., Zhao, C. S., Moerman, M., Henzing, B., De Leeuw, G., Löschau, G., and Bastian, S.: Mobility particle size spectrometers: harmonization of technical standards and data structure to facilitate high quality long-term observations of atmospheric particle number size distributions, *Atmos. Meas. Tech.*, 5, 657–685, <https://doi.org/10.5194/amt-5-657-2012>, 2012.

Wong, J. P. S., Nenes, A., and Weber, R. J.: Changes in Light Absorptivity of Molecular Weight Separated Brown Carbon Due to Photolytic Aging, *Environ. Sci. Technol.*, 51, 8414–8421, <https://doi.org/10.1021/acs.est.7b01739>, 2017.

Wu, Z., Hu, M., Lin, P., Liu, S., Wehner, B., and Wiedensohler, A.: Particle number size distribution in the urban atmosphere of Beijing, China, *Atmospheric Environment*, 42, 7967–7980, <https://doi.org/10.1016/j.atmosenv.2008.06.022>, 2008.

Formatted: Font: +Headings (Times New Roman)

Formatted: Font: +Headings (Times New Roman)

Formatted: Font: +Headings (Times New Roman)

Formatted: Font: +Headings (Times New Roman)

Formatted: Font: +Headings (Times New Roman)

Formatted: Font: +Headings (Times New Roman)

Formatted: Font: +Headings (Times New Roman)

Formatted: Font: +Headings (Times New Roman)

Xing, J., Wang, J., Mathur, R., Wang, S., Sarwar, G., Pleim, J., Hogrefe, C., Zhang, Y., Jiang, J., Wong, D. C., and Hao, J.: Impacts of aerosol direct effects on tropospheric ozone through changes in atmospheric dynamics and photolysis rates, *Atmos. Chem. Phys.*, 17, 9869–9883, <https://doi.org/10.5194/acp-17-9869-2017>, 2017.

Formatted: Font: +Headings (Times New Roman)

Xu, W., Croteau, P., Williams, L., Canagaratna, M., Onasch, T., Cross, E., Zhang, X., Robinson, W., Worsnop, D., and Jayne, J.: Laboratory characterization of an aerosol chemical speciation monitor with PM<sub>2.5</sub> measurement capability, *Aerosol Science and Technology*, 51, 69–83, <https://doi.org/10.1080/02786826.2016.1241859>, 2017.

Zhang, Q., Jimenez, J. L., Canagaratna, M. R., Ulbrich, I. M., Ng, N. L., Worsnop, D. R., and Sun, Y.: Understanding atmospheric organic aerosols via factor analysis of aerosol mass spectrometry: a review, *Anal Bioanal Chem*, 401, 3045–3067, <https://doi.org/10.1007/s00216-011-5355-y>, 2011.

Formatted: Font: +Headings (Times New Roman)

Zhang, R., Khalizov, A., Wang, L., Hu, M., and Xu, W.: Nucleation and Growth of Nanoparticles in the Atmosphere, *Chem. Rev.*, 112, 1957–2011, <https://doi.org/10.1021/cr2001756>, 2012.

Zhang, X., McVay, R. C., Huang, D. D., Dalleska, N. F., Aumont, B., Flagan, R. C., and Seinfeld, J. H.: Formation and evolution of molecular products in  $\alpha$ -pinene secondary organic aerosol, *Proc. Natl. Acad. Sci. U.S.A.*, 112, 14168–14173, <https://doi.org/10.1073/pnas.1517742112>, 2015.

Zhao, D., Pullinen, I., Fuchs, H., Schrade, S., Wu, R., Acir, I.-H., Tillmann, R., Rohrer, F., Wildt, J., Guo, Y., Kiendler-Scharr, A., Wahner, A., Kang, S., Vereecken, L., and Mentel, T. F.: Highly oxygenated organic molecule (HOM) formation in the isoprene oxidation by NO<sub>3</sub> radical, *Atmos. Chem. Phys.*, 21, 9681–9704, <https://doi.org/10.5194/acp-21-9681-2021>, 2021.

Zheng, Y., Cheng, X., Liao, K., Li, Y., Li, Y. J., Huang, R.-J., Hu, W., Liu, Y., Zhu, T., Chen, S., Zeng, L., Worsnop, D. R., and Chen, Q.: Characterization of anthropogenic organic aerosols by TOF-ACSM with the new capture vaporizer, *Atmos. Meas. Tech.*, 13, 2457–2472, <https://doi.org/10.5194/amt-13-2457-2020>, 2020.

Formatted: Bibliography

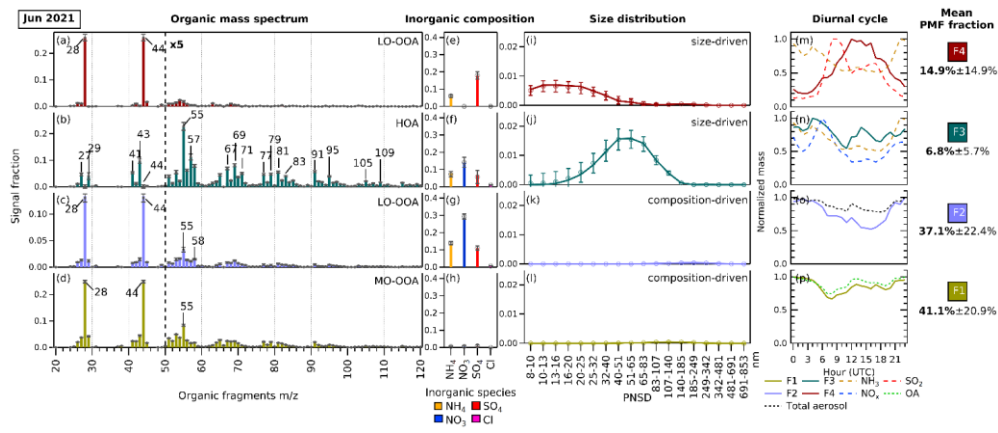
Supplementary Information – What chemical species are responsible for new particle formation and growth in the Netherlands? A hybrid positive matrix factorization (PMF) analysis using aerosol composition (ACSM) and size (SMPS)

S1. Figures and tables

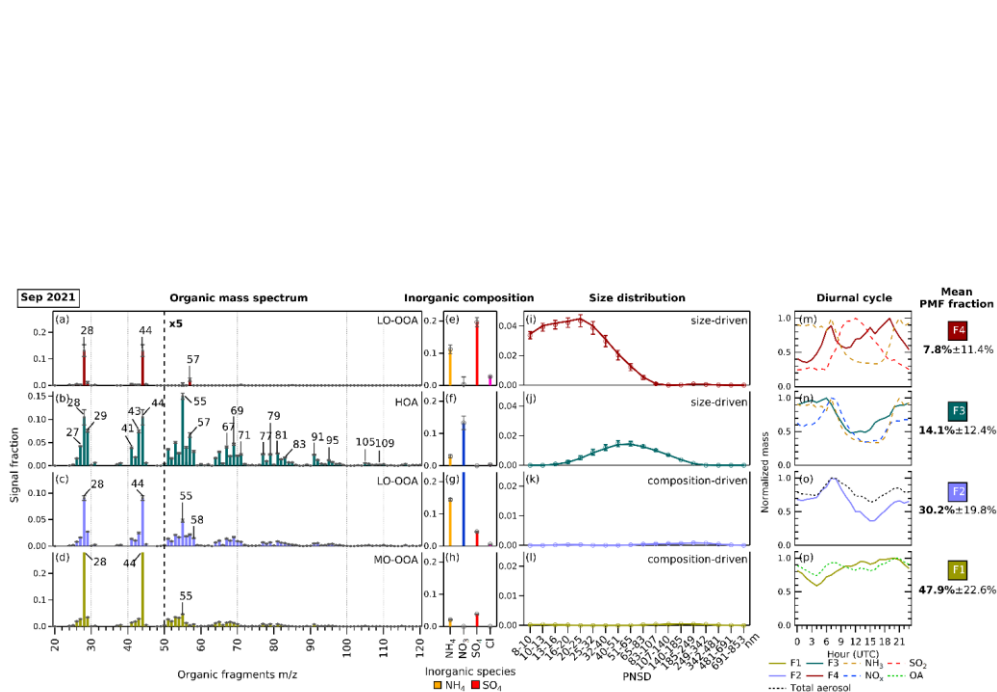
Table of Figures

Figure S1. The profiles of 6 factor solution from the combined ACSM-SMPS dataset in June 2021. ....2

Figure S2. The profiles of 6 factor solution from the combined ACSM-SMPS dataset in September 2021. ....3



**Figure S1.** The profiles of 4-factor PMF solution from the combined ACSM-SMPS dataset in June 2021. Each factor is split into three matrices with their own rescaled signal fraction axes. The error bars in each variable represents standard deviation generated by performing bootstrapped run of the solution. The panel a-d shows the organic fragment mass spectrum from m/z 20 to 120 from ACSM (m/z < 20 not included). The panel e-h shows the ACSM standard inorganic aerosol species concentrations (ammonium (NH<sub>4</sub>), nitrate (NO<sub>3</sub>), sulfate (SO<sub>4</sub>), and chloride (Cl)). The panel i-l shows the particle size distribution profiles from the SMPS. On the panel m-p, the diurnal cycles of the factors and related species are depicted. The mean PMF fractions and their standard deviations are shown indicating the mean contribution of each hybrid PMF factor to the “total variable reconstruction” by PMF throughout the period. The factors in May 2021 are assigned as: (F1) MO-OOA, (F2) NH<sub>4</sub>+NO<sub>3</sub>+SO<sub>4</sub>+LO-OOA, (F3) size-driven NH<sub>4</sub>+NO<sub>3</sub>+SO<sub>4</sub>+HOA, and (F4) size-driven NH<sub>4</sub>+SO<sub>4</sub>+LO-OOA.



**Figure S2.** The profiles of 4-factor PMF solution from the combined ACSM-SMPS dataset in September 2021. Each factor is split into three matrices with their own rescaled signal fraction axes. The error bars in each variable represents standard deviation generated by performing bootstrapped run of the solution. The panel **a-d** shows the organic fragment mass spectrum from  $m/z$  20 to 120 from ACSM ( $m/z < 20$  not included). The panel **e-h** shows the ACSM standard inorganic aerosol species concentrations (ammonium ( $\text{NH}_4$ ), nitrate ( $\text{NO}_3$ ), sulfate ( $\text{SO}_4$ ), and chloride ( $\text{Cl}$ )). The panel **i-l** shows the particle size distribution profiles from the SMPS. On the panel **m-p**, the diurnal cycle of the factors and related species are depicted. The mean PMF fractions and its standard deviation are shown indicating the mean contribution of each hybrid PMF factor to the “total variable reconstruction” by PMF throughout the period. The factors in May 2021 are assigned as: (F1) MO-OOA, (F2)  $\text{NH}_4+\text{NO}_3$ + LO-OOA, (F3) size-driven  $\text{NH}_4+\text{NO}_3$ +HOA, and (F4) size-driven  $\text{NH}_4+\text{SO}_4$ +LO-OOA.

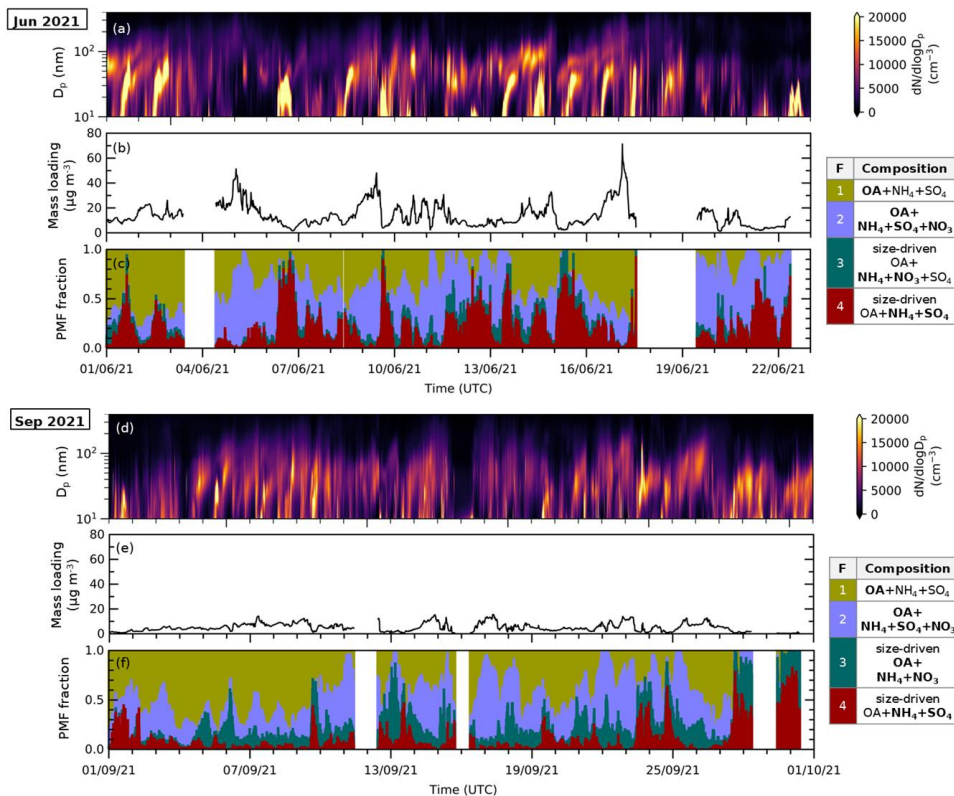


**Figure S3.** Time series of (a,d) particle size distribution (dN/dlogD<sub>p</sub>) in cm<sup>-3</sup> with logarithmic scale in particle size obtained from SMPS measurements, (b,e) total mass loading calculated from ACSM species concentration (using Tofware) in μg.m<sup>-3</sup>, and (c,f) reconstructed PMF fraction (stacked) from analyses in June and September 2021. — 4 Episodes of F4 and F3 coincide with relatively low total aerosol mass conditions and high fine particle concentrations.

Formatted: Font: Times New Roman, Not Bold

Formatted: Font: Times New Roman

Formatted: Font: Times New Roman

Formatted: Font: Times New Roman, Not Bold

Formatted: Caption, Indent: Left: 0 cm, First line: 0 cm, Tab stops: Not at 17.68 cm

Formatted: Font: Times New Roman

Formatted: Font: Times New Roman

Formatted: Font: Times New Roman, Not Bold

Formatted: Font: Times New Roman

Formatted: Font: Times New Roman

Formatted: Font: Times New Roman, Not Bold

Formatted: Font: Times New Roman, 9 pt, English (United Kingdom)

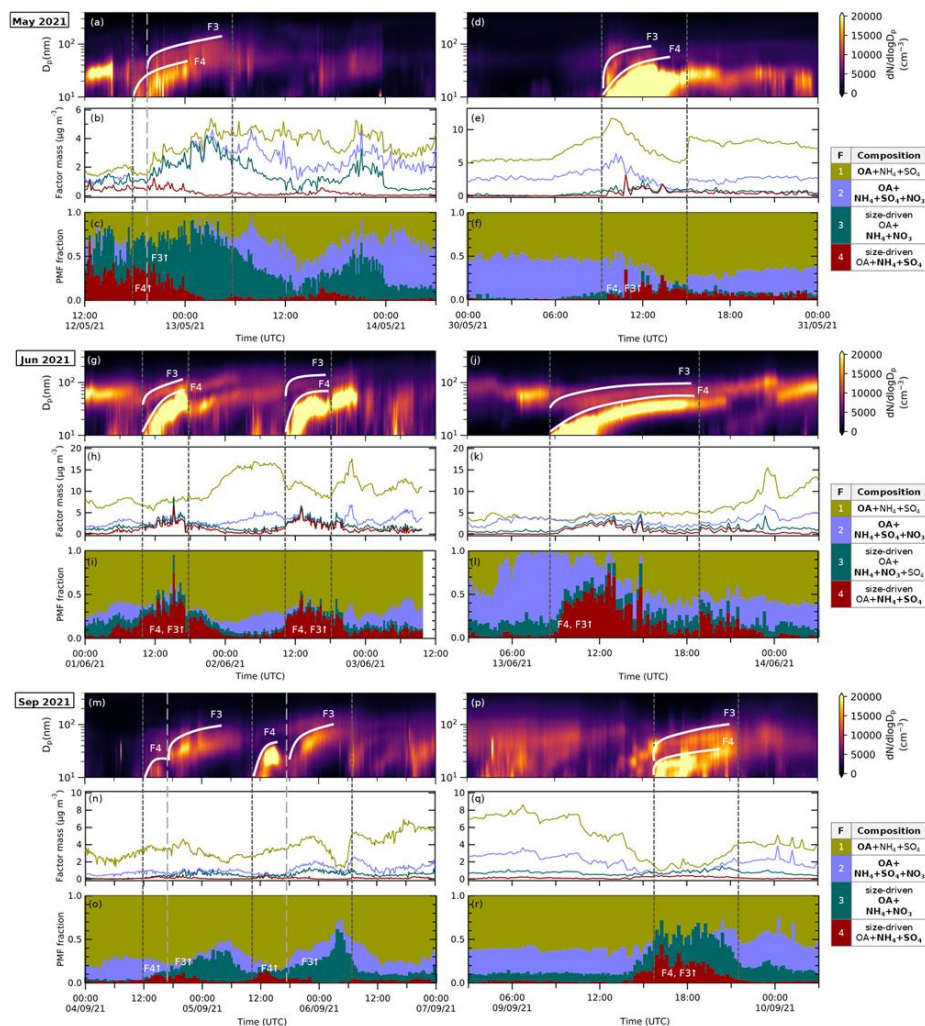


**Figure S4.** Selected timeseries windows during which new particle formation (NPF) events were detected by the scanning mobility particle sizer (SMPS) resembling ‘banana’ shapes in May 2021 (a-f), June 2021 (g-k) and September 2021 (m-r). Rapid increases of fine new particles were observed at (a) 30/05/2021 00:00 to 31/05/2021 00:00, (b) 13/06/2021 00:00 to 14/06/2021 00:00, and (c) 27/09/2021 12:00 to 28/09/2021 12:00. — During these events, the increase in size-driven factors F4 and F3 can be seen equally in the reconstructed PMF fraction time series. The results suggest the events occur with either simultaneous episodes of F4 and F3 (growth-mode) (d-f, g-i, j-l, p-r), or sequential episodes of both F4 and F3 (a-c, m-o).

Formatted: Font: Not Bold

Formatted: Font: Not Bold

Formatted: Caption, Indent: Left: 0 cm, First line: 0 cm, Tab stops: Not at 17.68 cm

Formatted: Font: +Headings (Times New Roman), 9 pt, Not Bold, English (United Kingdom)

Figure S5. Normalized diurnal cycles in June and September 2021 of (a) the size-driven factors of F6 and F5, and SO<sub>2</sub> as the sulfate precursor, and (b) the size-driven factors of F4 and F3.....6

Figure S6. Timeseries of (a) wind direction (WD) color-coded with wind speed (WS), and (b) reconstructed PMF fractions F6 and F5 (stacked) corresponding to nucleation-mode and first-growth-mode particles in June and September 2021. ....6

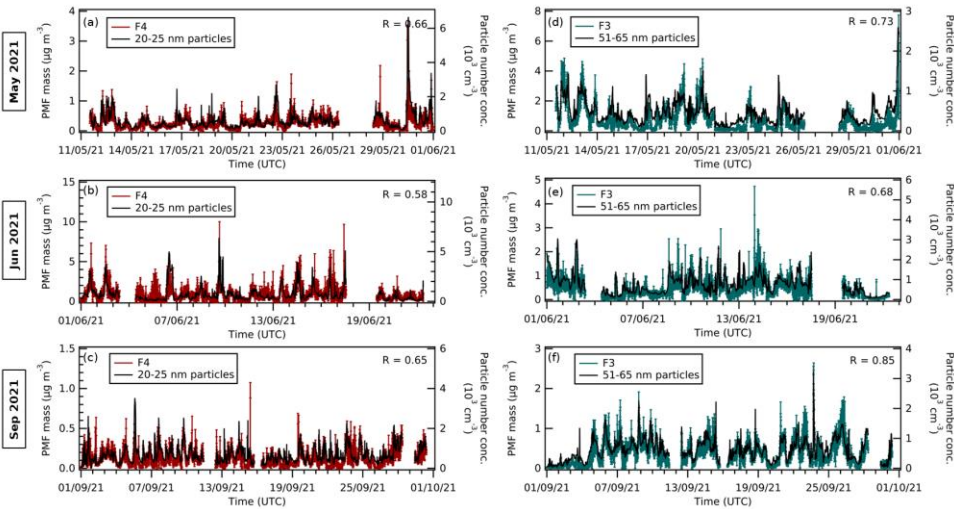
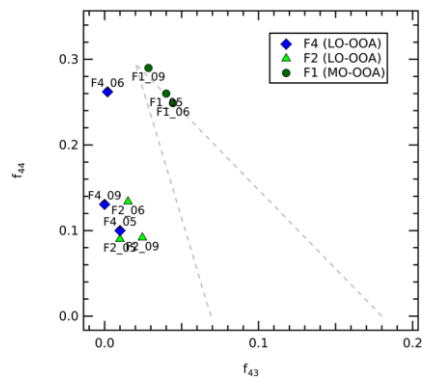
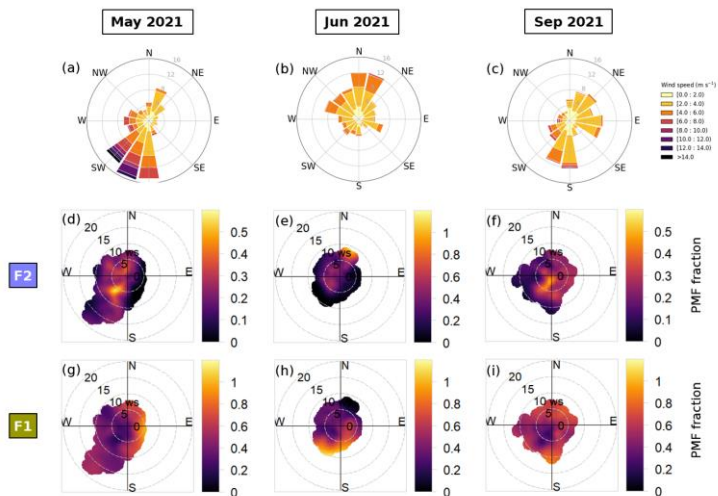


Figure S5. (a-c) The bootstrapped time series of F4 and number concentration of particles in the size bin of 20-25 nm and (d-f) the bootstrapped time series of F3 and number concentration of particles in the size bin of 51-65 nm in May 2021, June 2021, and September 2021. Both size bins are the median size of the size-driven factors' particle size distribution. The uncentered R Pearson coefficient shown on the right top of each graph shows the correlation between the time series of the factor and the particle number concentration.





**Figure S6.** The triangle plot showing  $f_{44}$  vs  $f_{43}$  signal for resolved LO-OOA in F4 (dark blue, diamond), LO-OOA in F2 (light green, triangle), and MO-OOA in F1 (dark green, dots). The number indicated after the factor's number corresponds to the period (05 for May, 06 for June, and 09 for September). We note that the June F4 signature is closer to the MO-OOA ratios (see Sect. 3.3.3 for discussion). Moving to the top of the triangle means a more oxidized OA. As the measurements were carried on using capture vaporizer (CV) and the triangle plot was first developed for mass spectrometry with standard vaporizer (SV), some of the  $f_{44}/f_{43}$  values are outside the triangle.



**Figure S7.** (a-c) Wind roses and (d-i) bivariate polar plots of nucleation-mode particle precursor concentrations composition-driven factor mass fraction (F2 and F1) by wind speed and wind direction measured in Cabauw in May, June, and September 2021.

7 The bulk OA+IA factor (F2, d-f) is shown to be originated from different directions, while the bulk OA factor (F1, g-i) is mainly coming from the easterly and southerly sector.

Formatted: Font: Times New Roman

Formatted: Font: Not Bold

Formatted: Font: Not Bold

Formatted: Caption, Indent: Left: 0 cm, First line: 0 cm, Tab stops: Not at 17.68 cm

Formatted: Font: Not Bold

Formatted: Font: +Headings (Times New Roman), 9 pt, Bold, English (United Kingdom)



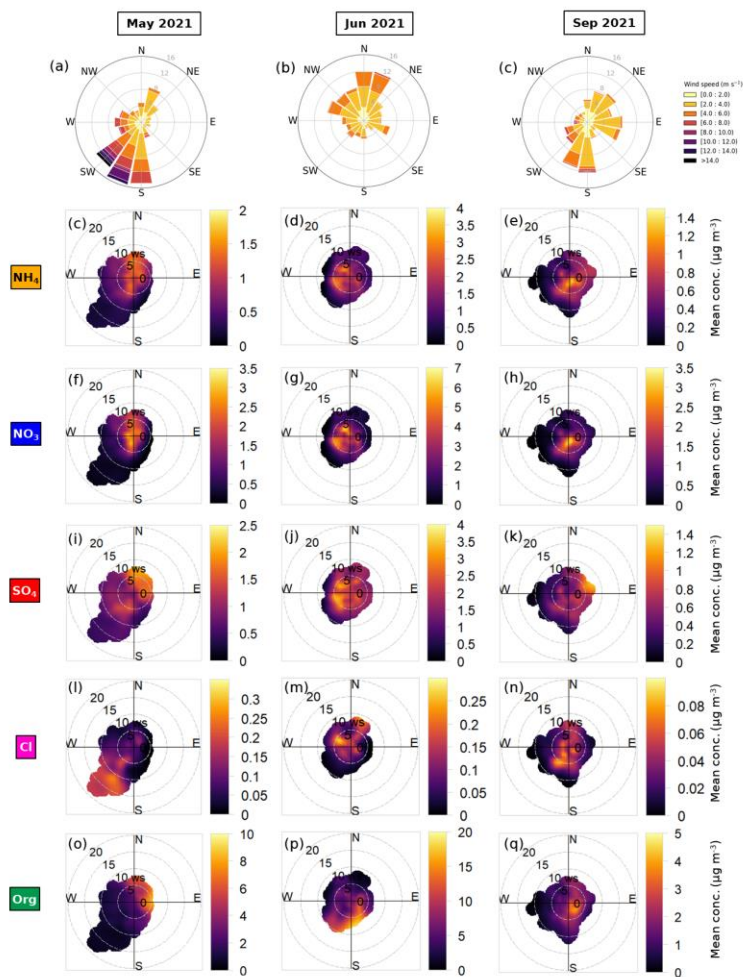


**Figure S8.** (a-c) Wind roses and (d-q) bivariate polar plots of ACSM-generated chemical species by wind speed and wind direction measured in Cabauw in May, June, and September 2021. The species include ammonium ( $\text{NH}_4$ , c-e), nitrate ( $\text{NO}_3$ , f-h), sulfate ( $\text{SO}_4$ , i-k), chloride ( $\text{Cl}$ , l-n), and organics (Org, o-q) in 10-minute resolution.  $\text{NO}_3$  and  $\text{SO}_4$  are found to be correlated to  $\text{NH}_3$  source direction (see Fig. S9) across seasons due to formation of ammonium nitrate and sulfate.  $\text{NO}_3$  are correlated with the southern and western sector of the site.  $\text{SO}_4$  is correlated to westerlies and north-easterlies, influenced by both  $\text{NH}_3$  and  $\text{SO}_2$  source direction since they react forming ammonium sulfate (Fig. S9).

Formatted: Font: Times New Roman

Formatted: Font: Times New Roman, Not Bold

Formatted: Font: Times New Roman, Not Bold

Formatted: Caption, Indent: Left: 0 cm, First line: 0 cm, Tab stops: Not at 17.68 cm

Formatted: Font: Times New Roman, 9 pt, English (United Kingdom)

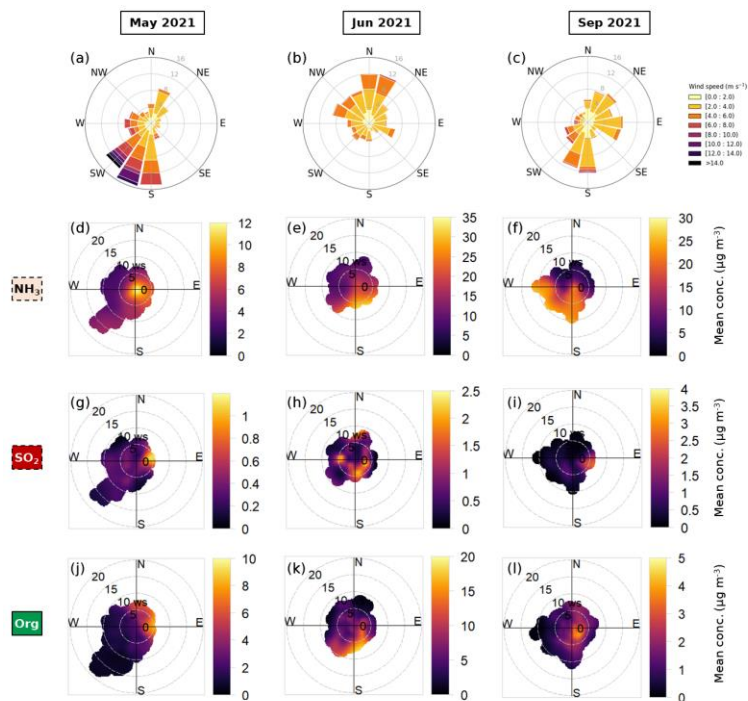


Figure S9.—Diurnal cycles of F2 and total aerosol mass loading measured by the ACSM (top) with associated composition (bottom) across periods..... 10  
(a-c) Wind roses and (d-l) Figure S10.—Diurnal cycles of F1 and total OA measured by ACSM in May, June, and September 2021 are shown (left), with associated composition (middle) and bivariate polar plots of F1 concentration by wind speed and direction (right) in 10-minute resolution..... 13

## Table of Tables

Table S1.— Mean bulk atmospheric chemical composition in the three period as detected by the ToF ACSM and collocated gas measurements in Cabauw..... 11

Formatted: Font: +Headings (Times New Roman)

Formatted: Font: Not Bold, Font color: Text 1

Formatted: Indent: Left: 0 cm, First line: 0 cm

Formatted: Font: Not Bold

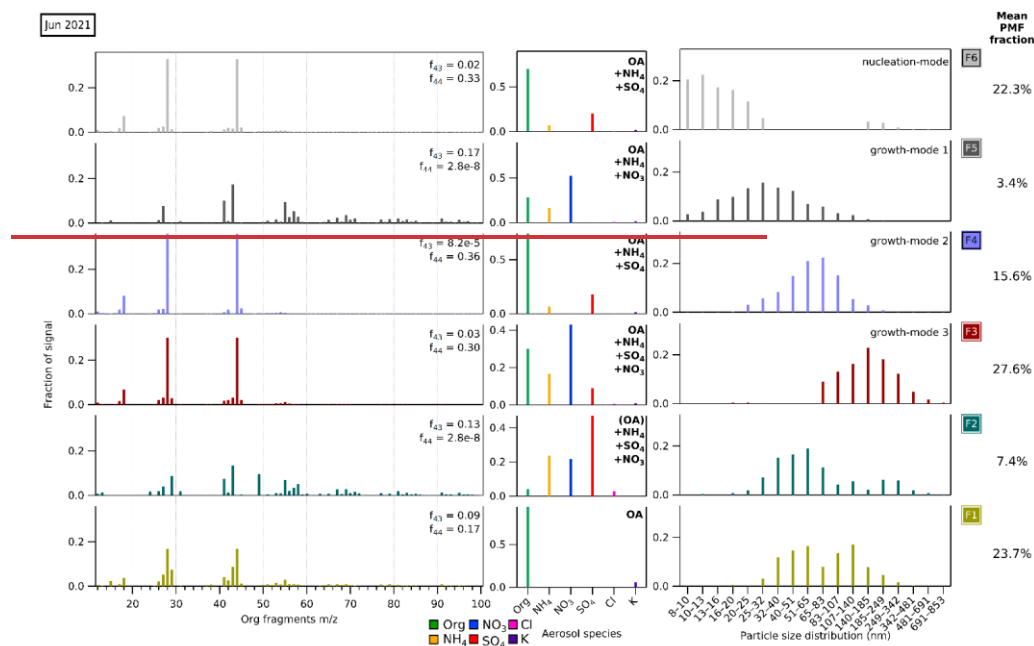


**Figure S1.** The profiles of 6-factor solution from the combined ACSM-SMPS dataset in June 2021. Each factor is split into three matrices with their own signal fraction axes. The lefthand panel shows the organic fragment mass spectrum profiles from ACSM. The values of  $f_{44}$  ( $\text{CO}_3^-$ -fragment) representing higher-oxidation level and  $f_{43}$  ( $\text{CH}_3\text{CO}^-$  and  $\text{C}_2\text{H}_5^-$ ) representing lower-oxidation level are given. The middle panel shows the ACSM standard aerosol species concentrations (organics (Org), ammonium ( $\text{NH}_4$ ), nitrate ( $\text{NO}_3$ ), sulfate ( $\text{SO}_4$ ), chloride (Cl), and potassium (K)). The righthand panel shows the particle size distribution profiles from the SMPS. The mean PMF fractions are shown related to the right, indicating the mean contribution of each hybrid PMF factor to the “total variable reconstruction” by PMF throughout the period (note we have reordered factors to be consistent across the 3 months). The factors in May 2021 are assigned as: (F1) OA, (F2) (OA) +  $\text{NH}_4$  +  $\text{SO}_4$  +  $\text{NO}_3$ , (F3) growth mode 3 OA +  $\text{NH}_4$  +  $\text{SO}_4$  +  $\text{NO}_3$ , (F4) growth mode 2 OA +  $\text{NH}_4$  +  $\text{SO}_4$ , (F5) growth mode 1 OA +  $\text{NH}_4$  +  $\text{NO}_3$ , and (F6) nucleation-mode OA +  $\text{NH}_4$  +  $\text{SO}_4$ . Factors with OA listed inside parentheses indicates OA below 25% of the total mass.

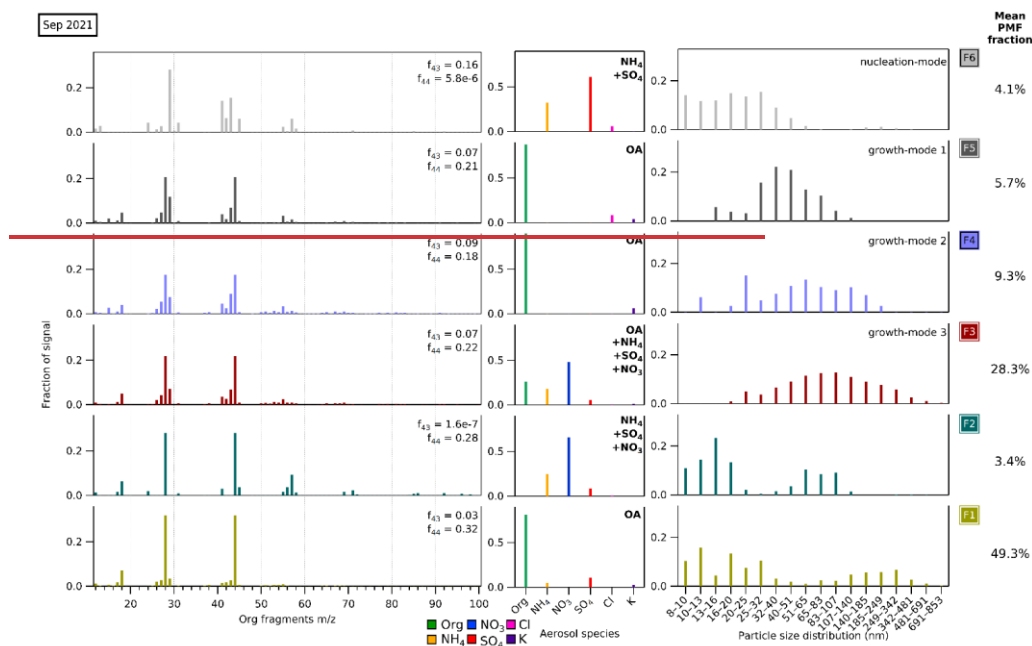


**Figure S2.** The profiles of 6-factor solution from the combined ACSM-SMPS dataset in September 2021. Each factor is split into three matrices with their own signal fraction axes. The lefthand panel shows the organic fragment mass spectrum profiles from ACSM. The values of  $f_{43}$  (CO<sub>2</sub><sup>-</sup> fragment) representing higher oxidation level and  $f_{44}$  (CH<sub>3</sub>CO<sup>-</sup> and C<sub>3</sub>H<sub>7</sub><sup>-</sup>) representing lower oxidation level are given. The middle panel shows the ACSM standard aerosol species concentrations (organics (Org), ammonium (NH<sub>4</sub>), nitrate (NO<sub>3</sub>), sulfate (SO<sub>4</sub>), chloride (Cl), and potassium (K)). The righthand panel shows the particle size distribution profiles from the SMPS. The mean PMF fractions are shown to the right, indicating the mean contribution of each hybrid PMF factor to the “total variable reconstruction” by PMF throughout the period (note we have reordered factors to be consistent across the 3 months). The factors in May 2021 are assigned as: (F1) OA, (F2) NH<sub>4</sub>+SO<sub>4</sub>+NO<sub>3</sub>, (F3) growth mode 3 OA+NH<sub>4</sub>+SO<sub>4</sub>+NO<sub>3</sub>, (F4) growth mode 2 (OA)+NH<sub>4</sub>+SO<sub>4</sub>, (F5) growth mode 1 OA, and (F6) nucleation-mode (OA)+NH<sub>4</sub>+SO<sub>4</sub>. Factors with OA listed inside parentheses indicates OA below 25% of the total mass. Some factor profiles may have organic fragments mass spectrum despite negligible or no ACSM organic composition (Org) variable contribution. We interpret these fragments showing the profile of trace OA that is insufficient to result in a significant contribution of the Org variable.

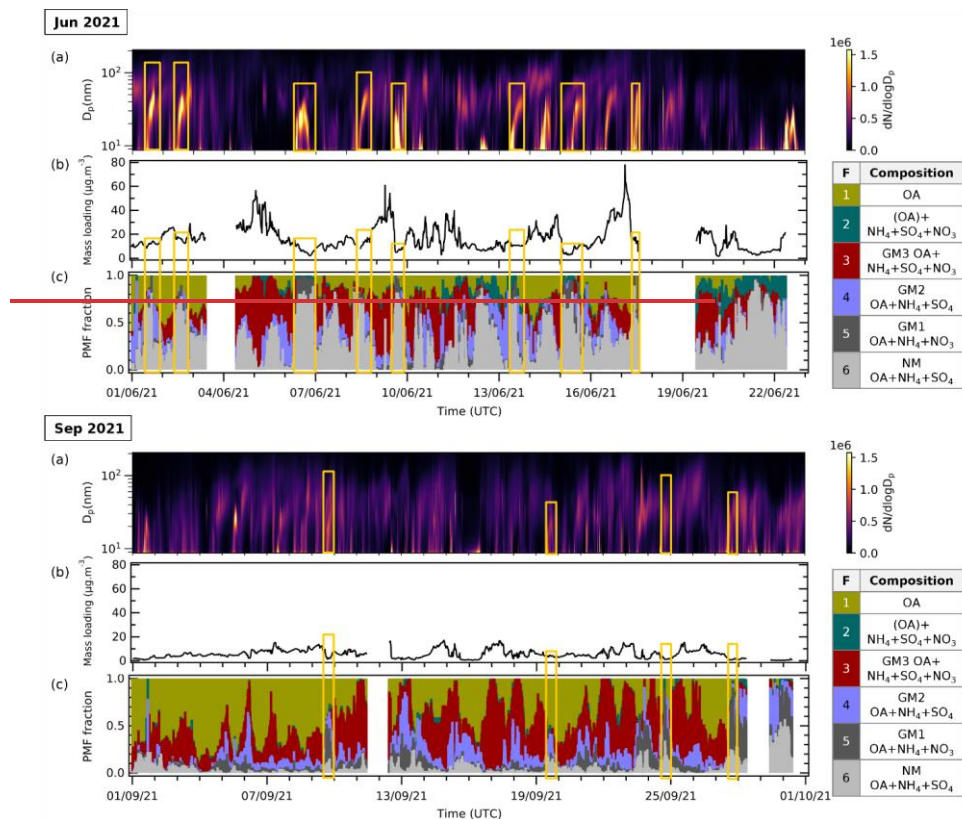


**Figure S3.** Time-series of (a) particle size distribution ( $dN/d\log D_p$ ) in  $\text{cm}^{-3}$  with logarithmic scale in particle size obtained from SMPS measurements, (b) total mass loading calculated from ACSM species concentration (using Tofware) in  $\mu\text{g}\cdot\text{m}^{-3}$ , and (c) reconstructed PMF fraction (stacked) from analyses in June and September 2021. Orange outlined sections indicate periods during which high episodes of size-driven factors are observed. These episodes coincide with relatively low total aerosol mass conditions and high fine particle concentrations.

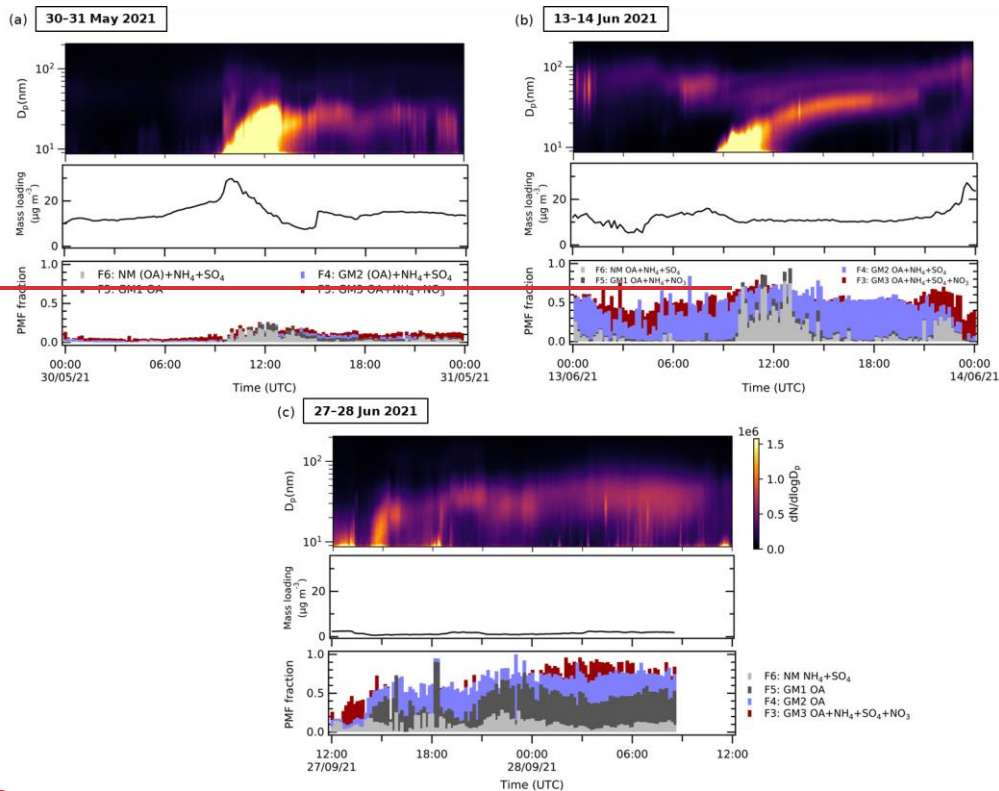


**Figure S4.** Selected timeseries windows during which new particle formation (NPF) events were detected by the scanning mobility particle sizer (SMPS) resembling 'banana'-shapes at (a) 30 May 2021 00:00 to 31 May 2021 00:00 UTC, (b) 13 Jun 2021 00:00 to 14 Jun 2021 00:00 UTC, and (c) 27-Sep 2021 12:00 to 28 Sep 2021 12:00 UTC. **Rapid increases of fine new particles were observed.** During these events, the increase in size-driven factors F7 and F6 can be seen equally in the reconstructed PMF fraction time series.

Formatted: Font: Bold

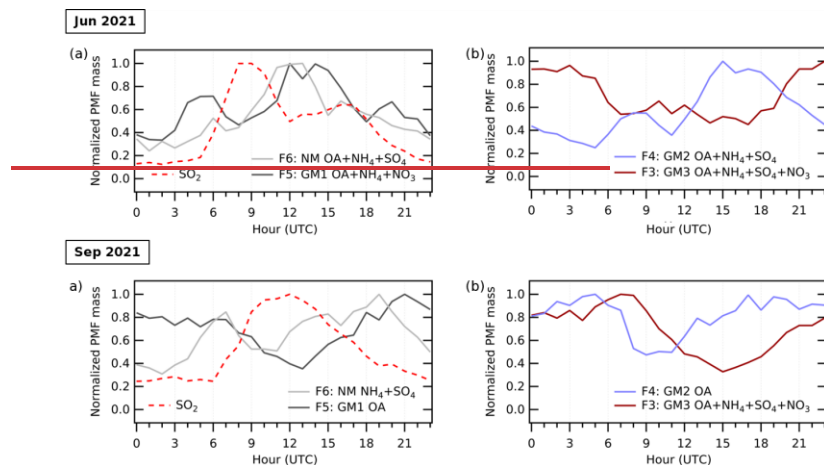


**Figure S5.** Normalized diurnal cycles in June and September 2021 of (a) the size-driven factors of F6 and F5, and SO<sub>2</sub> as the sulfate precursor, and (b) the size-driven factors of F4 and F3. Notice that from F6 to F3, the factors' diurnal pattern shifted from high daytime to high nighttime concentration.

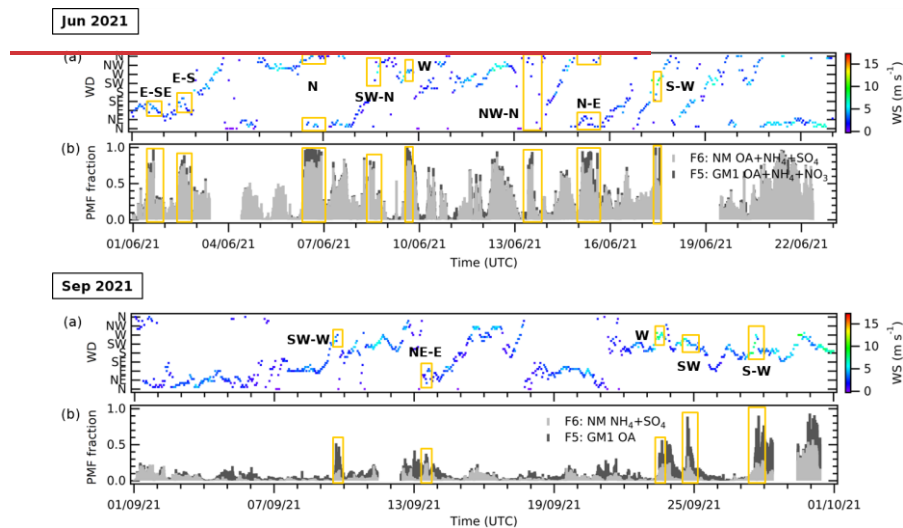


**Figure S6.** Timeseries of (a) wind direction (WD) color-coded with wind speed (WS), and (b) reconstructed PMF fractions F6 and F5 (stacked) corresponding to nucleation-mode and first growth-mode particles in June and September 2021. Orange outlined sections indicate high F6 and F5 episodes. We can observe that new particle formation is correlated with air masses from the southwesterly-westerly sector or northerly-easterly sector.



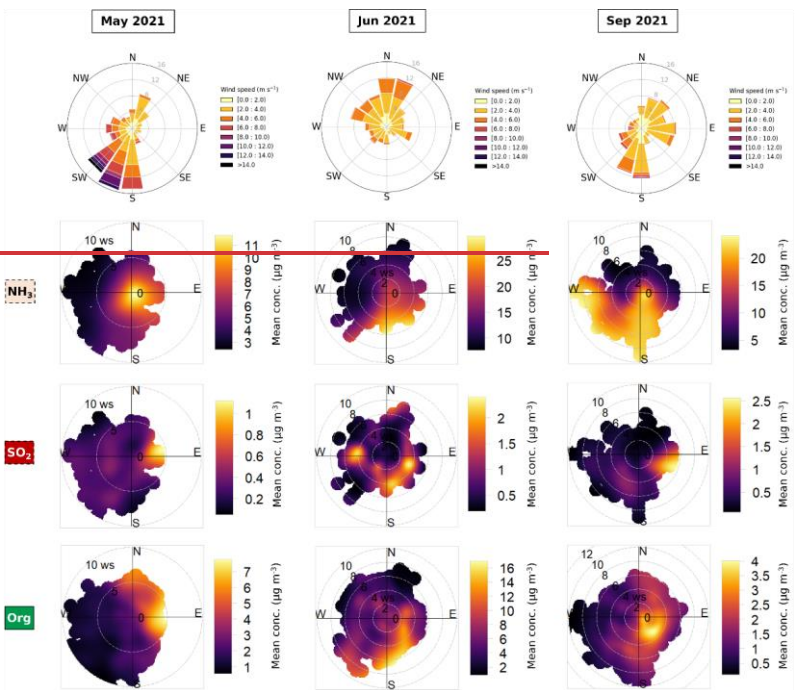


**Figure S7.** Wind roses and bivariate polar plots of nucleation-mode particle precursor concentrations by wind speed and wind direction measured in Cabauw in May, June, and September 2021. The species include ammonia ( $\text{NH}_3$ , d-f) and sulfur dioxide ( $\text{SO}_2$ , g-i) in the gaseous phase in hourly resolution, and organics (Org, j-l) in the aerosol phase in 10-minute resolution.  $\text{NH}_3$  is predominant around the site, particularly from the southern sector.  $\text{SO}_2$  is prevalent from the east and west of the site. Org species are predominantly coming from the eastern sector explaining the correlation of nucleation-mode factor (F6F4) episodes with easterlies in May and June 2021 when OA participates in early NPF.



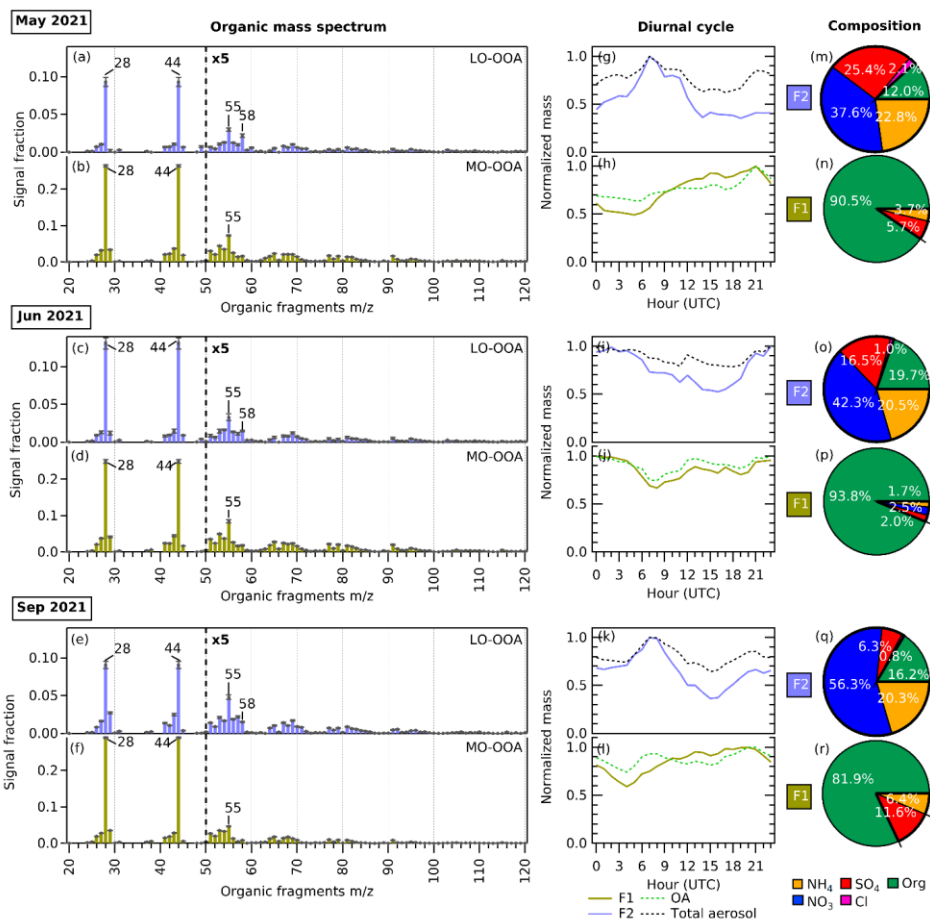


**Figure S10.** (a-f) Organic mass spectrum from  $m/z$  20 to 120 ( $m/z < 20$  not included) of F2 (purple) showing LO-OOA factor profiles and F1 (lime green) showing MO-OOA factor profiles in May 2021, June 2021, and September 2021. The error bars in each  $m/z$  were generated from bootstrap run. (g-l) The diurnal cycles of F2, consisting of OA and IA mixture, follows the diurnal pattern of total bulk aerosol pattern, while F1, mainly consisting of OA, follows the diurnal pattern of bulk OA measured by ToF-ACSM (Org). The MO-OOA F1 concentration increase slightly during the day due to photochemical activity and then concentrated in the boundary layer after sunset. It decreases around the midnight until morning due to

Formatted: Font: Times New Roman

absence of photochemistry.

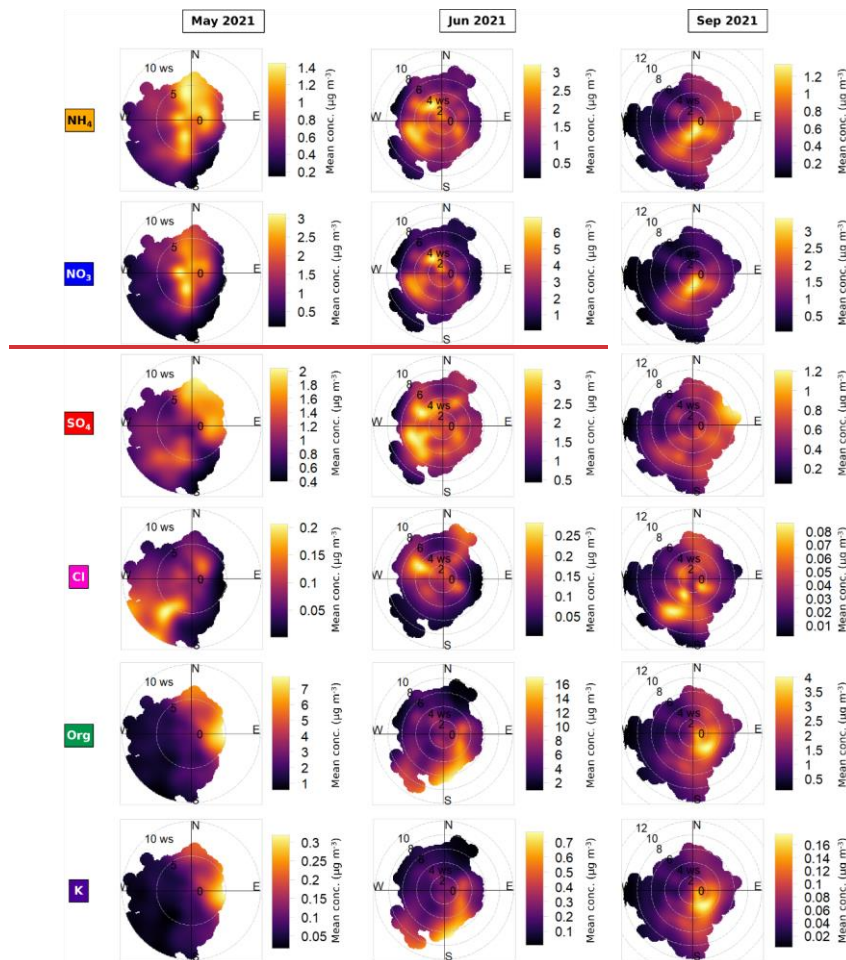


**Figure S8.** Wind roses MO-OAA in F1 shows a more stable diurnal cycle pattern with some increase from the morning to afternoon due to photochemistry. The concentration is accumulated in the evening due to shallow boundary layer and bivariate polar plots then diminishes in the early morning due to absence of ACSM-generated chemical photochemistry. (m-n) Pie charts showing mass percentage of each aerosol species by wind speed and wind direction measured in Cabauw contributing to each composition-driven factor in May 2021, June 2021, and September 2021. The species include Green represents organics (Org), orange represents ammonium (NH<sub>4</sub>), dark blue represents nitrate (NO<sub>3</sub>), dark red represents sulfate (SO<sub>4</sub>), and pink represents chloride (Cl), organics (Org), and potassium (K) in 10-minute resolution. NO<sub>3</sub> and SO<sub>4</sub> are found to be correlated to NH<sub>4</sub> source direction (see Fig. S7). across seasons due to formation of dominated by ammonium sulfate while F3 are dominated by ammonium nitrate and sulfate. NO<sub>3</sub> are correlated with the southern and western sector of the site. SO<sub>4</sub> is

Formatted: Justified

Formatted: Font: Times New Roman

Formatted: Font: Times New Roman

Formatted: Font: Times New Roman

Formatted: Font: Times New Roman

Formatted: Font: Times New Roman

Formatted: Font: Times New Roman

Formatted: Font: Times New Roman

Formatted: Font: Times New Roman

Formatted: Font: Times New Roman

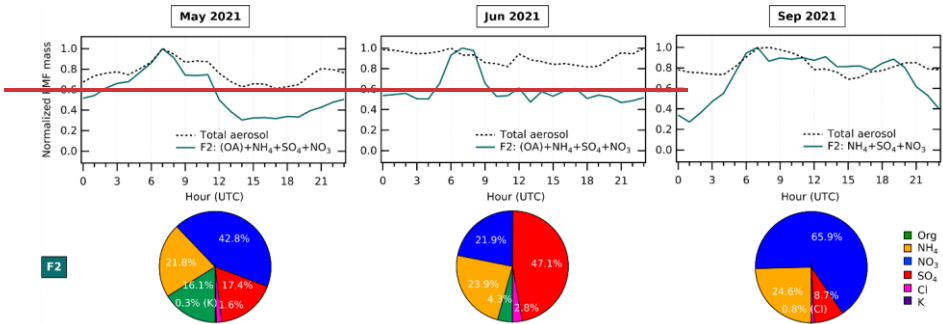
Formatted: Font: Times New Roman

Formatted: Font: Times New Roman

Formatted: Font: Times New Roman

150 correlated to westerlies and north-easterlies, influenced by both  $\text{NH}_3$  and  $\text{SO}_2$  source direction since they react forming ammonium sulfate (see Fig. S7). As trace ions, Cl is correlated with  $\text{SO}_4$ , while K is correlated with Org.

Formatted: Font: Times New Roman, Not Bold



155 **Figure S9.** Diurnal cycles of F2 and total aerosol mass-loading measured by the ACSM (top) with associated composition (bottom) across periods. F2 has a higher daytime value that resembles the diurnal cycle of total aerosol concentration except in summer (June).

160 **S2. Determining Atmospheric composition regimes from bulk atmospheric composition and aerosol formation**

**Ion balance ratio/ammonium balance**

165 The ion balance ratio ( $n_{\text{NH}_4^+}$ , or also called ammonium balance ( $\text{NH}_4 \text{ bal} = n_{\text{NH}_4^+} / (n_{\text{NO}_3^-} + 2 \times n_{\text{SO}_4^{2-}} + n_{\text{Cl}^-})$ ), is used to assess the ion-pairing between cations and anions forming inorganic aerosol (IA). Ambient aerosol is normally charge-balanced, meaning that the major cation ( $\text{NH}_4^+$ ) and anion species ( $\text{NO}_3^-$ ,  $\text{SO}_4^{2-}$ , and  $\text{Cl}^-$ ) should have one-to-one molar ratio. To calculate the ion balance ratio, we compare the measured ammonium molar concentration ( $n_{\text{NH}_4^+}$ ) to the total ammonium needed to neutralize the measured major anion concentration ( $n_{\text{NO}_3^-} + 2 \times n_{\text{SO}_4^{2-}} + n_{\text{Cl}^-}$ ). In spring (May), the ion balance is 0.99 which can be regarded as unity, meaning that the ion charge is fully neutralized. In summer (June), the ion balance ratio is less than unity (0.98). This may be caused by aerosol acidity. When the  $\text{NH}_4 \text{ bal} < 1$  (Farmer et al., 2010; Docherty et al., 2011) with excess in  $\text{H}^+$  aerosol being undetected by the instrument. Alternatively, nitrate or sulfate may be present in compounds other than ammonium salts. They. The anions can form salts refractory compounds with undetected other cations (e.g.,  $\text{NaNO}_3$ ,  $\text{Na}_2\text{SO}_4$ ,  $\text{Ca}(\text{NO}_3)_2$ ) and thus be less efficiently detected by the spectrometer, or exist in form of organic nitrates and organic sulfates, yielding an additional amount of nominal nitrate and sulfate measured by ACSM (Farmer et al., 2010; Docherty et al., 2011) detected by ACSM. It also may be caused by excess aerosol acidity (Farmer et al., 2010; Docherty et al., 2011). The ion balance ratio in autumn (September) is larger than unity (1.08). This can arise from ) although the clear relationship between  $\text{NH}_4 \text{ bal}$  and high aerosol acidity ( $\text{pH} < 0$ ) is observed for mass spectrometry measurements only when  $\text{NH}_4 \text{ bal} < 0.65$  (Schueneman et al., 2021). On the other hand, when the  $\text{NH}_4 \text{ bal} > 1$ , uncharged amines may be detected as ammonium by the ACSM (Farmer et al., 2010; Docherty et al., 2011), or from the presence of unmeasured anions such as carboxylates.

Commented [NF1]: 8) Section S2. Further clarification needed be added in this section to discuss the thermodynamics vs kinetic that may be controlling NPF and the aerosol composition in general. It is recommended that Weber et al. (2016) and Pye et al. (2020) reviewed and incorporated in the discussions here, for the following reasons.

Formatted: Font: Italic

Formatted: Font: +Headings (Times New Roman)

Formatted: Font: Italic

Commented [NF2]: 8.2) It is nearly impossible to say anything about aerosol acidity in the boundary layer just with charge balance calculated with the ACSM/AMS. E.g., it was not until the ammonium balance dropped below 0.65 could aerosol acidity be directly related to the charge balance measured on the AMS (ACSM) (Schueneman et al., 2021).

Commented [NF3]: 8.3) Though  $\text{NO}_3$  and  $\text{SO}_4$  would be visible other cations, generally, both the cations and anions would be easily observable due to the higher boiling point and the aerosol being more refractory. It would be recommended to say that the cations and anions from these salts would be slowly detected and not "not detected." (Line 939 SI).

may be present. The aerosol species excess for each period can be deduced from the aerosol formation chemistry in a  $\text{HNO}_3$ - $\text{NH}_3$ - $\text{H}_2\text{SO}_4$ - $\text{H}_2\text{O}$  system (Ansari and Pandis, 1998; Seinfeld and Pandis, 2016; Tsai et al., 2016). When the molar ion balance ratio of free ammonia to sulfate total is larger than two,  $\text{NH}_3$  prefers to react homogeneously with  $\text{H}_2\text{SO}_4$  to form ammonium sulfate ( $(\text{NH}_4)_2\text{SO}_4$ ). The rest of  $\text{NH}_3$  will react with  $\text{HNO}_3$  to form ammonium nitrate ( $\text{NH}_4\text{NO}_3$ ) (Ansari and Pandis, 1998). The surplus is calculated based on the assumption that all available sulfate reacts with ammonia first to form  $(\text{NH}_4)_2\text{SO}_4$ . The remaining  $\text{NH}_3$  forms  $\text{NH}_4\text{NO}_3$  with nitrate and can result in either ammonium or an overabundance of nitrate.

In spring (May), summer (June), and autumn (September) are 0.997, 0.986, and 1.066 respectively, which can be regarded as close to unity. Therefore, we observe roughly a doubling in can infer that the bulk aerosol concentration charge is fully neutralized for all IA and an increase with a factor 2.6 in OA compared to May. This increase is mainly due to increasing anthropogenic activities, photosynthesis, and evapotranspiration of plants in summer. However, a mean nitrate excess is still observed ( $n_{\text{NH}_4^+}/(n_{\text{NO}_3^-} + 2 \times n_{\text{SO}_4^{2-}} + n_{\text{Cl}^-}) < 1$ ). In autumn (September), the particle concentrations decrease again, with a relatively larger decrease for sulfate. The discrepancy between the decrease of sulfate and other IA species concentrations in September leads to a change in ion balance ratio, generating the ammonium excess discussed previously ( $n_{\text{NH}_4^+}/(n_{\text{NO}_3^-} + 2 \times n_{\text{SO}_4^{2-}} + n_{\text{Cl}^-}) > 1$ ). In addition, to illustrate how the concentration of sulfate relates to nitrate, we introduce the mean sulfate-to-nitrate molar concentration ratio ( $n_{\text{SO}_4^{2-}}/n_{\text{NO}_3^-}$ ). The values of  $n_{\text{SO}_4^{2-}}/n_{\text{NO}_3^-}$  in May, June, and September were 0.41, 0.43, and 0.23 respectively (see summary in Table S1). A lower  $n_{\text{SO}_4^{2-}}/n_{\text{NO}_3^-}$  as found in autumn (September) suggests a more sulfate-poor regime, while a higher  $n_{\text{SO}_4^{2-}}/n_{\text{NO}_3^-}$  in spring (May) and summer (June) indicates a more sulfate-rich composition periods.

Besides the two previous ratios, the mean organic-to-ammonium mass ratio ( $m_{\text{Org}}/m_{\text{NH}_4}$ ) is used to indirectly compare the composition of IA and OA of factors across periods. Ammonium is a good representation of IA, as ammonium salts are the dominant inorganic species in the atmosphere. A mass ratio ( $m_{\text{Org}}/m_{\text{NH}_4}$ ) is used instead of molar ratio because organic species are measured as a mixture of various organic compounds by ToF-ACSM. The  $m_{\text{Org}}/m_{\text{NH}_4}$  values in May, June, and September were 2.47, 3.36, and 2.90, respectively (see summary in Table S1). The higher value observed in June implies an organic-rich regime, while the other months are in a more inorganic regime.

**Table S1.** Mean bulk atmospheric chemical composition in the three period as detected by the ToF-ACSM and ~~collocated~~co-located gas measurements in Cabauw. The ion balance ratio ( $n_{\text{NH}_4^+}/(n_{\text{NO}_3^-} + 2 \times n_{\text{SO}_4^{2-}} + n_{\text{Cl}^-})$ ) was unity in May, less than unity in June, and more than unity in September. An overabundance of nitrate was found in May and June, while ammonium excess is found in September.

Species/ratio	Mean concentration in May 2021 (spring)		Mean concentration in Jun 2021 (summer)		Mean concentration in Sep 2021 (autumn)	
	Mass ( $\mu\text{g m}^{-3}$ )	Molar ( $10^{-4} \text{ mol m}^{-3}$ )	Mass ( $\mu\text{g m}^{-3}$ )	Molar ( $10^{-4} \text{ mol m}^{-3}$ )	Mass ( $\mu\text{g m}^{-3}$ )	Molar ( $10^{-4} \text{ mol m}^{-3}$ )
$\text{NH}_3^{\text{§(a)}}$	7.03	41.37	15.25	89.56	12.67	74.37

$\text{NO}_x = \text{NO} + \text{NO}_2$	9.55	21.79	10.90	24.90	14.78	34.08
$\text{SO}_2$	0.34	0.54	0.85	1.33	0.59	0.91
Total aerosol <sup>(b)</sup>	6.60	-	14.12	-	5.15	-
Org	2.49	-	6.3736	-	2.4418	-
$\text{NO}_3^-$	1.84	2.97	3.42	5.52 <sup>***</sup>	1.5760	2.5358
$\text{NH}_4^+$	1.01	5.61	1.90	10.54	0.7475	4.10 <sup>***17</sup>
$\text{SO}_4^{2-}$	1.15	1.20 ( $\times 2 = 2.40$ )	2.29	2.39 ( $\times 2 = 4.78$ )	0.5556	0.5758 ( $\times 2 = 1.1416$ )
$\text{Cl}^-$	0.11	0.30	0.15	0.42	0.05	0.1314
$\text{K}^+/\text{NH}_4^+ \text{ bal}^{(c)}$	0.08	0.21997 $\pm$ 0.001	0.23	0.58986 $\pm$ 0.001	0.09	1.066 $\pm$ 0.23001
$\text{n}_{\text{NH}_4^+}/(\text{n}_{\text{NO}_3^-} + 2 \times \text{n}_{\text{SO}_4^{2-}})$ ***	-	0.99	-	0.98	-	1.08
$\text{n}_{\text{SO}_4^{2-}}/\text{n}_{\text{NO}_3^-} m_{\text{Org}}/m_{\text{In}}^{(d)}$	-0.61	0.41	-0.82	0.43	-0.74	0.23
$m_{\text{Org}}/m_{\text{In}}$	2.47	-	3.36	-	2.90	-
Composition regime	sulfate-rich		nitrate excess, organic- and sulfate-rich		ammonium excess, sulfate-poor	

<sup>\*(a)</sup> Data taken from Zegveld-Oude Meije measurement station

<sup>\*\*\*</sup> Aerosol species that are found having excess quantity

<sup>\*\*\*\*(b)</sup> Total mass of aerosol detected by ToF-ACSM ( $m_{\text{Org}} + m_{\text{NO}_3^-} + m_{\text{NH}_4^+} + m_{\text{SO}_4^{2-}} + m_{\text{Cl}^-}$ )

<sup>(c)</sup> Ion balance ratio/ammonium ratio is the ratio between the measured ammonium ( $\text{n}_{\text{NH}_4^+}$ ) and the total ammonium needed to neutralize the major anions ( $\text{n}_{\text{NO}_3^-} + 2 \times \text{n}_{\text{SO}_4^{2-}} + \text{n}_{\text{Cl}^-}$ ). The value is obtained from linear regression.

<sup>(d)</sup> Organic-to-inorganic mass ratio is the ratio between the measured organic aerosol mass ( $m_{\text{Org}}$ ) and the measured inorganic aerosol mass ( $m_{\text{NO}_3^-} + m_{\text{NH}_4^+} + m_{\text{SO}_4^{2-}} + m_{\text{Cl}^-}$ ). The concentration is obtained from ToF-ACSM measurements.

### Ammonium sulfate and nitrate aerosol formation

The ammonium sulfate and nitrate aerosol formation can be explained from the chemistry of a  $\text{HNO}_3\text{-NH}_3\text{-H}_2\text{SO}_4\text{-H}_2\text{O}$  system (Ansari and Pandis, 1998; Seinfeld and Pandis, 2016; Weber et al., 2016; Pye et al., 2020). The formation of ammonium sulfate and nitrate aerosols involves the buffering capacity of semi-volatile  $\text{NH}_3$  partitioning between the gas and particle phase, reacting with  $\text{H}_2\text{SO}_4$  and  $\text{HNO}_3$  and forming aerosols. Coming from  $\text{SO}_x$  emission,  $\text{H}_2\text{SO}_4$  reacts with  $\text{NH}_3$  forming a mixture of ammonium bisulfate ( $\text{NH}_4\text{HSO}_4$ ), ammonium sulfate ( $(\text{NH}_4)_2\text{SO}_4$ ), and leaving some free gas-phase  $\text{NH}_3$  in the equilibrium. As sulfate has an extremely low vapor pressure and ammonium are semi-volatile,  $\text{NH}_4^+/\text{NH}_3$  acts as a mobile species between gas and aerosol phase, establishing equilibrium between the two phases. With the decrease of  $\text{SO}_x$  emissions and steady  $\text{NH}_3$  emissions,  $\text{NH}_4^+$  will be converted back to gas-phase  $\text{NH}_3$  favoring the formation of  $\text{NH}_4\text{HSO}_4$  and the release  $\text{H}^+$ , keeping the aerosol pH stable (0–3) (Weber et al., 2016). The buffering effect of  $\text{NH}_4^+/\text{NH}_3$  is also reflected in the stable ion balance ratio around unity as observed across seasons in this study (see Table S1). The equilibrium mechanism to keep the aerosol pH from rising is expected to occur despite  $\text{SO}_x$  emission reduction, unless the atmospheric sulfate concentration goes below  $0.3 \mu\text{g m}^{-3}$ , where sulfate starts to be associated with non-volatile cations (Weber et al., 2016). With the addition of  $\text{HNO}_3$  in the system coming from  $\text{NO}_x$  emission, ammonium nitrate ( $\text{NH}_4\text{NO}_3$ ) is also formed by either the association of free gas-phase  $\text{NH}_3$  or  $\text{NH}_4^+$  in the aerosol phase moving to the gas-phase. Since  $\text{HNO}_3$  is more volatile than  $\text{H}_2\text{SO}_4$ , ammonium nitrate is moves more freely between the gas and aerosol phase to buffer the aerosol acidity and reach equilibrium. As the buffering system

Formatted: Subscript

Formatted: Font: Not Bold

Formatted: Font: Not Bold

Formatted: Font: Not Bold

Formatted: Font: Not Bold

Formatted: Font: Times New Roman

Formatted: Font: Times New Roman

Formatted: Font: Times New Roman

Formatted: Font: Times New Roman, Italic, Not Superscript  
Subscript

Formatted: Font: Times New Roman

Formatted: Font: Times New Roman

Formatted: Font: Times New Roman

Formatted: Font: Times New Roman

Commented [NF4]: 8.1) Are the values 0.99 and 0.98 statistically different, considering the overall uncertainties with the ACSM?

Formatted: Font: Not Bold

Formatted: Font: Not Bold

Formatted: Font: Not Bold

Formatted: Font: Not Bold

relies on chemical species volatility, meteorological conditions like temperature and relative humidity also play role in the formation of ammonium sulfate and nitrate aerosol.

In summary, from the chemistry perspective, ammonium sulfate is more likely to become condensation nuclei due to low volatility nature of sulfuric acid favouring the aerosol phase, whereas ammonia or amines (as bases) stabilize it. In consequence, they are more likely to occur in smaller particles. Nitric acid plays role in particle growth as it condenses to the particle phase at smaller rate, and serve more as bridge to facilitate the association ammonium sulfate particle clusters in early NPF (Liu et al., 2018). The association of semi-volatile organic vapors to the condensation nuclei occurs through acid-base chemistry and accretion of organic molecules (Zhang et al., 2004; Hodshire et al., 2016), building up the particle mass throughout aerosol formation and growth.

### **S3. PMF analysis**

#### **PMF variables downweighting**

Downweighting is an important step in hybrid PMF input matrix preparation to ensure the variables have similar magnitude over others, or to remove duplicated variables in the matrix. Downweighting is done first to the species mass concentrations and particle number concentrations. The values and errors of species mass concentrations and particle number concentrations in the matrix ( $X_{ij,input}$ ) were downweighted by dividing the dataset with a downweighting constant (DWC) to get the final values and errors ( $X_{ij,DW}$ ).

$$X_{ij,DW} = \frac{X_{ij,input}}{DWC}$$

The goal of downweighting is to normalize the magnitude of newly introduced variables in comparison to the organic mass spectrum, by decreasing their magnitude in reference to the spectrum. The dataset from September 2021 is used for the calculation as it represents the lowest concentration of all chemical species among analyzed periods. The 95% percentile concentration is selected for the calculation to avoid using outlier peak in the dataset. The concentration of m/z 44 fragment ( $C_{44}$ ) is chosen to represent the organic mass spectrum dataset for the calculation of DWC as it generally has the highest average peak among organic fragments. For the inorganic mass concentration, nitrate concentration ( $C_{NO_3}$ ) is selected as the reference for the inorganic chemical species since it generally has the highest concentration among measured inorganics. The PNSD in the 51-65 nm size bin ( $C_{p51-65}$ ) is chosen for the particle size distribution, also for the same reason.

The PNSD has different unit compared to other variables ( $\text{cm}^{-3}$  instead of  $\mu\text{g m}^{-3}$ ). However, we disregard the unit as we are only interested in seeing the particle size concentration variation over time, and how the sizes are being distributed in the

profiles in the PMF solution. In this study, the DWC for PNSD variables was multiplied by 100 to tune down the number distribution values relative to the inorganic species. This empirically tuned multiplier factor is chosen because it gives convergent PMF solutions.

### S3. — **Table F1: Background OA factor**

There are two distinct profiles of F1, affected by seasonality of organic-rich regime and meteorological variables. In the organic-rich regime during summer (June), this factor consists almost solely of organics (94.1%) with trace potassium (5.8%). In spring (May) and autumn (September), there is less organic (81.2% to 83.5%), again traces of potassium (2.6% to 3.3%), and more significant contributions of ammonium (3.3% to 5.1%) and sulfate (10.0% to 11.1%).

In spring (May) and autumn (September), F1 exhibits a diurnal pattern consistent with a more oxidized oxygenated organic aerosol (MO-OOA) factor, with concentration rising slightly across the day (see Fig. S10). The  $f_{44}$  values are 0.28 and 0.32 in spring (May) and autumn (September), respectively. MO-OOA has a relatively stable concentration throughout the day because the factor is typically part of a long-range transported aerosol (Kodros et al., 2020; Chen et al., 2022). The concentration slightly increases from morning to afternoon due to photochemical oxidation. The factor then shows a slight decrease in the late night until sunrise, as its production slows in the absence of radiation. This profile was found in airmasses arriving from the easterly sector that extends from northerly ( $0^\circ$ ) to southerly-southeasterly ( $157.5^\circ$ ) (see Fig. S10), making up 42.1% to 49.3% of total reconstructed PMF mass. To the east, the province of Gelderland is mostly covered by agricultural grass land and forested protected nature areas that emit VOCs, therefore increasing the amount of OA produced. Easterly wind directions may also contain the accumulated pollutants or VOCs from continental Europe, and therefore may contain a variety of OA from either biogenic or anthropogenic sources.

Meanwhile, in summer (June), F1 resembles more the description of less oxidized oxygenated organic aerosol (LO-OOA) factor (see Fig. S10). The  $f_{43}$  and  $f_{44}$  values are 0.09 and 0.17, respectively. LO-OOA has higher nighttime concentration with a slight decrease during the day, suggesting more regional source and higher partitioning of organic vapors into the aerosol phase in the shallow nocturnal boundary layer (Chen et al., 2022). The source region of the organic aerosol is more correlated to wind from the southern sector, extending from northeasterly to southwesterly ( $45^\circ$  to  $225^\circ$ ) (see Fig. S10). By comparing to other factors in the same month and F1 across season, we suggest that due to organic-rich regime, high mean radiation, and high temperatures, highly oxidized organic compounds participate substantially in the size-driven factors forming new particles. This results in less aged OA (lower  $f_{44}$  value) in F1 and F2, and a reduction in the overall PMF fraction of F1 (accounting only 23.7% of total reconstructed PMF mass).

Formatted: Font: Not Bold, Font color: Text 1

Formatted: Indent: Left: 0 cm, First line: 0 cm



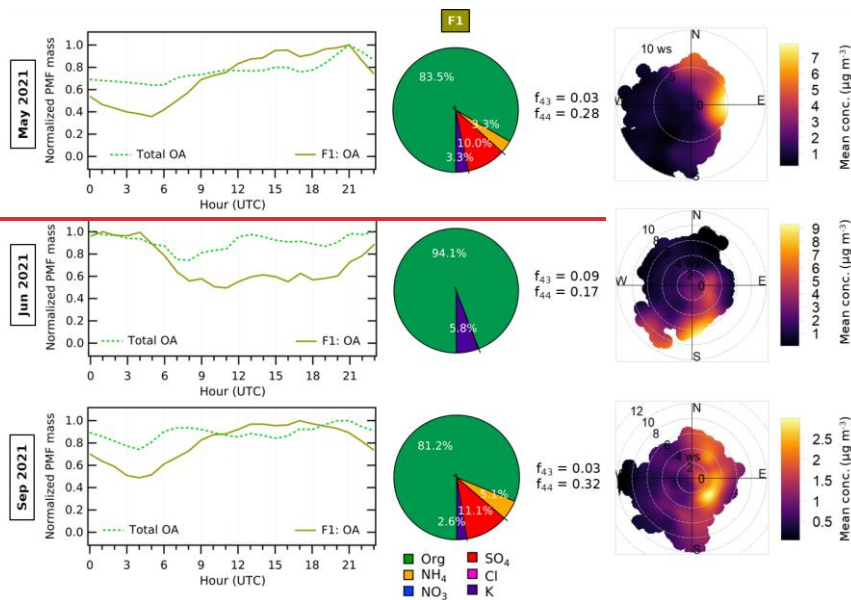


**Figure S10.** Diurnal cycles of F1 and total OA measured by ACSM in May, June, and September 2021 are shown (left), with associated composition (middle) and bivariate polar plots of F1 concentration by wind speed and direction (right) in 10-minute resolution. The concentrations are shown in  $\mu\text{g m}^{-3}$ . The determination of downweighting constant (DWC) for inorganic species mass species and particle number size distribution (PNSD) in the PMF input matrix prior to analysis. The values are obtained from September 2021 dataset and applied for all analyzed periods.

Variable	Value
$C_{f44;95\%} (\mu\text{g m}^{-3})$	1.43
$C_{NO_3;95\%} (\mu\text{g m}^{-3})$	4.95
$C_{p51-65;95\%} (\text{cm}^{-3})$	1198.34
$DWC_{inorganic} = \frac{C_{NO_3;95\%}}{C_{f44;95\%}}$	3.45
$DWC_{PNSD} = 100 \times \frac{C_{p51-65;95\%}}{C_{f44;95\%}}$	83527.07

The information in m/z 44 is duplicated among different organic fragments in the default fragmentation table (Allan et al., 2004) and therefore also need to be downweighted. The downweighting procedure is applied for m/z 44, 28, 18, 17, and 16 signals in the organic mass spectrum as provided by PETv3.08 during PMF input matrix preparation (Ulbrich et al., 2009). A correction calculation for capture vaporizer (CV) is also opted at the end of the PMF analysis to account the additional thermal decomposition in smaller fragments.



### **Determination of PMF solution**

PMF analysis in each period were run unconstrained by varying the number of factors ( $p$ ) from 2 to 8 factors and using varied seed values (min = 0; max = 20; delta = 1). The optimum  $p$  is selected first based on the lowest residuals and local minima ( $Q/Q_{\text{exp}}$ ) of the PMF solutions. With the introduction of inorganic species mass concentration and particle number size distribution (PNSD) variables, we suggest that the PMF solution also must include at least two factors that show a significant signal of particle size distribution, or size-driven factors. A minimum of two size-driven is required in order to study new particle formation and growth. Lastly, the lowest  $Q/Q_{\text{exp}}$  should not be accepted if it contains redundant factors with very similar organic and inorganic profile. The diurnal cycle of each factor and correlation with other chemical species (gas and aerosol species) are also done to confirm the PMF solution. After the optimum  $p$  and seed value are chosen, the rotationality of the solution is explored by performing PMF run with varied rotation ( $f_{\text{peak}}$ ) values (min = -1, max = +1, delta = 0.2).

For each period, a 4-factor solution was picked as the best fit (see Table S3 for the statistical summary). The measured and total reconstructed PMF mass time series, total residuals time series, and scaled residuals of PMF variables are shown in Fig. S11 (May), Fig. S12 (June), and Fig. S13 (September). We can observe that the PMF solutions that were solved by PMF analysis from hybrid PMF input have reduced number of converging solutions unlike regular PMF analysis with only organic spectrum. As we introduce extra variables to the input, more constraints are introduced to the PMF analysis, and thus increasing the number of variables that needs to be considered into the PMF model fit, limiting the number of convergences.  $\text{NO}_3$  and  $\text{SO}_4$  represent the largest contributor of residuals as can be seen in the scaled residual plots in Fig. S11 (May), Fig. S12 (June), and Fig. S13 (September).

**Table S3.** Diagnostic plots of hybrid PMF analyses in May 2021, June 2021, and September 2021, combining CV-ToF-ACSM organic mass spectrum, CV-ToF-ACSM inorganic species concentration, and TROPOS-SMPS PNSD measurements: (a)  $Q/Q_{exp}$  vs. number of factors, (b)  $Q/Q_{exp}$  vs. seed value, (c)  $Q/Q_{exp}$  vs.  $f_{peak}$  value, and (d) correlation of time series and mass spectra among PMF factors (R time series vs. R profiles). The number of factors, seed value,  $f_{peak}$  value,  $Q/Q_{exp}$ , and the reasoning of the chosen PMF solutions are listed below the plots. If not stated, the default values for seed and  $f_{peak}$  are zero.

Plots*/ values chosen	May 2021	Jun 2021	Sep 2021
(a) $Q/Q_{exp}$ vs. $p$			
(b) $Q/Q_{exp}$ vs. seed			
(c) $Q/Q_{exp}$ vs. $f_{peak}$			
(d) Un- centered R time series vs. R profiles			
$p$	4	4	4
seed	1	5	0
$f_{peak}$	0 (no significant change in rotational changes)	0 (no significant change in rotational changes)	0 (no significant change in rotational changes)

<u>Q/Q<sub>exp</sub></u>	<u>12.62</u>	<u>21.27</u>	<u>10.82</u>
<u>Comments</u>	Although solutions with $p > 4$ have lower $Q/Q_{exp}$ , 4-factor solution was chosen because it does not generate redundant factors with same organic and inorganic compositions unlike factors with $p > 4$ . It resolves two size-driven factors, and every factor has distinctive particle size distribution and inorganic composition. One POA (HOA) and three OOA factors (one MO-OOA and two LO-OOA) are also generated.	This PMF solution was chosen because it is solution with the highest number of factors that converged. It resolves two size-driven factors, and every factor has distinctive particle size distribution and inorganic composition. One POA (HOA) and three OOA factors (one MO-OOA and two LO-OOA) are also generated.	This PMF solution was chosen because it is solution with the highest number of factors that converged. It resolves two size-driven factors, and every factor has distinctive particle size distribution and inorganic composition. One POA (HOA) and three OOA factors (one MO-OOA and two LO-OOA) are also generated.

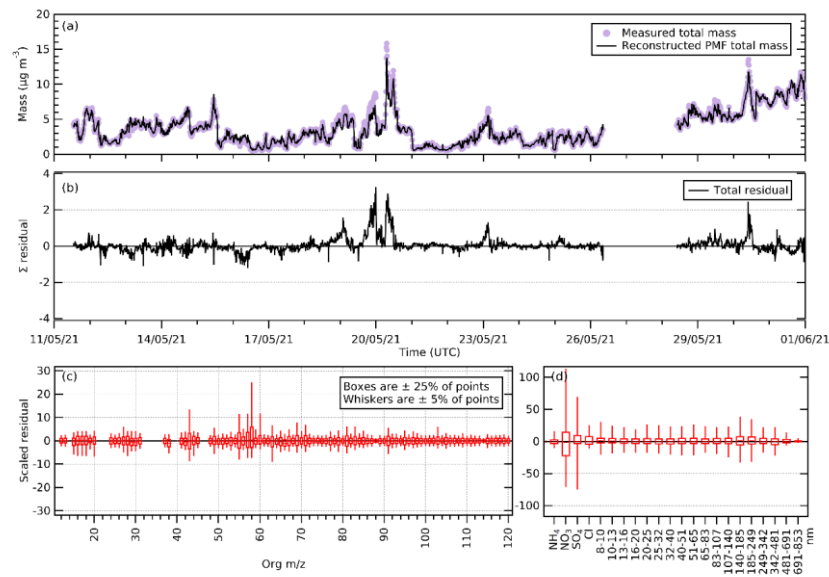


**Figure S11.** Diagnostic plots of hybrid PMF analysis combining CV-ToF-ACSM organic mass spectrum, CV-ToF-ACSM inorganic species mass concentration, and TROPOS-SMPS PNSD measurements in May 2021: (a) time series of the measured and reconstructed PMF mass, (b) time series of residual of the least-square-fit, (c) distribution of scaled residuals for each  $m/z$ , and (d) distribution of scaled residuals for each inorganic species and size-binned particle number concentration.

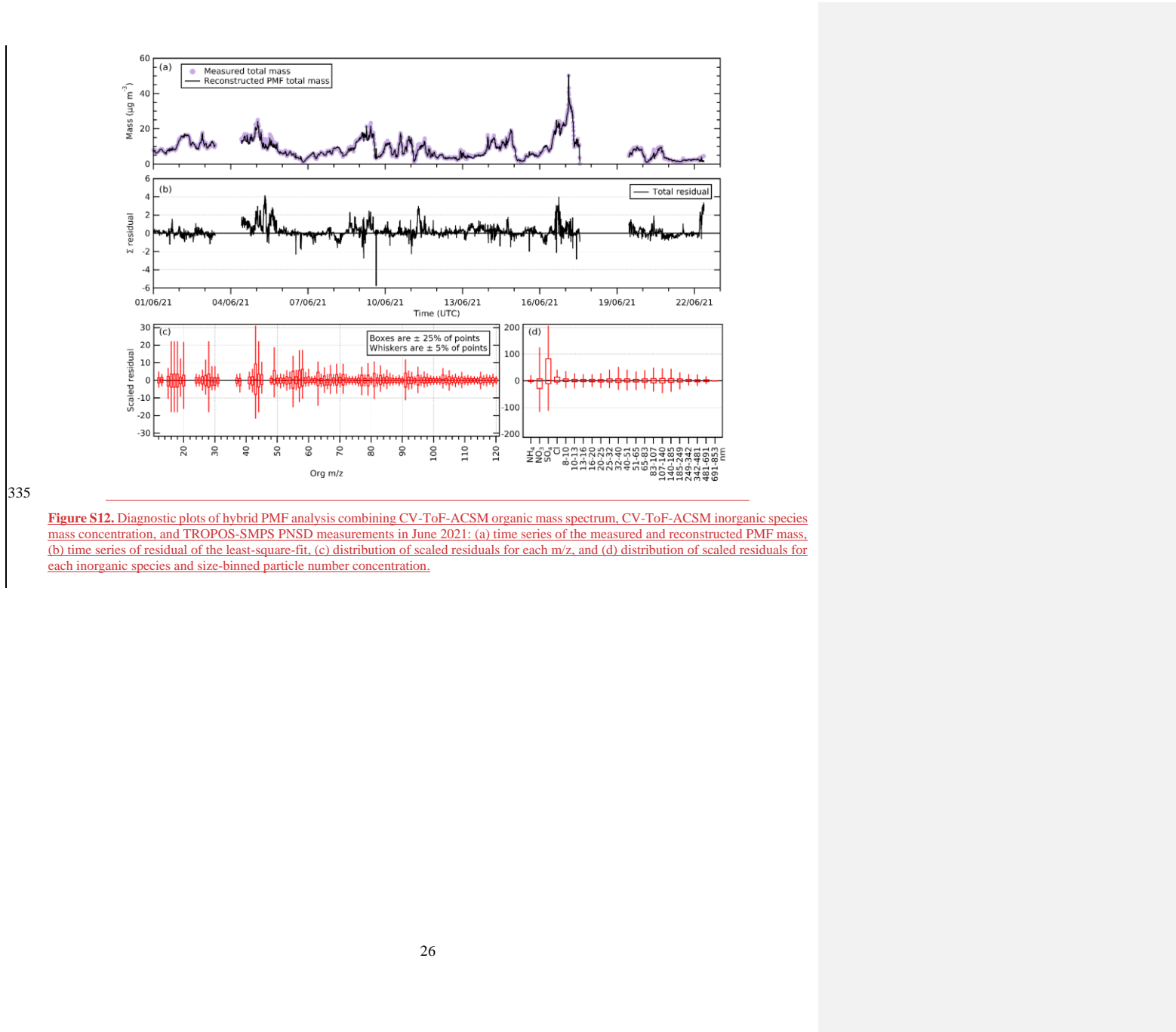


**Figure S12.** Diagnostic plots of hybrid PMF analysis combining CV-ToF-ACSM organic mass spectrum, CV-ToF-ACSM inorganic species mass concentration, and TROPOS-SMPS PNSD measurements in June 2021: (a) time series of the measured and reconstructed PMF mass, (b) time series of residual of the least-square-fit, (c) distribution of scaled residuals for each  $m/z$ , and (d) distribution of scaled residuals for each inorganic species and size-binned particle number concentration.

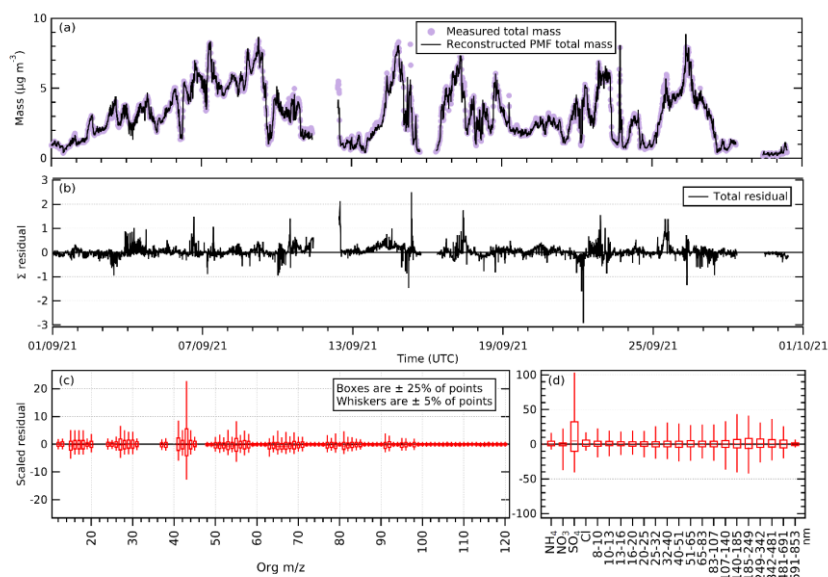


**Figure S13.** Diagnostic plots of hybrid PMF analysis combining CV-ToF-ACSM organic mass spectrum, CV-ToF-ACSM inorganic species mass concentration, and TROPOS-SMPS PNSD measurements in September 2021: (a) time series of the measured and reconstructed PMF mass, (b) time series of residual of the least-square-fit, (c) distribution of scaled residuals for each  $m/z$ , and (d) distribution of scaled residuals for each inorganic species and size-binned particle number concentration.

increase slightly during the day due to photochemical activity and then concentrated in the boundary layer after sunset. It decreases around the midnight until morning due to absence of photochemistry. The OA F1 plumes mostly arrive from the eastern and northern sector in Cabauw.

#### S4. — Correlation of chloride-sulfate and potassium-organic species

Chloride (Cl) and potassium (K) generally only contribute a trace amount of mass in the aerosol (see Fig. 3, Fig. S1, and Fig. S2). Nonetheless, source apportionment of ACSM species and PMF factors showed some interesting patterns with chloride and potassium species. Most of the time, chloride is a visible minority to factors that are abundant in sulfate. In nucleation-mode F6, which is mostly composed of ammonium sulfate, a trace of chloride (0.1% to 6.0%) can be found. Such appearance is also observed for the sulfate-containing size-driven factors (i.e., F4 in May, F3 in June, and F3 in September), where chloride is 0.6% to 3.6% of the total factor mass. The chloride across periods may arrive from sea salt aerosols, although its sources varied as seen in Fig. S8. This is broadly consistent with the dominant source of sulfate being the port region, where sea spray can be a source of the co-occurring chloride.

Formatted: Font: Times New Roman

360

365

A trace amount of potassium was frequently found on factors related to OA. When the OA in F6 is higher during summer (June), a significant amount potassium (2.1%) can be found in the factor. This appearance can also be observed in factors that are dominated by OA or in OA+IA mixed factors (e.g., F5, some F4, F3, and F1) where the potassium concentration ranges from 0.8% to 6.2% of the total mass. Such correlation was also confirmed by the similar pollution rose of the ACSM organic and potassium species (see Fig. S8). This suggests that the potassium originated from the same source as the emissions of organic compounds, perhaps indicative of a woodsmoke contribution from biomass burning (Pio et al., 2008; Urban et al., 2012; Pachon et al., 2013).

**Formatted:** Font: Times New Roman

**Formatted:** Caption